Dissertation

submitted to the Combined Faculty of Natural Sciences and Mathematics

of the Ruperto Carola University Heidelberg, Germany

for the degree of

Doctor of Natural Sciences

Presented by

Luuk Nico van Oosten, M. Sc.

born in: Woerden, The Netherlands

Oral examination: June 3rd 2020

A novel high-throughput and label-free phenotypic drug screening approach:

MALDI-TOF mass spectrometry combined with machine learning strategies

Referees: Prof. Dr. Christian D. Klein

Prof. Dr. Jeroen Krijgsveld

Notice

Parts of the work described in this thesis have been published as follows:

1) An international PCT patent application by Heidelberg University, filed under reference number PCT/EP2018/079221, with the author and first referee of this thesis listed as inventors. This patent application is under review at the time of publishing this thesis (April 2020).

2) A submission to the bioRxive preprint server, which can be cited as follows: Luuk N. van Oosten and Christian D. Klein, 2019, PhenoMS-ML: Phenotypic Screening by Mass Spectrometry and Machine Learning, DOI: https://doi.org/10.1101/593244

3) A conference poster publication, which can be cited as follows: Luuk N. van Oosten and Christian D. Klein, 2019, MALDI-TOF Mass Spectrometry Profiling of Bacteria Coupled with Machine Learning Techniques Identifies Mode of Action of Antibacterial Drugs, Poster Presentation, *Annual Meeting of the German Pharmaceutical Society*, September 1-4, 2019

4) A peer-reviewed publication in the Journal of Medicinal Chemistry, which can be cited as follows: Luuk N. van Oosten and Christian D. Klein, 2020, Machine learning in mass spectrometry: A MALDI-TOF MS approach to phenotypic antibacterial screening, *Journal of Medicinal Chemistry*, DOI: https://doi.org/10.1021/acs.jmedchem.0c00040

Abstract

A renewed and growing interest in phenotypic drug screening approaches in the field of drug discovery is observed, as it has become apparent that target-oriented drug discovery assays have inherent limitations and cannot fulfil the urgent unmet medical need for novel drugs. The shortcomings of target-oriented drug screening assays are especially apparent in the field of antibiotic drug discovery, where target-based approaches largely failed to translate screening hits to clinically relevant drugs.

In this thesis, a proteomics-based phenotypic drug screening approach using MALDI-TOF mass spectrometry was developed, which is able to detect sub-lethal stress in bacterial cells provoked by antibiotics. To achieve this, mass spectra of whole-cells exposed to known antibiotics at concentrations below the minimal inhibitory concentration (MIC) were used to extract relevant mass spectral peaks with a data-dependent and automated computational pipeline created in the MATLAB environment. Using the selected subset of mass spectral peaks, classification models were trained to recognize general mass spectral responses provoked by unknown drugs in the cellular proteome. Additionally, the classification models proved capable of identifying the mechanisms of action of unknown drugs.

To establish and validate the best performing classification modeling procedure, four different feature selection algorithms and nine classification models were analyzed in detail using an *Escherichia coli* data set composed of over 900 spectra, involving 17 antibiotics with four different mechanisms of action, at concentrations ranging 1×MIC down to $^1/_{32}$×MIC in a two-fold dilution series. Four different feature selection approaches were investigated to ensure the extraction of relevant mass spectral data in response to the different antibiotics for classification modeling. The selection approaches included (1) a random forest of decision trees, (2) sequential forward feature selection, and (3) sequential backward feature selection. Mass spectral peaks selected by two or all three of these feature selection approaches were combined into (4) an aggregated feature set. Classification models were trained for all combinations of nine model types and the four feature sets. In this thesis two classification problems were investigated. First, a binary classification problem, to differentiate between affected cells, and non-affected cells based on selected mass spectral peaks. Second, a multi-class model was trained to detect and distinguish between the different antibiotic mechanisms of action, a highly desired drug screening assay characteristic. The combination of these elements yielded 72 models, which were evaluated based on their overall classification accuracy. The overall classification accuracy was determined using internal 10-fold cross-validation and external validation, which was performed with a blind set of 20 drugs. The internal and external validation studies showed that the aggregated feature set in combination with a quadratic support vector machine-based model (Q-SVM) resulted in the best classification performance. For the *E. coli* data set, this was represented by an overall accuracy of 0.92 for internal validation and an

accuracy of 0.95 for the external validation of the Q-SVM model. Classifying based on the mechanism of action of the antibiotics resulted in a classification accuracy of 0.67 for internal validation and 0.80 for external validation. Furthermore, it was shown that the peak selection method was able to identify relevant, known stress associated proteins within the aggregated feature sets of both the binary and the mechanism of action model.

After the experimental workflow and the computational pipeline were established based on *E. coli* data, the method was applied to four different organisms (the Gram-positive bacterium *Staphylococcus aureus*, the fungi *Saccharomyces cerevisiae* and *Candida albicans*, and human HeLa cancer cell line) and different proteomic responses, to explore the versatility and transferability of the developed screening assay. The applicability of the method was demonstrated by the consistent performance of the classification models generated with the experimental and computational pipeline. This resulted in binary model accuracies between 0.92 and 0.97 for internal and 0.77 and 0.95 for external validation, depending on the assayed organism and data set complexity. For mechanism of action models, model accuracies ranged between 0.73 and 0.96 for internal and 0.66 and 0.93 for external validation.

The application of the developed assay on different organisms with different drug stressors highlighted several advantageous characteristics of the developed MALDI-TOF MS screening approach. Both the binary and mechanism of action classification models of *S. aureus* correctly identified an antibiotic drug (fusidic acid) in the blind test set, which had a target binding activity that was not present in the training data set. This implicates the ability of the method to detect novel drugs within known global mechanism of action for which the model was trained. Moreover, external validation of *S. cerevisiae* showed that the binary classification model is able to detect antifungal drugs (tavaborole, an antifungal protein synthesis inhibitor) with a mechanism of action which was not present in the training data set. This is a highly desirable property of any phenotypic screening assay, as it shows that the assay allows for the identification of drugs with novel mechanisms of action. Lastly, the proteomic effect of different types of drugs on mammalian cells was explored by using the HeLa cancer cell line. It was shown that the presented proteomic profiling approach can easily detect several types of drug-induced stresses in HeLa cells, in particular corticosteroids and tubulin (de)polymerization inhibitors, but is less suitable for distinguishing other types of drug classes (neurotransmitter antagonists, statins, opioids). Additionally, the application of the assay on HeLa cells demonstrated the ability to detect different types of stresses, such as the cells' proteomic response to UV exposure or heat shocks. These results pave the way for possible distinction between apoptosis and necrosis pathways in HeLa cells using the presented MALDI-TOF MS based method.

To conclude, a high-throughput compatible, label free, MALDI-TOF mass spectrometry-based screening assay is described in this thesis, which measures sub-lethal drug effects on

the cellular proteome in a phenotypic and pharmacological relevant setting. The method was found suitable for whole-cell screening of small libraries of drugs, and showed the ability to distinguish different types of stresses elicited on multiple types of cell cultures. The potential to find new, weakly active drugs within a known mechanism of action, as well as the ability to detect sub-lethal drug responses with new mechanisms of action for which the model was not trained, was demonstrated. The characteristic to identify novel mechanisms of action in a cell-based screen can be exploited to solve the most pressing issues in drug discovery today. In addition, mechanistic information of the drugs activity can be used as a starting point for further target elucidation or to prioritize drug screening hits. The studies performed in this thesis have resulted in a solid foundation for further research that expand the capabilities of the MALDI-TOF MS-based assay in a broad range of phenotypic profiling applications in the drug discovery field.

Zusammenfassung

Aktuell ist ein erneutes und wachsendes Interesse an phänotypischen Screening-Ansätzen in der Medikamenten-Entdeckung zu beobachten, da deutlich wurde, dass Target-orientierte Wirkstoff-Entdeckungsassays inhärente Limitierungen haben und den dringenden medizinischen Bedarf an neuartigen Medikamenten nicht decken können. Die Einschränkungen von Target-orientierten Ansätzen treten vor allem im Bereich der Antibiotika-Entdeckung auf, in welchem Target-orientierte Screening-Treffer größtenteils nicht in klinisch relevante Wirkstoffe umgesetzt werden können.

In dieser Arbeit wurde ein Proteomik-basierter phänotypischer Wirkstoff-Assay unter Verwendung von MALDI-TOF-Massenspektrometrie entwickelt, mit welchem Antibiotika-induzierter subletaler Stress in Bakterienzellen spezifisch nachgewiesen werden kann. Dafür wurden Massenspektren von ganzen Zellen verwendet, die bekannten Antibiotika in Konzentrationen unterhalb der minimalen Hemmkonzentration (MHK) ausgesetzt waren. Relevante Massenspektralpeaks wurden mit einer datenabhängigen und automatisierten rechnergestützte Pipeline extrahiert, welche in der MATLAB-Umgebung erstellt wurde. Um allgemeine Änderungen in den Massenspektren, die durch unbekannte Arzneimittel im zellulären Proteom hervorgerufen wurden, zu erkennen, wurden unter Verwendung ausgewählter Untergruppen von Massenspektralpeaks Klassifizierungsmodelle trainiert. Zudem erwiesen sich die Klassifizierungsmodelle als geeignet, die Wirkmechanismen der unbekannten Arzneimittel zu identifizieren.

Um das leistungsstärkste Klassifizierungsmodellierungsverfahren zu etablieren und zu validieren, wurden vier verschiedene Merkmalsauswahlalgorithmen und neun Klassifizierungsmodelle unter Verwendung eines *Escherichia coli*-Datensatzes aus über 900 Spektren analysiert. Für die Behandlung der Bakterien wurden 17 Antibiotika mit vier verschiedenen Wirkmechanismen in Konzentrationen zwischen 1×MHK bis $^1/_{32}$×MHK verwendet. Vier verschiedene Merkmalsselektionsverfahren wurden eruiert, um die Extraktion der relevanten Massenspektral-Daten in Anhängigkeit zu den verschiedenen Antibiotika für das Klassifizierungsmodell sicherzustellen. Die Auswahlansätze umfassten (1) eine randomisierte Struktur von Entscheidungsbäumen, (2) eine sequentielle Auswahl von Vorwärtsmerkmalen und (3) eine sequentielle Auswahl von Rückwärtsmerkmalen. Massenspektralpeaks, die durch zwei oder alle drei dieser Merkmalsauswahlansätze ausgewählt wurden, wurden zu einem aggregierten Merkmalssatz kombiniert (4). Für alle Kombinationen von neun Modelltypen und den vier Merkmalssätzen wurden Klassifizierungsmodelle trainiert. Zwei Klassifizierungsprobleme wurden in dieser Arbeit untersucht. Erstens wird ein binäres Klassifizierungsproblem beschrieben, um basierend auf ausgewählten Massenspektralpeaks zwischen behandelten Zellen und nicht behandelten Zellen zu unterscheiden. Zweitens wurde ein Mehrklassenmodell trainiert, um die verschiedenen antibiotischen Wirkmechanismen zu erkennen und zu unterscheiden. Hierbei

handelt es sich um eine besonders wichtige Eigenschaft von Wirkstoff-Assays. Die Kombination dieser Elemente ergab 72 Modelle, die anhand ihrer Gesamtklassifizierungsgenauigkeit bewertet wurden. Die Gesamtklassifizierungsgenauigkeit wurde unter Verwendung einer internen 10-fachen Kreuzvalidierung und einer externen Validierung, für die ein Blindsatz von 20 Arzneimitteln vermessen wurde, bestimmt. Die internen und externen Validierungsstudien zeigten, dass der aggregierte Merkmalssatz in Kombination mit einem maschinenbasierten quadratischen Support-Vektor-Modell (Q-SVM) die beste Klassifizierungsleistung erbrachte. Für den *E. coli*-Datensatz wurde dies durch eine Gesamtgenauigkeit von 0,92 für die interne Validierung und eine Genauigkeit von 0,95 für die externe Validierung des Q-SVM-Modells verdeutlicht. Die Klassifizierung durch den Wirkmechanismus der Antibiotika ergab eine Klassifizierungsgenauigkeit von 0,67 für die interne Validierung und 0,80 für die externe Validierung. Weiterhin konnte gezeigt werden, dass die Peakauswahlmethode relevante, bekannte stressassoziierte Proteinpeaks in den aggregierten Merkmalssätzen sowohl des binären Modells als auch des Wirkmechanismusmodells identifizieren konnte.

Im Anschluss an die Erstellung des experimentellen Arbeitsablaufs und der Rechenpipeline basierend auf *E. coli*-Daten, wurde die Methode auf vier verschiedene Organismen (*Staphylococcus aureus*, *Saccharomyces cerevisiae*, *Candida albicans* und humane HeLa-Krebszelllinie) und verschiedene proteomische Reaktionen angewendet, um die Vielseitigkeit und Übertragbarkeit des entwickelten Assays zu untersuchen. Die Anwendbarkeit der Methode wurde durch die konsistente Leistung der mit den experimentellen und Rechenpipeline-generierten Klassifizierungsmodellen demonstriert. Dies führte im binären Modell zu Genauigkeiten zwischen 0,92 und 0,97 für die interne und 0,77 und 0,95 für die externe Validierung, abhängig vom untersuchten Organismus und der Komplexität des Datensatzes. Für das Wirkmechanismus-Modell lagen die Modellgenauigkeiten zwischen 0,73 und 0,96 für die interne und zwischen 0,66 und 0,93 für die externe Validierung.

Die Anwendung des entwickelten Assays im Bezug auf verschiedene Organismen mit verschiedenen Arzneimittelstressoren hob mehrere vorteilhafte Eigenschaften des entwickelten MALDI-TOF-MS-Assays hervor. Sowohl das binäre als auch das Wirkmechanismus-Klassifizierungsmodell von *S. aureus* identifizierten ein Antibiotikum (Fusidinsäure) im Blindtest-Set korrekt, dessen Targetwirkung nicht im Trainingsdatensatz vorhanden war. Dies impliziert, dass es mithilfe dieser Methode möglich ist, neuartige Medikamente innerhalb eines bekannten globalen Wirkmechanismus nachzuweisen, für den die Modelle trainiert wurden. Darüber hinaus zeigte die externe Validierung von *S. cerevisiae*, dass das binäre Klassifizierungsmodell Antimykotika mit einem Wirkmechanismus nachweisen kann, der im Trainingsdatensatz nicht vorhanden war (Tavaborol, ein antimykotischer Inhibitor der Proteinbiosynthese). Diese Eigenschaft ist für phänotypische Assays sehr wichtig, da sie zeigt, dass der Assay die Identifizierung von

Wirkstoffen mit neuartigen Wirkmechanismen ermöglicht. Zuletzt wurde unter Verwendung von HeLa-Krebszellen die Wirkung verschiedener Arzneimittel auf das Proteom von Säugetierzellen untersucht. Es konnte gezeigt werden, dass der proteomische Ansatz verschiedene Arten von arzneimittelinduzierten Belastungen in HeLa-Zellen nachweisen kann. Insbesondere eignet sich der Assay zur Unterscheidung von Corticosteroiden und Tubulin-(De)polymerisationshemmstoffen, jedoch weniger zur Unterscheidung anderer Wirkstoffklassen (Neurotransmitter-Antagonisten, Statine, Opioide). Weiterhin zeigte der Assay mit HeLa-Zellen die Fähigkeit, verschiedene Arten von Belastungen für die Zellen zu erkennen wie z. B. die proteomische Reaktion der Zellen auf UV-Exposition oder Hitzeschocks. Diese Ergebnisse ebnen den Weg für eine mögliche Unterscheidung von Apoptose- und Nekrose-Reaktionen der HeLa-Zellen mittels der vorgestellten MALDI-TOF-MS-Methode.

Zusammenfassend wird in dieser Arbeit ein Hochdurchsatz-kompatibler, markierungsfreier MALDI-TOF-Massenspektrometrie-basierter Assay beschrieben, der subletale Wirkungen von Verbindungen auf das zelluläre Proteom in einem phänotypischen und pharmakologisch relevanten Umfeld misst. Das Verfahren erwies sich als geeignet für die Ganzzell-Testung kleiner Arzneimittelbibliotheken und zeigte die Fähigkeit, verschiedene Arten von Zellstress zu unterscheiden, die bei mehreren Zellkulturarten hervorgerufen wurde. Desweiteren wurde das Potenzial, neue und schwach aktive Wirkstoffe mit einem bekannten Wirkmechanismus zu finden, demonstriert. Zudem wurde gezeigt, dass der Assay in der Lage ist, subletale Wirkstoffreaktionen mit neuen Wirkmechanismen zu erkennen, für die das Modell nicht trainiert wurde. Die Eigenschaft, neuartige Wirkmechanismen in einem zellbasierten Screening zu identifizieren, kann genutzt werden, um die dringlichsten Probleme der aktuellen Wirkstoffforschung zu lösen. Darüber hinaus können mechanistische Informationen über die Wirkstoffwirkung als Ausgangspunkt für die weitere Targetaufklärung oder zur Priorisierung von Arzneimittelscreening-Hits verwendet werden. Die Ergebnisse, die in dieser Arbeit präsentiert werden, bilden ein solides Fundament für weitere Forschung, um die Anwendbarkeit des MALDI-MS basierten Assays auf ein breites Spektrum phänotypischer Anwendungen im Bereich der Wirkstoffentdeckung zu erweitern.

Tabel of Contents

1 Introduction

The current rise in antimicrobial resistance among bacteria and fungi endangers effective healthcare practice, and has severe, worldwide economic consequences [1]. The increase in antibiotics resistance is a complex problem, resulting from misuse of antibiotic drugs, [2] in combination with the absence of significant investment and progress in drug development pipelines [1, 3]. As resistance has evolved against almost every antibiotic placed on the market, irrespective of antibiotic class or target [4], there is a growing need for new antibiotics and novel classes of antibiotics to treat resistant bacteria. The increase of (multi-) drug resistant organisms is associated with an increase in medical costs and mortality rates [5]. In Europe and the US alone, resistant bacterial infections are estimated to cause 50.000 deaths annually [6]. According to conservative estimates, antimicrobial resistant infections (including fungal and viral infections) cause over 700.000 deaths annually worldwide. At the current rate, it is projected that this number will rise to over 10 million deaths annually by 2050, as indicated in Figure 1. By then, the number of antimicrobial resistant deaths will surpass the combined current incidences of cancer and diabetes related deaths [5]. The rise in antimicrobial resistance is also pressing on modern health care systems. Without the availability of effective antibiotics, common surgical procedures, but also childbirth, could once again become life-threatening. Similarly, most clinical invasive fungal infections are caused by complications of surgery, or occur in people undergoing chemotherapy or otherwise immunocompromised people, such as those with HIV infection [7]. Moreover, the increase in antimicrobial resistance will account for 2.0-3.5% decrease in global gross domestic product by 2050 [5], equally damaging as the global financial crisis of 2008-2009 [8].
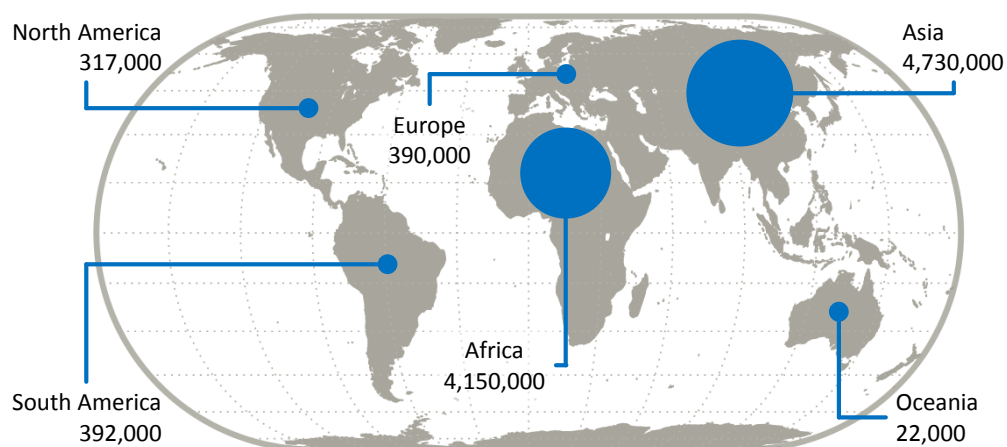

Figure 1. Projected annual deaths attributed to antimicrobial resistance by the year 2050. Depicted are overall mortality numbers per continent, excluding Antarctica. Image adapted from [5].

To offer solutions for the pressing needs in the field of antibiotic and antifungal drug discovery, this thesis focusses on a new mass spectrometry-based screening technique that supports the identification of novel, weakly active drug compounds, while simultaneously providing information of the mechanism of action involved. For the establishment of such a screening technique, the mechanisms of action of existing antibiotics and antifungal drugs must be understood. In the first two sections of this introduction, the currently used antimicrobial pathways involved in bacterial and fungal infections will be presented, as drug resistant bacterial and fungal infections are among the most urgent issues threatening health care systems [5]. As the current drug discovery pipelines are failing to provide new antibiotics, it is paramount to lay out the information content and the limitations of existing screening techniques, in order to (partially) solve drug screening issues with a new approach. Therefore, a brief overview of past and current antibiotic drug screening approaches will be discussed. Subsequently, the analytical technique employed in this work, matrix assisted laser desorption ionization – time of flight (MALDI-TOF) mass spectrometry, will be described in more detail. The final section of the introduction will cover machine learning approaches, as the data complexity in combination with the throughput of the developed assay requires advanced computational analysis to establish a comprehensive and robust assay to detect weakly active drug hits and their respective mechanism of action.

1.1 Antibacterial drugs

The most important classes of antibiotics to treat bacterial infections include the β-lactams, aminoglycosides, tetracyclines, macrolides, fluoroquinolones, folate pathway synthesis inhibitors, and rifamycins [3]. Figure 2 depicts a schematic overview of the most important antibiotic targets engaged by these mentioned antibiotic drug classes.

A well-known group of antibiotics, the β-lactams, disrupt the cell wall synthesis, shown in red in Figure 2. Among the β-lactams is probably the most famous antibiotic of all, penicillin, originally derived in 1928 from a *Penicillium* mold by Alexander Flemming [10]. The β-lactam drugs inhibit the assembly of bacterial peptidoglycan layer by binding to penicillin-binding proteins (PBPs) [11]. By inhibiting PBPs, peptidoglycan cross linkages required for proper cell wall synthesis cannot be created, which causes cell death. Another long-existing group of drugs are the sulfonamide drugs, originally developed in the early 1930s [12]. Sulfonamide drugs, together with the later developed trimethoprim-like drugs [13], are antimetabolite drugs, inhibiting crucial steps in the bacterial folate synthesis pathway (shown in yellow in Figure 2), thereby depleting the cell of essential building blocks for proper nucleic acid synthesis [14].
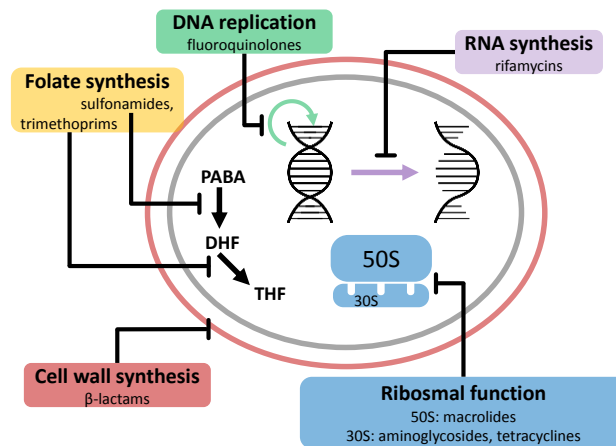
Figure 2. Simplified schematic of main antibiotic drug targets in bacterial cells and their corresponding classes of drugs. In green, the inhibition of DNA gyrase and topoisomerase II, disrupting DNA stability. Depicted in magenta is the inhibition of DNA-dependent RNA polymerase, inhibiting the production of RNA. In blue the ribosomal inhibitors, of which the most prominent classes of antibiotics bind to either the 50S or the 30S ribosomal subunit, thereby disrupting protein synthesis. In red are depicted cell wall synthesis inhibitors, inhibiting the cross-linking of the peptidoglycan layer. In yellow, antimetabolite drugs inhibiting crucial steps in the folate synthesis pathway. The sulfonamide drugs inhibit the dihydropteroate synthase enzyme, which converts para-aminobenzoic acid (PABA) to dihydropteroate, which in its turn is further converted to dihydrofolic acid. (DHFA) The trimethoprim-like drugs inhibit dihydrofolate reductase, an enzyme that reduces dihydrofolic acid (DHFA) to tetrahydrofolic acid (THFA). Image inspired by [9].

Another more direct way of disrupting the bacterial genomic material is by direct interference with DNA replication, as performed by the fluoroquinolone class of drugs (shown in green in Figure 2). Fluoroquinolones prevent mainly DNA replication and transcription by inhibiting gyrase and topoisomerase IV [15]. By specifically inhibiting the ligase activity of those enzymes, supercoiling is disrupted and single and double strand breaks in the DNA are introduced, leading to cell death [16]. Another way of disrupting nucleic acids is by targeting the RNA production directly, shown in purple in Figure 2. Rifamycins inhibit bacterial nucleic acid synthesis by inhibiting the bacterial DNA-dependent RNA polymerase [17]. As the production of mRNA is thereby inhibited, protein synthesis comes to a halt, resulting finally in cell death.

The last major groups of antibiotics, the macrolides, tetracyclines, and aminoglycosides, target protein synthesis by interfering with the ribosomal function [18], shown in blue in Figure 2. The macrolide antibiotics inhibit protein synthesis by binding near the P-site and the exit tunnel on the large 50S ribosomal subunit, which either prevents peptidyl transferase from adding an amino acid or prevents peptide elongation, thereby inhibiting translation [19, 20]. Contrarily to the macrolide antibiotics, antibiotics of the class aminoglycosides and tetracyclines mainly interfere with the small 30S ribosomal subunit. Aminoglycosides disrupt peptide elongation, causing inaccurate translation which leads to

7

truncated or altered protein sequences [21]. Tetracyclines, first discovered in the 1940s [22], inhibit protein synthesis by blocking the A-site on the 30S ribosomal subunit, thereby preventing the attachment of aminoacyl-tRNA and further growth of the peptide chain [23].

Most of the antibacterial drugs inhibiting the major macromolecular synthesis pathways shown in Figure 2 are known since the so-called Golden Age of antibacterial drug discovery (1940-1970) [24, 25]. Even though several new antibiotics have entered the market since then, these new drugs, such as additional generations of cephalosporins (a β-lactam) and fluoroquinolones, were all members of known, existing classes antibiotics [3, 26]. As most of these new drugs were more of the same, the underlying resistance mechanisms were not addressed. Therefore these new drugs did not significantly contribute to the fight against the rise in antibiotic resistance.

Bacteria gain resistance to antibiotics mainly by three different mechanisms [27-29]. The most prominent mechanisms by which bacteria gain resistance are by horizontal and lateral gene transfer (plasmid exchange) and by mutations in resistance-associated genes. The gene transfer and mutations can cause alterations in the abundance and structure of porins and efflux pumps. These alterations make it impossible for the drug to reach its intracellular target protein by reducing the cell permeability, or by increasing drug-efflux, respectively [30]. Other contributors to antimicrobial resistance are changes in antibiotic targets themselves, caused by mutations in target proteins or by introducing post-translational modifications (PTMs), rendering the drug ineffective. The third major contributor to resistance development is enzyme-catalyzed modifications, which inactivate the antibiotics. The most well-known example is the increased presence of β-lactamase enzymes that hydrolyze the β-lactam ring of penicillin- and cephalosporin-like structures. These processes usually happen relatively fast, as resistance to novel antibiotics is usually observed within months to years after entering the market. This is problematic, as drug development typically takes much longer [6, 31].

Although there are supposedly over 160 essential proteins shared among a wide array of bacteria which could serve as potential antibiotic targets, only 40 targets are represented by currently marketed drugs [32]. The genomics era was thought to boost the number of molecular targets in bacteria, however the target-directed approach failed to deliver new drugs [33, 34]. Only two new classes of antibacterial compounds have been introduced since the dawn of the genomic era, namely linezolid and daptomycin [3]. Meanwhile, the main targets remain cell wall synthesis proteins, DNA gyrases, and the bacterial ribosome [35]. Recently, antibiotic drug development mainly focused on combinational therapy, as it is seldom enough to just inhibit one specific target [36]. For example, to overcome β-lactam resistant bacteria, combinational therapy of a β-lactamases inhibitor and a β-lactam is typically given. Most commonly, a mixture of clavulanic acid (itself a β-lactam, a β-lactamase inhibitor) amoxicillin and is given as therapy [37]. The clavulanic acid inhibits the bacterial β-

lactamase enzymes, which allows the accompanying amoxicillin to bind to its target PBPs. Similarly, trimethoprim and sulfamethoxazole are almost exclusively given as combination therapy to avoid resistance development [36].

As antibiotic resistance is on the rise, novel antibiotics with new mechanisms of action are urgently needed, but currently only few of such truly novel compounds are under investigation [38, 39]. One recent example is the drug halicin, which was previously under investigation for treatment of diabetes type 2. Halicin was identified as potential novel antibiotic using artificial intelligence in a drug repurposing project [40]. It was shown that halicin has a unique antibacterial mechanism of action which sequestered iron inside bacterial cells, thereby disrupting pH regulation across the cell membrane, causing the proton motive force to dissipate and consequently cell death.

Although drugs with new mechanisms of action are desperately needed, the search for novel mono-therapeutic drug targets and novel mechanisms of action has had very low output. Therefore, it is postulated by some that antibiotics research should not only focus on new finding novel chemical scaffolds with new molecular targets, but should be complemented by innovative screening of the main classical targets involved in macromolecular synthesis pathways [34, 41], as depicted in Figure 2.

1.2 Antifungal drugs

Most clinical invasive fungal infections are caused by complications of surgery, chemotherapy, organ transplantation, or as a side-effect of immunomodulatory therapies [7]. For these systemic fungal infections, the most important antifungal drug classes available are relatively limited to the polyene drugs (among which amphotericin-B), azole drugs (among which fluconazole, voriconazole), and the echinocandin drugs (among which caspofungin) [42-44]. A schematic overview of the main fungal drug targets is provided in Figure 3.

Shown in yellow in Figure 3 are the antifungal drugs which interfere with crucial steps in ergosterol synthesis (the azoles and allylamines) [46] or bind directly to ergosterol in the cellular membrane (polyenes) [47]. Ergosterol is a sterol found almost uniquely in fungal cell membranes, fulfilling the same function as cholesterol in higher eukaryotic animal cells [46]. As sterol is an essential component of the fungal cell membrane, it is an excellent target for antifungal drugs. By binding directly to ergosterol, the polyene antifungals weaken the membrane, causing leakage of ions and eventually cause cell death. One of the most commonly used antifungal drugs of this class is amphotericin-B [48].
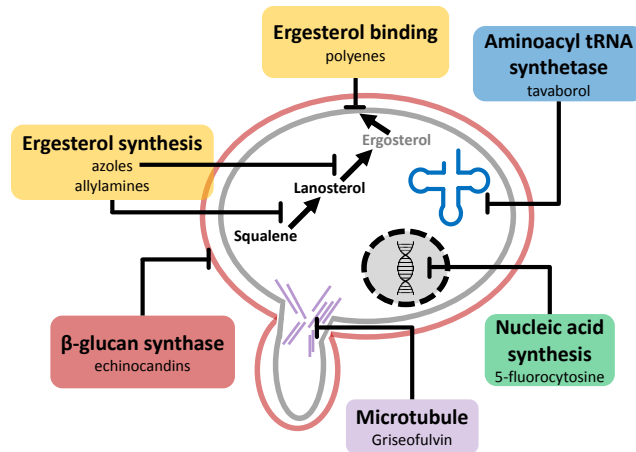
Figure 3. Simplified schematic of main antifungal drug targets and corresponding classes of drugs. In yellow are drugs interfering with crucial enzymes in ergosterol synthesis (the azoles and allylamines) and the polyenes (binding directly to the ergosterol in the fungal membrane). In blue tavaborole, which inhibits aminoacyl tRNA synthetase, thereby effectively inhibiting protein synthesis. In green, 5-flucytosine, a pyrimidine analog, inhibiting proper nucleic acid synthesis. In magenta, griseofulvin, a mitotic inhibitor. In red, the echinocandins inhibiting β-glucan synthase enzyme, an enzyme for fungal cell wall synthesis. Image inspired by [45].

The other two major classes shown in yellow in Figure 3, the azole and allylamine drugs inhibit crucial steps in the biosynthesis pathway of ergosterol, thereby depleting the cell of a sufficient amount of ergosterol causing membrane disruption, and, consequently, cell death [49]. The class of azole drugs specifically inhibits lanosterol 14-alpha-demethylase, a protein essential in sterol biosynthesis which converts lanosterol to ergosterol [50, 51]. The allylamines inhibit another essential enzyme in the sterol synthesis pathway, squalene monooxygenase, which oxidizes squalene to squalene epoxide [52].

Depicted schematically in red in Figure 3 are the fungal cell wall synthesis inhibitors, the echinocandin class of drugs. Although the first echinocandins were discovered in the early 1970s [53], the first echinocandin to be put on the market was caspofungin in the early 2000s [54]. The echinocandin drugs inhibit the 1,3-β-glucan synthase, an essential enzyme in fungal cell wall synthesis. By disrupting the assembly of the fungal cell wall, echinocandins cause osmotic stress and lysis, leading to cell death [54].

Among the antifungal drugs that work specifically intracellularly are the aminoacyl tRNA synthetase inhibitors (depicted in blue in Figure 3), the pyrimidine analogue drugs (depicted in green in Figure 3), and the mitotic inhibitors (depicted in magenta Figure 3). The tRNA synthetase inhibiting drug tavaborole is one of the most recently approved drugs, being FDA approved for topical applications in 2014 [55]. By inhibiting the fungal aminoacyl tRNA synthetase, the fungal protein synthesis is disrupted [56]. Among the antifungals interfering with nucleic acid synthesis is 5-fluorocytosine, a pyrimidine analogue drug [57], shown in green in Figure 3. Once inside the cell, it is converted to several different intermediates,

which in turn inhibit DNA and RNA biosynthesis. The disturbance of RNA synthesis consequently disrupts protein synthesis. Lastly, depicted in magenta in Figure 3, are the drugs inhibiting microtubule assembly, of which the most well-known antifungal member is griseofulvin [58]. By interfering with microtubule assembly, the process of mitosis is inhibited.

Compared to bacteria, systemic antifungal drugs are relatively difficult to develop due to the eukaryotic nature of both the fungal and human cells. Their relatively close genetic composition limits the number of fungal-specific drug target proteins [7]. This causes many antifungal drugs, and antifungal screening candidates, to have severely toxic side-effects. Similar to drugs against bacterial infections, most of these classes of antifungal drugs were discovered over 50 years ago, and since then, only the polyenes, azoles and echinocandin drugs remain the viable and effective options for most life-threatening systemic fungal infections [7]. However, resistant fungal strains are becoming more frequent, especially among common *Candida* species [59, 60].

Fungi gain resistance through similar mechanisms as bacteria, either by target modification, target upregulation, the use of efflux pumps (or upregulation of efflux pump expression), or the drugs are inactivated in a similar way that β-lactamases hydrolyze β-lactam antibiotics in bacteria [51, 61]. Additionally, yeasts are able to form biofilms, which in some cases are extremely resistant to drug treatment due to the high cell density and protective properties of the extracellular matrix [62].

The limited classes of antifungal drugs available for systemic infections, and the rise in resistant antifungal strains has resulted in the current unmet medical need for novel, safe, antifungal drugs [7, 63]. Like antibacterial drug discovery, current antifungal drug research is focusing on the identification of new pathways that could be targeted, as well as combinational therapy approaches [64]. Additionally, novel drugs are under investigation, such as drugs targeting membrane-associated fungal-specific lipids, drugs targeting the fungal mitochondria, and drugs targeting fungal virulence factors, but also repurposing of clinically approved drugs as antifungals is under investigation [65].

1.3   Antimicrobial drug screening

In the 'Golden Age' of antibacterial drug discovery (1940-1970), numerous substances and crude extracts were screened in whole cell-assays [3], such as the Waksman screening platform [66], which have yielded most of the antibacterial drug classes still used today. The advent of rapid sequencing of genomic data, progress in recombinant expression, and biochemical characterization of proteins shifted the field of antibiotic drug discovery from phenotypic cell-based assays towards high-throughput target-based screening [33, 67, 68]. The major problem with target-based discoveries in the context of antibiotic drug discovery,

11

is that *in vitro*, activities of single targets are usually poorly correlated to cellular efficacy [3, 33, 69]. This is mainly due to the fact that compounds discovered in a target-based screening simply could not cross the bacterial cell membrane to reach their target [41]. Other disadvantages of target-based screens are that they inherently do not yield information about off-target effects and do not yield insight or information on novel drug targets or pathways.

The poor yield of target-based approaches is not only problematic in the field of antibiotic drug discovery, but is a more widely realized shortcoming of target-based drug screening approaches, such as in the field of antiviral and cancer drug discovery [70-72]. Out of all the 259 drugs (not solely antimicrobials) approved between 1999 and 2008, 75 were drugs with novel molecular mechanisms of action (first-in-class), of which 50 were small molecules and 25 biologics. Of these 75 first-in-class drugs, 28 small molecule drugs were found using a phenotypic screen, compared to only 17 being found by target-based approaches [71] (the remaining 30 drugs concerned were biologics or modified natural substrates, outside the scope of this thesis). From the new molecular entities, nine of them had unknown mechanism of action [72]. Notably, a detailed knowledge of the mechanism of action of new drugs is not required for FDA approval.

However, target-based studies are very suitable in identifying and improving follower drugs (also known as 'me-too' drugs) containing the same chemical scaffolds as previously approved drugs, with just minor modifications [73]. In total, 83 of such drugs were found between 1999 and 2008 using target-based screenings. In the same timeframe 30 follower drugs were identified using a phenotypic screen, which is still a considerable amount, underlining the power of phenotypic screening [71, 72].

Nowadays, whole-cell based phenotypic assays are thought to be favored over target-based assays for finding lead compounds [74], mainly because it is considered easier to identify the cellular target, then to engineer permeability of a compound [33]. In addition, the use of cell-based assays in drug discovery can be favorable, as it reflects the complexity and interplay of multiple target proteins and associated pathways in an in vivo setting [71].

Based on renewed appreciation and the corresponding benefits of cell-based phenotypic screening assays, this thesis describes a newly devised phenotypic profiling approach for drug screening using a proteomics approach. Multiple different phenotypic profiling approaches already exist, yet have some drawbacks and limitations. Therefore, the next section will present available techniques to highlight which characteristics are desired to implement in a novel phenotypic screening approach.

1.4 Phenotypic screening assays

Phenotypic antimicrobial susceptibility testing, in one of its most simplistic forms, measures growth inhibition of a microorganism. This is either done in agar plates using disk-diffusion tests [75, 76] or in a more high-throughput turbidity assay [77]. The disadvantage of these methods is that the readout provides very limited information: growth or no growth. When screening at a fixed concentration, potential hits can be missed, as the growth-inhibitory effect is not visible at the (usually fixed) screening concentration. For example, the minimal inhibitory concentration (MIC) of the antibiotics vancomycin (256 mg/L) and ciprofloxacin (0.03 mg/L) for *E. coli* vary by approximately a factor 8000 [78]. The identification of weakly active drugs is an important desired screening characteristic, as these weakly active hits can be further optimized in fragment-based drug discovery pipelines [79]. In fragment-based drug discovery, small (typically <300 Da) weakly active compounds are sought, which are subsequently grown into larger compounds, or are combined to produce leads with a higher activity [80].

In the field of drug screening, it has been remarked that it is sensible to employ screening methods that yield more information on the phenotype than just binary growth/no-growth readout, such as mechanistic information [81]. Feng and co-workers propose to use assays which yield multiplexed read-out parameters such as protein arrays, mRNA profiling, and cytological profiling to monitor phenotypic responses (for an extensive review see [81]), but have also remarked that each of these popular techniques has some disadvantages and limitations. For example, protein microarrays have the disadvantage of limited coverage depending on availability of specific antibodies and mRNA profiling has high associated cost and a relatively low throughput.

Currently, cytological profiling is one of the most applied methods to investigate the state of the cell, as it can be coupled to image recognition software to extract features from imaging data. Cytological profiling, as described by the Pogliano group, is used to identify bacterial cellular pathways in response to antibiotics by means of fluorescence microscopy in combination with linear discriminant analysis clustering [82, 83]. Although this method allows for distinguishing between cells treated with different types of antibiotics, as a drug screening assay it is less suitable because of the relatively high concentrations of antibiotics required (5 times the MIC) to see a noticeable effect. Moreover, due to the nature of fluorescence microscopy, this method is less prone towards miniaturization and high-throughput screening, as it requires multiple stains and antibodies. These limitations prevent large library screenings and the detection of weakly active drug compounds with optimization potential.

An example of a large library phenotypic drug screening approach to evaluate eukaryotic cells is described by Young and co-workers [84]. In this study, HeLa cells were stained with multiple dyes and antibodies after treatment with a drug library of over 6000 compounds.

After drug treatment, cytological features were measured to determine the phenotypic profile of the HeLa cells using factor analysis. Overall, they were able to predict the correct drug target in 70% of the cases in a validation study, but remarked that the ability to detect new drug types was limited.

Besides fluorescence microscopy used for cytological profiling, other spectral profiling-based methods have been investigated. Athamneh and co-workers have the described the use of Raman spectroscopy to profile the phenotypic response signatures in *E. coli* upon treatment with different classes of antibiotics [85]. By employing Raman spectroscopy, they were able to distinguish the bacteria's response towards multiple antibiotic classes and individual antibiotic species. They were able to train classification models based on the Raman spectra that could predict the mechanism of action of antibiotics involved in the treatment of *E. coli*. Their classification model's highest accuracy was reached by using a combination of principle component analysis (PCA) and discriminant analysis, which correctly classified the antibiotic mechanism of action in 84% of the cases and in 71% of the cases the correct antibiotic drug. The major drawback of their method is the use of relatively high concentrations of antibiotics (3 times the MIC) to observe an effect. The low sensitivity makes Raman spectroscopy-based assay unable to screen for weakly active antibiotics. Similar to Athamneh and co-workers, surface enhanced Raman spectra (SERS) has been used to determine the phenotype of bacteria [86] by Liu and co-workers. They found that spectra of bacteria changed upon exposure to cell wall synthesis inhibitors. The main disadvantage of their method is, again, the use of a high concentration of antibiotics (5 times the MIC), which makes the identification of weakly active drugs impossible.

Although there is a wide variety of phenotypic screening assay available, which are based on different analytical techniques, none of them are able to combine all desired characteristics required for screening weakly active antibiotics. The desired characteristics are the capability to screen large libraries without expensive (radio)labels or complicated sample workup limiting throughput (such as liquid chromatography), as well as the ability to detect sub-lethal compounds and provide information on mechanism of action. Therefore, a whole-cell based phenotypic screening assay in this thesis was designed to differentiate between effects of existing (and potentially new) mechanisms of action and to identify weakly active compounds in a (relatively) high-throughput and label-free manner. This assay is based on a proteomics approach using MALD-TOF mass spectrometry. In the following two sections, a brief theoretical background of MALDI-TOF mass spectrometry and an overview of its general applications are provided.

1.5 MALDI-TOF principles

Mass spectrometry is an analytical technique to determine the mass-to-charge ratio of ions [87]. This results in a mass spectrum, a graph that depicts the ion intensity as a function of the mass-to-charge ratio (m/z). A mass spectrometer generally consists of three components: an ion source, a mass analyzer, and a detector. To analyze sample molecules according to their m/z ratio, the molecules have to be ionized into the gas phase. This is typically performed in vacuum to prevent collision with air molecules leading to fragmentation of the molecule [87]. There are many ionization approaches available, but the analysis of peptides and proteins from biological samples typically involves so-called soft ionization techniques. Soft ionization methods are relatively non-destructive for the non-volatile proteins in the sample, which is important to prevent fragmentation of the protein molecules upon ionization. The two most commonly employed soft ionization techniques for biological samples, including protein ionization, are electrospray ionization (ESI) [88] and matrix assisted laser desorption ionization (MALDI) [89, 90]. This thesis will only focus on ionization of peptides and proteins using MALDI, of which a schematic overview is provided in Figure 4.
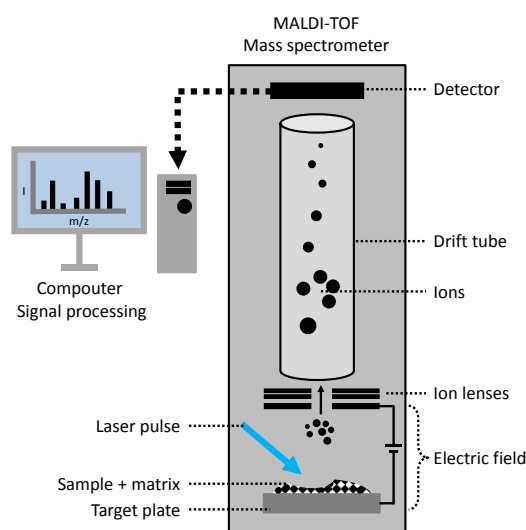
Figure 4. Schematic representation of a typical matrix assisted laser desorption ionization time of flight (MALDI-TOF) mass spectrometer and its main components. Sample (back) and an excess of matrix (white) are co-crystallized on a metal target plate and placed in the ion source, under vacuum. A pulsed laser (blue arrow) irradiates the sample and causes a cloud of sample and matrix to ablate from the target plate. An electric field is applied, providing the ionized molecules with kinetic energy. The ionized molecules are directed by ion lenses (black bars) into the drift tube, which separates the ions based on their TOF, after which they hit the detector. As the molecules' TOF is proportional to their relative mass and charge (m and z), the signal can be deconvoluted by a computer to provide a mass spectrum. In a mass spectrum the mass over charge value, m/z, is typically on the x-axis and the corresponding ion intensity (I) on the y-axis. Image inspired by [91].

15

For MALDI, protein samples are mixed with an excess of suitable photon energy absorbing, weakly acidic, organic matrix compound. Commonly used matrices for protein analysis are sinapinic acid (SA), dihydroxybenzoic (DHB) acid, and α-cyano-4-hydroxycinnamic acid (CHCA) (reviewed in [92]). Typically, the matrix is dissolved in a volatile liquid, such as acetonitrile or methanol, to speed up the crystallization process. The matrix is dissolved in combination with an acid, such as trifluoroacetic acid, to act as proton donor and contribute to the ionization process. For peptide analysis, and bacterial peptide profiling in particular, CHCA is the most commonly used matrix due to its excellent ability to ionize proteins in the 2–15 kDa mass range [93]. After mixing of the sample with the matrix, a droplet of this solution is deposited on a metal target plate and allowed to dry whilst forming crystals (see Figure 4). The metal target plate with the sample-matrix crystals is positioned into a vacuum chamber of the machine, and subsequently irradiated with a pulsed laser (blue arrow, Figure 4). Upon absorption of the laser energy by the matrix molecules, the energy is partially transferred to the proteins in the sample, causing ablation and desorption of the sample and matrix. The sample molecules, still under vacuum, are then ionized by transfer of protons, which produces predominantly singly charged ions [94, 95]. The cloud of ionized molecules is subsequently exposed to a constant electric field, and the ions are accelerated towards the mass analyzer, as depicted in Figure 4. Typically, a MALDI ion source is coupled to a time-of-flight mass analyzer (TOF system), also known as a drift tube. An electrical field of several kV accelerates the ions into the drift tube, after which they hit the detector. The kinetic energy (E_K) provided to each of the ions by the electric field is described by classical mechanics law, as expressed in Equation 1.

$$E_K = zU = \frac{1}{2}mv^2 \qquad\qquad \text{Equation 1}$$

In Equation 1, z is the charge (a dimensionless integer), U the applied electric potential (in Volt), and m being the mass (in Dalton) and v being the velocity of the ion (in meter/second). The energy provided to each ion is equal, and therefore their traveling velocity (in meter/second) through the drift tube of fixed length (in meter) is dependent on their respective mass (m) and charge (z). As the traveling time of the ions is proportional to their mass and charge (m/z value), the traveling time through the drift tube of fixed length provides information about their relative m/z.

The amount of times the ions strike the detector gives the arbitrary ion intensity of each ion in the mass spectrum. This signal is then processed and further analyzed by computer software to yield an interpretable mass spectrum. As the ions are predominantly singly charged due to inherent properties of MALDI ionization, the m/z value provides information about the mass of the analyte. The mass of the analyte can be calculated as described in Equation 2.

$$\frac{m}{z} = \frac{(\text{MW} + zH^+)}{z}$$
<div align="right">Equation 2</div>

In Equation 2, the *m* is the mass of the ion and *z* its charge (the *m/z* value in the mass spectrum), *MW* is the molecular weight of the analyte (in Da), *z* the number of protons (or charges) and *H⁺* the mass of a proton (in Da). General mass spectrum processing steps will be further discussed in the following section.

1.6 Mass spectral data processing

A typical MALDI-TOF mass spectrometry data set easily contains hundreds to thousands of spectra, with each spectrum in its turn containing hundreds to thousands of peaks with potentially relevant biological information [96]. Before one attempts to analyze, investigate, or compare these mass spectra, pre-processing of the mass spectra must be performed [97]. The processing of raw MALDI-TOF MS spectra typically involves, but is by no means limited to, the following general preprocessing steps: baseline correction, smoothing, normalization, peak alignment, and peak detection [96, 98]. A schematic representation of these pre-processing steps and their effect on a mass spectrum is depicted in Figure 5.
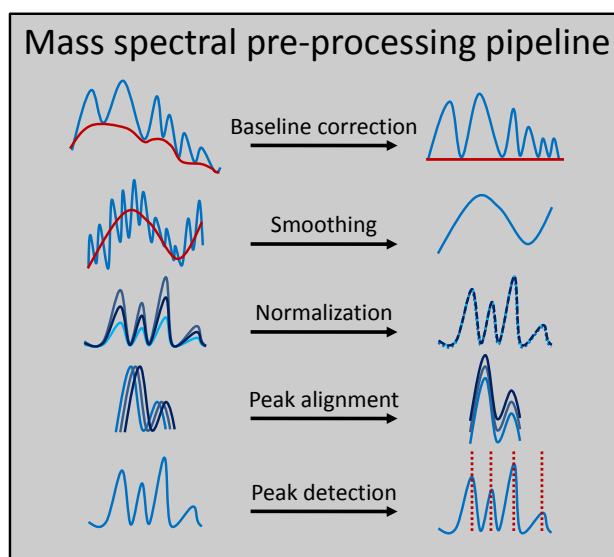
Figure 5. Typical steps performed in a mass spectral processing pipeline. In raw mass spectral data the baseline needs to be estimated and corrected to reduce noise. Additionally, a smoothing filter needs to be applied to remove high-frequency noise. Spectral intensity needs to be normalized across samples to allow a more direct comparison. Peak drift needs to be corrected by a peak alignment step. Lastly, peaks need to be detected using a peak detection algorithm. Image inspired by [99]

There have been numerous approaches published that perform the steps listed in Figure 5 using a variety mathematical approaches and techniques [96]. Several pre-processing pipelines are incorporated in proprietary software from the instrument manufacturers (such as FlexAnalysis and ClinProTools software by Bruker Daltonics), but there also exist freely available software packages that perform pre-processing steps on MALDI data, such as the MALDIquant [100] and MALDIrppa [101] packages developed in the *R* programming language, and other pipelines such as PROcess [102], Cromwell [103], and many others [104]. The first, and one of the most important steps in pre-processing, is baseline correction. Here, systematic artifacts and low-frequency noise are removed, which is typically observed in the lower m/z region (see Figure 5, top row). Baseline correction is usually performed by a so-called Top-Hat filter [105] or wavelet transform filter [106]. This involves a baseline estimation from the signal, and a subsequent baseline subtraction from the original signal [104]. The second pre-processing step is typically a smoothing procedure, which allows for the removal of high-frequency noise in the spectrum (see Figure 5). In general, this involves smoothing algorithms, such a Savitzky-Golay filter or moving average (or mean) filter [104]. The third step in the pre-processing sequence of mass spectra is normalization (sometimes referred to as standardization) of the signal. This step is performed to allow for comparison of the relative intensities of the peaks in mass spectra (see Figure 5) [107-109]. For MALDI-TOF data this is of particular importance as it is, at best, a semi-quantitative technique [110]. Normalizing of the signal resizes the ion count intensity (the y-axis) to range between 0 and 100% relative intensity. After normalization, it is common to rescale the largest peak in the mass spectrum to 100% relative intensity. For this, the total mass spectral intensity is divided by the total ion current (TIC, sometimes also referred to as total ion count), where the TIC can be calculated by integrating the area under the mass spectral curve [107, 108]. Alternatively, one can standardize the relative intensity to a (known) abundant reference peak, or only use a specific portion of the mass spectrum for normalization.

In general, the last steps of pre-processing pipeline involves peak alignment and peak detection (also referred to as peak picking), as shown in Figure 5. Peak alignment across different samples is required, as peak drifts are always present due to inherent calibration and peak detection issues, especially in low-resolution MALDI-TOF experimentation [96]. The peak drift has mainly a mechanical origin, where it can be influenced by sample spotting, instrument temperature, and laser attenuation and calibration parameters [111, 112]. With peak alignment, peaks are aligned to known peak locations on the m/z axis, thereby minimizing the absolute mass error. Alternatively, an internal calibration mixture can be added to the sample, consisting of molecules with a known mass. Typically the last pre-processing step, a peak picking algorithm is applied to detect local maxima, which correspond to ionized proteins [104]. Popular approaches for peak picking are signal-to-

noise ratio (SNR) [113], continues wavelet transform (CWT) [103], and Gaussian-based methods, among others [96, 114, 115].

1.7 Current applications of MALDI-TOF

MALDI-TOF mass spectrometry is widely used in the clinical environment to identify bacterial species based on their spectral differences, often referred to a biotyping [116, 117], where the basics of bacterial biotyping dates back several decades, to 1975 [118]. The comparison of MALDI-TOF spectra is mainly used to identify bacterial species, but subspecies differentiation, identification of resistance markers, and degradation products of antibiotics belongs to its capabilities as well [119-125]. Some of these methods, such as the one described by Sparbier and co-workers, require stable-isotope labeled reagents [126]. This requirement makes the application less straightforward and only detects general resistance to antibiotics. Sparbier and co-workers also developed an assay to replace conventional MIC determination assays [127]. Here, bacteria were grown in the presence of antibiotics and compared to a culture grown in the absence of antibiotics. After incubation with antibiotics, samples were spiked with an internal standard and growth inhibition was quantified based on relative signal intensity (the TIC in the mass spectrum). The MIC determination was found to be accurate, with >95% in agreement with reference values, but it must be noted that this study was only applied to one organism and one drug, *Klebsiella* sp. treated with meropenem. Although this is an innovative way of determining MIC values, the method does require (expensive) radiolabels. Similar applications using MALDI-TOF and stable isotope labeling are reviewed in [128]. Furthermore, this application of MALDI-TOF cannot be extended beyond the MIC determination application as it yields limit information: either growth is inhibited or not, based on observed isotope labeled peaks. Thus, that MALDI-TOF MS-based assay is not able to provide more detailed information about the antibiotic applied or its mechanism of action.

Besides the extensive applications of MALDI-TOF MS to investigate bacteria, fungal yeasts have also been investigated. Marinach and co-workers have applied MALDI-TOF MS to assess drug susceptibility of a yeast strain towards fluconazole, an antifungal agent [129]. Here, a dose-dependent change in the yeast's mass spectrum upon introduction of fluconazole was described. It was demonstrated that this method was reliable, accurate, and it was performed according to the Clinical Laboratory Standards Institute's (CLSI) laboratory practices [130]. Marinach and co-workers coined the term minimal profile change concentration (MPCC), defined as the lowest concentration value at which the mass spectrum profile changes. This work is similar to the work performed by Kostrzewa (associated with Bruker Daltonics) and co-workers, that linked the classical standardized CLSI method of MIC determination to MALDI-TOF MS data using a semi-quantitative method [127, 131-133], where the relative peak intensities are subsequently used as an indicator for

bacterial growth after isotope labeling. The applicability of this method for detection of drug susceptibility of mycobacteria was also shown [134]. All these mentioned MIC determination methods using MALDI have in common that they do not require an overnight culture in the presence of antibiotics, as an effect in the mass spectra was already detectable after 1-3 hours of incubation. This makes MALDI-TOF MS-based methods favorable over the classical MIC determination methods, which usually require incubation times overnight. However, as mentioned before, the MIC determination assays yield only limited information, as only the total area under the curve is taken as a measurement for relative growth. This means that the multiplex nature of MALDI-TOF MS is not used to its full potential.

MALDI-TOF's multiplex output has been used by Schott and co-workers, who have investigated the stress response of *Lactobacillus paracasei subsp. paracasei F19* after incubation with different stresses (such as osmotic stress, oxidative stress, starvation stress, pH induced stress) [135]. However, they concluded that principal component analysis (PCA) coupled with discriminant analysis did not allow for a distinction between several of the assayed stress conditions and the identification of biomarkers related to fitness and stress with MALDI-TOF MS is limited. Božik and co-workers found mass spectral responses of *E. coli* cells after exposure to essential oils to be similar to certain antibiotics, but data analysis was not pursued beyond unsupervised learning techniques such as clustering and PCA approaches [136]. MALDI-TOF MS also been applied for assay development using mammalian cells. Dong and co-workers [137] have shown the applicability of MALDI-TOF MS profiling to discriminate between healthy, apoptotic, and necrotic HeLa cells. In a similar manner, Kober and co-workers showed that mass spectra could assist in differentiating between toxic effects of three different environmental toxins (copper sulphate, acridine, and β-naphthoflavone) on a eukaryotic fish cell line [138]. Chiu and co-workers explored the use of MALDI-TOF MS to distinguish in vitro cellular responses resulting from the exposure of mammalian HepG2 cells to toxic chemicals [139]. Mass spectral changes were found upon treatment of cells with aflatoxin and hydrogen peroxide using descriptive PCA, but no peak evaluation or modeling was performed. Vanhara and co-workers showed the applicability of intact cell MALDI-TOF MS as a tool for quality control to reveal minute phenotypic changes of human embryonic stem cells [140].

The abovementioned studies for bacterial, fungal, and mammalian cell-based assays all describe phenotype changes in the respective cells, as determined by MALDI-TOF MS, but the corresponding data analytical approaches do not use the information density of the mass spectra to its full extent. In all cases, the analysis is dependent mostly on unsupervised machine learning techniques, such as descriptive PCA and clustering, and subsequent data evaluation is generally subjective, as it is mainly controlled by the experimenter. This means that data is not used to reach beyond the performed experiment, where it could be utilized to develop predictive approaches. Thus, previous research has reported on signals of the

potential application of MALDI-TOF MS to distinguish between (drug) stressed cells, but a holistic and objective evaluation and targeted utilization, beyond exploratory data analysis techniques of MALDI-TOF mass spectral data, is largely missing. To fill this gap, this thesis aims to evaluate and exploit drug response mass spectrometry profiles of whole-cells with the purpose of phenotypic drug screening by means of supervised machine learning techniques. The following section will give a brief overview of the difference between unsupervised and supervised machine learning approaches, and the required machine learning steps to reach the projected aim in more detail.

1.8 Machine learning approaches

A typical MALDI-TOF MS experiment yields a highly dimensional data set, composed of hundreds to thousands of mass spectra with hundreds of peaks per mass spectra. Visual interpretation of such vast numbers of spectra and corresponding peaks becomes infeasible, and objective multidimensional data analysis and machine learning tools are required [141]. In the field of machine learning, one can generally distinguish two different machine learning approaches: unsupervised and supervised machine learning [142, 143], as schematically depicted in Figure 6.
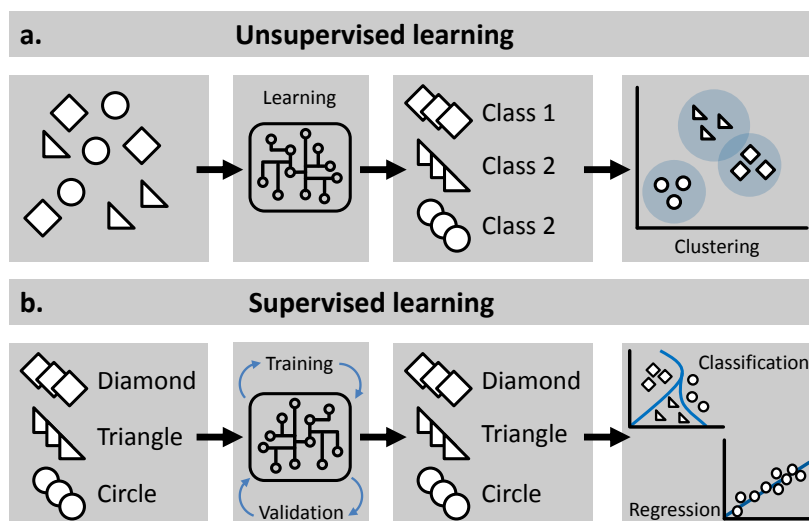
Figure 6 Schematic workflow of (a) unsupervised and (b) supervised machine learning. Unsupervised learning is mainly used for finding patterns in data using clustering approaches, without prior knowledge of underlying relations of the data set. Supervised machine learning uses labelled observations in a data set to train and validated a model. These models can be divided in classification and regression models, depending on whether the model concerns discrete or continuous data, respectively.

Unsupervised learning (top panels in Figure 6) focusses on exploratory data analysis and aims to find patterns or groups in the underlying data (the shapes in Figure 6), without the use of existing data labels. Techniques typically employed in unsupervised learning are principal component analysis (PCA) and cluster analysis [142]. This type of data analysis, sometimes also referred to as pattern recognition, aims to reveal the degree of similarity between data points [142].

Supervised learning algorithms (bottom panels in Figure 6) aim to train models which require input data (observations) and their corresponding output label or value (the name of the shape, in the example in Figure 6). Supervised machine learning aims to predict discrete (classification) or continues label values (regression) based on a training data set of observations and has the goal of generalizing observations in the training data set to unseen situations with reasonable accuracy [143]. Thus, the main difference between unsupervised and supervised learning is the labelling of the data, which in the case of supervised learning is used for training models. This training set has to consist of representative data, in order to prevent overfitting, bias, or overoptimistic performance results of the classification or regression model. Therefore, the data set size, composition, class labeling, and distribution has to be considered for practical implementations of the models [144]. As this thesis aims to train classification models to predict the activity or mechanism of action of drugs based on the mass spectral response of cells, the introduction to machine learning will focus on supervised learning and classification models only. Although supervised machine learning has a rich history in the context of (bacterial) identification and strain typing (listed in [145]), the application of supervised machine learning in the context of MALDI-TOF MS analysis to detect phenotypic changes is still largely unexploited.

There is a wide range of supervised learning algorithms available for classification purposes, and it is near to impossible to tell which model type works best for a particular problem beforehand [146]. Typical classification algorithms used in the field of bioinformatics, and particularly for MALDI-TOF MS data, are linear and quadratic discriminant classifiers, Naive Bayes classifiers, and k-Nearest Neighbor (kNN) [147]. More recently, the support vector machines (SVM), decision tree, and random forest based classification algorithms have gained popularity [143]. The choice for the most suitable classification algorithm is dependent on the inherent bias of certain algorithms and variance in the data it has to capture. An elaborate overview of classification algorithms can be found here [142].

A data set that is used for analysis consists of points that are measurable for each observation. These are commonly called features (also referred to as variables or attributes) [142]. For MALDI-TOF mass spectra, the peaks in the mass spectrum are considered features for investigation, but can also be (although less common) the complete continuous signal [148]. Features can be obtained from MALDI-TOF MS data by means of peak detection, one of the pre-processing steps discussed in section 1.6. In the context of machine learning, the

step of peak detection during pre-processing is referred to as feature extraction [96]. The selected features can subsequently be used to classify mass spectra, as was shown for the non-phenotypic applications strain typing and cancer detection [125, 149]. However, most peaks (features) in the mass spectrum do not contain discriminatory information to separate between classes and are considered redundant [96, 114]. To minimize the inclusion of noise and ensure inclusion of most of the discriminatory information, feature selection methods can be applied, where features are selected based on a certain selection criterion or threshold [147]. This step is also referred to as dimensionality reduction. Thus, reducing the number of features reduces the chances of fitting the model to noisy or non-informative variables in the data set. In addition to a reduction in noise, reducing feature set size using feature selection has shown to decrease the computational expense and model complexity [144]. These three effects result in an improved model performance for unseen data (generalization), faster model training, and a simplified model interpretation.

Feature selection algorithms can be divided into three different categories: filter, wrapper, and embedded type feature selection [143, 150]. Filter type feature selection algorithms evaluate feature importance based on characteristics of the feature itself, such as variance or relevance to the observed response [150]. Therefore, filtering methods have the inherent disadvantage that they are incapable of detecting synergistic feature-feature interactions, and do not incorporate information about the contribution of features to a specific classification problem. This may be disadvantageous for datasets with highly correlated features, as it can incorporate redundant information and may cause overfitting [151]. Wrapper methods partially overcome the weaknesses that filter methods possess, as it assesses features in the context of a specific classification algorithm. These methods are called wrapper methods, as the classification algorithm is said to be 'wrapped around' the features that are selected. In the context of MALDI-TOF MS, one of the most well-known wrapper methods is SVM-RFE (support vector machine recursive feature elimination), which is a form of sequential backward feature selection wrapped around a support vector machine classifier [152]. Although wrapper methods can provide feature sets with the desired classification characteristics, a main disadvantage of wrapper methods is that they are computationally expensive. Embedded feature selection methods are different than filter and wrapper methods, as the feature selection and learning algorithm interact with each other [153]. One of the most popular embedded methods is the random forest algorithm [154]. This algorithm combines the power of multiple decision trees to evaluate and select features to be incorporated.

After a model has been trained with the selected features, it needs to be evaluated to determine its overall performance. Typically, models are evaluated based on internal validation and external validation [155]. Internal validation is often performed by means of k-fold cross-validation. During a k-fold cross-validation step, the training data set is split into k partitions (folds), where k is often equal to ten. This is referred to as 10-fold cross-

validation. Stratified division of the training set data into k partitions is of importance to ensure equal representation of each class per fold. For 10-fold cross-validation, 90% of the training set data observations are used to train a model, and 10% of the observations are used to evaluate the resulting model's performance. This process is repeated until every partition of the 10-fold division is used as validation set once. The average outcome of cross-validation provides an estimate of the overall model performance. However, for proper model assessment, a model must also be evaluated using external data which was not used for model training, to determine how well the model generalized to unseen data [156]. This data set evaluation is referred to as external validation.

The performance of internal and external validation is typically evaluated based on precision, recall, and accuracy, and can visually presented by means of a confusion matrix [146]. A confusion matrix (sometimes referred to as an error matrix) is a table that lists the performance of a trained algorithm. An example confusion matrix is provided in Table 1. In this exemplary confusion matrix, a simple classification problem is described where one tries to identify apple objects from non-apple objects.

Table 1. A confusion matrix for the binary problem where one wants to classify apple objects from objects that are non-apples. Columns indicate model predictions, rows indicate true class of the objects.

		Model predicted class	
Class labels		Apple	Non-apple
True class	Apple	True positives	False positives
	Non-apple	False negatives	True negatives

In the confusion matrix for the exemplary binary problem in Table 1, the columns represent classification instances by the model and each row represents the corresponding true class of that observation. This means that all correct predictions end up on the diagonal (green in Table 1) and incorrect predictions end up outside the diagonal (red in Table 1), allowing for straightforward interpretation of prediction errors made by the classification algorithm. Usually, model performance is reflected by the overall accuracy, which is a number between 0 and 1. The overall accuracy is the amount of the true positives (the amount of apples that were correctly identified as apples) and true negatives (non-apple objects that were identified as such) divided by the total amount of observations (the total amount of objects classified by the model). An additional level of understanding of the model can be gained by also using the number of false positive (non-apple objects identified as apples) and false negative observations (apples that were classified as non-apple objects), shown in red in

24

Table 1. The true positive value and the false negative value can be used to calculate the recall of the model (also known as sensitivity or true positive rate). The recall reflects how well a model can detect the amount of positive cases out of all cases. The precision of the model (also known as the positive prediction value) reflects how well the model can correctly identify positive cases out of all positively identified cases. A more detailed description on how to obtain these values for binary and multiclass models is provided in the Experimental section, in subchapter 3.14. In summary, to construct a classification model for predictive whole cell phenotypic drug identification based on MALDI-TOF MS data, one must carefully select a classification model, the method of feature selection, and establish a systematic approach to evaluate model performance.

2 Research aim

Antibiotic drug discovery has long relied on natural product screening using simple growth inhibition assays. After the Golden Age of antibiotic drug discovery, most of nature's bioactive antibiotics had been found, namely the sulfonamides, β-lactams, macrolides, and tetracyclines. At the dawn genomics era, studies on isolated target proteins became widely available, but the target-based approaches failed to satisfy the ever-increasing demand for novel antibiotic drugs. One of the main reasons for this was that drug leads which showed promising target binding, proved incapable of significant activity on a cellular level due to the inability of crossing the bacterial cell wall and membrane. In addition, the focus on target-oriented approaches largely failed to deliver drugs that bind to new targets or have novel chemical scaffolds. These shortcomings of target-based assays are not only present in antibiotic drug discovery, but have been problematic in other drug screening fields as well, such as antifungal and anti-cancer drug research.

Recently, there has been a renewed appreciation for phenotypic cell-based screening assays in the area of drug discovery. Contrary to target-oriented approaches, cell-based assays have the advantage of inherently providing information about a drugs' cell permeability, which overcomes one of the most limiting factors and major hurdles for antibacterial drug development. By studying a drug's effect in a more pharmacological relevant environment, phenotypic assays have the potential to also provide essential information of the mechanism of action involved. This is a screening characteristic that target-oriented assays on isolated proteins are not able to provide.

Available phenotypic screenings in the context of antibiotic drug research, such as macromolecular synthesis assays, microarray profiling, cytological profiling, and Raman profiling, each have limitations of their own. Among the disadvantages of these assays are the use of (radio)labels, expensive reagents and specialized equipment, relatively low throughput, and use of genetically modified organisms. Moreover, most of these assays are unable to detect weakly active drugs, which could serve as potential drug leads, or lack the ability to provide molecular mechanism of action information.

To bridge the gap between current screening limitations and needs present in the drug discovery field, the main aim of this thesis was to develop a high-throughput, label-free, phenotypic cell-based assay with a sensitive analytical method which is able to detect a variety of sub-lethal stresses induced by antibiotic drugs in wild-type bacterial cell cultures. Furthermore, it was aimed to provide information about the mechanism of action of the applied stressor with the developed assay. As limitations of drug screening assays are shared between different drug development fields, an additional sub-aim of this work was to explore this concept beyond antibiotic drug screening for Gram-positive and Gram-negative bacteria. This was done by applying the developed workflow to eukaryote yeasts,

to investigate the effect of antifungal drugs, and human HeLa cells subjected to a variety of stressors.

To achieve the described aims, MALDI-TOF mass spectrometry was selected as analytical method, as it is relatively easy to use, high-throughput compatible, and requires minimal sample workup or fractionation to provide a detailed proteomic fingerprint of cells. Moreover, MALDI-TOF MS has already shown to be an excellent tool for identification of bacterial strains and other microorganisms. In this thesis, the applicability of MALDI-TOF MS was expanded towards phenotyping cells in response to drug treatment.

As MALDI-TOF MS is sensitive to fluctuations in experimental conditions, one of the experimental objectives was to standardize sample treatment and liquid handling procedures prior to mass spectral acquisition. Additionally, one of the objectives was to establish a mass spectral data pre-processing workflow to standardize processing of raw spectral data for the various assayed organisms. However, not all mass spectral variations can be controlled by experimental and spectral processing standardization, as there is inherently some degree of inter-day variability in obtained mass spectra. To circumvent the effects of inter-day spectral variation, a computational objective was to establish a data-dependent spectral analysis workflow.

To facilitate the identification of weakly active drugs in a screening setting, and provide information of the respective mechanism of action based on the proteomic response measured by MALDI-TOF MS, utilization and interpretation of the pre-processed data should be performed by a computational pipeline using machine learning approaches. This is required, as machine learning methods allow for pattern recognition in large, highly dimensional data sets. Therefore, one of the objectives was to design a computational pipeline which uses objective and data-dependent processing and analysis steps, which negates user interference and subjective interpretation of data. This versatile adaptability of the data analysis also prevents the use of a defined, static set of mass spectral peaks, making the computational pipeline transferable not only to different types of phenotypic stress responses, but also to different organisms and applications. Furthermore, to gain a flexible workflow and have control and understanding over all algorithms and variables within the complex data analysis, an objective was to implement all machine learning approaches in in-house developed programming scripts, which were established in the MATLAB programming environment. MATLAB has the advantage of being widely used in the academic environment. MATLAB also contains a wide array of multidimensional data analysis techniques in its Statistics and Machine Learning Toolbox and already contains specialized functions for handling mass spectrometry data in its BioInformatics Toolbox.

3 Experimental

3.1 Bacterial medium and antibiotics

All experiments using bacteria were performed using cation-adjusted Mueller-Hinton medium (MH medium; Sigma-Aldrich, Munich, Germany) prepared according to the manufacturers' guidelines. Antibiotics were selected to cover a diverse range of mechanisms of action, listed in Table 2 in chapter 4.1.1. The following antibiotics were dissolved in water: benzylpenicillin, cefotaxime, cefuroxime, moxifloxacin, and vancomycin. The following antibiotics were dissolved in dimethyl sulfoxide (DMSO) and water (50 v/v%): amoxicillin, ciprofloxacin, erythromycin, gentamicin, neomycin, tetracycline, trimethoprim, nitrofurantoin, and rifampicin. The following antibiotics were dissolved in DMSO: chloramphenicol, clarithromycin, and doxycycline. Antibiotics were dissolved to a final concentration of 1280 mg/L and filtered using a cellulose acetate membrane (0.2 µm pore size, GE Healthcare Life Science, Freiburg, Germany) to ensure sterility. Stock solutions were stored at -20 °C. Prior to use, antibiotic stock solutions were diluted in sterile cation-adjusted MH medium.

3.2 Bacterial MIC determination

The MICs of selected antibiotics were determined in accordance with the European Committee on Antimicrobial Susceptibility Testing (EUCAST) guidelines for antimicrobial susceptibility testing [157], as described in detail by Wiegand and coworkers [158]. The MIC was determined for the Gram-negative *Escherichia coli* strain (DSMZ 1103, equivalent to ATCC 25922) and the Gram-positive *Staphylococcus aureus* (DSMZ 2569, equivalent to ATCC 29213), obtained from the DSMZ (Deutsche Sammlung von Mikroorganismen und Zellkulturen; German collection of microorganisms and cell cultures).

3.3 Fungal MIC determination

All experiments on yeasts were performed using RPMI 1640 medium supplemented with L-glutamate, 2% glucose, phenol red, and buffered with sodium bicarbonate (Sigma-Aldrich, Munich, Germany).

Antifungal drugs used in this study were amphotericin-B, amorolfin, caspofungin, fluconazole, 5-fluocytosine, and miconazole, obtained from commercial suppliers. The MIC determination of antifungal drugs was performed as described by the European Committee on Antimicrobial Susceptibility Testing-Subcommittee on Antifungal Susceptibility Testing (EUCAST-AFST) guidelines [159] with minor alterations. In brief, *Candida albicans* (ATCC 90028) and *Saccharomyces cerevisiae* (wild-type, strain BY4742, a derivative of strain S288C,

a gift of Yaqing Zhang, Institute of Pharmacy and Molecular Biotechnology, Heidelberg University) was grown on yeast-peptone-dextrose (YPD) agar plates overnight. Five representative colonies were suspended in DPBS (Dulbecco's phosphate buffered saline, Sigma-Aldrich, Munich, Germany) and diluted to yield a cell density of McFarland 0.50, corresponding to approximately 3×10^6 colony forming units/mL (CFU/mL), as determined by colony plate count. The solution was subsequently diluted in RPMI 1640 medium to yield a cell density of approximately 3×10^5 CFU/mL. Drug stock solutions (in DMSO, sterile filtered) were diluted in RPMI 1640 medium and mixed 1:1 with 100 µL of yeast cells in a 96-well plate (polystyrene U-bottom; Greiner Bio-One GmbH, Frickenhausen, Germany) to yield a final inoculum of 1.5×10^5 CFU/mL. Plates were incubated overnight at 35 °C at 100% humidity, after which growth was assessed visually.

3.4 Toxicity assay HeLa

HeLa cells (HeLa-ACC57; obtained from DMSZ; Braunschweig, Germany) were grown in DMEM medium (Dulbecco's Modified Eagle's Medium, Sigma-Aldrich, Munich, Germany) supplemented with 10% fetal bovine serum (Gibco FBS, ThermoFisher Scientific, Waltham, MA, USA), penicillin and streptomycin (100 units/mL and 100 mg/L, respectively; Gibco, ThermoFisher Scientific, Waltham, MA, USA) to approximately 90% confluence at 37 °C in the presence of 5% CO_2 under humidified atmosphere in a tissue culture flask (T75, Saerstedt AG & Co. KG, Nuembrecht, Germany). Cells were washed with DPBS and harvested using the commercial available Accutase® cell detachment solution (Innovative cell technologies, Inc., San Diego, USA) according to the manufacturer's protocol. Cell seeding density was determined using a hemocytometer (Neubauer improved, Marienfeld Superior, Lauda-Koenigshofen, Germany) and adjusted to 20.000 cells/90 µL/well (96 well plate; Cellstar® polystyrene flat-bottom plates, Greiner Bio-One, Frickenhausen, Germany).

Drug solutions (10 µL/well) were mixed in the plate upon seeding cells and incubated for 24 hours at 37 °C under a humidified atmosphere in the presence of 5% CO_2 to determine CC_{50} values. Cell viability was assessed using the resazurin-based CellTiter-Blue® reagent (Promega Corporation, Madison, USA) by adding 20 µL of CellTiter-Blue® assay solution to each well. After incubation for 1-2 hours at 37 °C, fluorescence was measured at 570 nm and 600 nm using a FLUOstar Omega plate reader (BMG Labtech GmbH, Ortenberg, Germany). Data was exported in Microsoft Excel format. Using OriginPro software (version 2015; OriginLab Corporation, Northampton, USA) the data was fitted to a sigmoidal dose-response curve and the CC_{50} was determined.

3.5   Bacterial cell culture synchronization

The replication and division cycles of the bacteria cells were synchronized. For this, cells were grown in 50 mL tubes for approximately eight hours in MH medium in a Minitron incubator (Infors AG, Bottmingen, Switzerland) at 120 rotations per minute (rpm, 25 mm shaking throw) at 37 °C, after which cells were centrifuged at 2000×g for 10 minutes (Rotina 420R, Hettich Lab Technology, Tuttlingen, Germany). Residual medium was decanted to waste and the cell pellet was resuspended in sterile DPBS. Cell cultures were starved in this nutrient limited environment (120 rpm; at 37 °C) overnight for approximately 16 hours. After starvation, cells were centrifuged for 10 minutes at 2000×g. Supernatant was decanted to waste and cells were resupplied with fresh MH medium and diluted to a McFarland standard of 1.0. Cells were allowed to adapt to the nutrient rich medium for at least one division cycle (approximately 70 minutes in the case of *E. coli*; approximately 90 minutes in the case of *S. aureus*) to a McFarland of >2.0. Afterwards, the cells were added to the antibiotics in the 384-well plate at a final cell density with McFarland 1.0, corresponding to approximately 1×10^8 (CFU/mL).

3.6   Antibiotic treatment of bacteria

The concentrations at which experiments were performed are denoted as a fraction of the MIC in the following manner throughout the remainder of this work. For example, ⅛×MIC for an experiment performed at ⅛th of the MIC value. Cells were exposed to 1×, ½×, ¼×, ⅛×, $^1/_{16}$×, and $^1/_{32}$×MIC, unless indicated otherwise. Eight biological replicate cell cultures per concentration were prepared, to yield eight replicate mass spectra per assayed condition. Exposure of cells to antibiotics was performed in clear polystyrene 384-well plates (flat-bottom; Greiner Bio-One GmbH, Frickenhausen, Germany). Concentrations of each antibiotic (2-fold dilution series in cation-adjusted MH medium) were made to ensure that the highest final assay concentration was 1×MIC the respective antibiotic. First, 50 μL of antibiotic stock (2×MIC) solution was added to each well. Subsequently an inoculum of 50 μL with 2×10^8 CFU/mL was added to the plates using a semi-automatic liquid handling station (VIAFLO 384, INTEGRA Biosciences GmbH, Biebertal, Germany; equipped with 384-channel head) to ensure final cell density of 1×10^8 CFU/mL. Plates were sealed using sealing film (SealPlate® film, Excel Scientific Inc., Victorville, CA, USA) and placed in a preheated microplate incubator (Thermo Scientific iEMS Incubator/Shaker, ThermoFisher Scientific, Waltham, MA, USA) at 37 °C and shaken at 1150 rpm for 2 hours.

3.7 Antifungal treatment of yeasts

Exposure of yeast cells to antifungals was performed in clear polystyrene 384-well plates (Flat-bottom; Greiner Bio-One GmbH, Frickenhausen, Germany). Concentrations of each antifungal (2-fold dilution series in RPMI 1640) were made to ensure that the highest final assay concentration was 1×MIC. To each well, 10 µL of antifungal stock solution was added using the VIAFLO 384 semi-automatic liquid handling. Subsequently an inoculum of 90 µL with a McFarland standard of 4.4 was added to the plates using the VIAFLO 384 semi-automatic liquid handling station. This ensured a final cell concentration which corresponds to an approximate cell density of 2.5×10^7 (CFU/mL). Plates were sealed using sealing film (SealPlate® film, Excel Scientific Inc, Victorville, CA, USA) and placed in a preheated microplate incubator (Thermo Scientific iEMS Incubator/Shaker, ThermoFisher Scientific, Waltham, MA, USA) at 35 °C and shaken at 1150 rotations per minute for 2 hours. In the case of *S. cerevisiae* (strain BY4742), cells were treated with amphotericin-B, amorolfin, caspofungin, and fluconazole at concentrations ranging 1×, ½×, and ¼×MIC. In the case of *C. albicans* (ATCC 90028), assay was performed using 5-fluocytosine, amphotericin-B, caspofungin, fluconazole, and miconazole at concentrations ranging 1×, ½×, and ¼×MIC.

3.8 Treatment of HeLa cells

HeLa cells were seeded with a density of 20.000 cells/well in absence or presence of drugs at previously determined CC_{50} in a total volume of 100 µL DMEM supplemented with penicillin, streptomycin, and 10% FCS in a 96-well plate (Cellstar® polystyrene flat-bottom plates, Greiner Bio-One, Frickenhausen, Germany). Cell cultures were grown overnight for approximately 16 hours at 37 °C in the presence of 5% CO_2 and saturated humidity, after which they were harvested.

In experiments where cells were subjected to ultraviolet (UV) light and elevated temperatures, overnight cell cultures were treated as follows: in the case of incubation at elevated temperature, the plate was placed in an incubator for 3 hours at 43 °C with atmospheric CO_2 levels (approximately 410 ppm, as of 2019) and saturated humidity. After subjection to the thermal stress, cells were placed back in the incubator at 37 °C, 5% CO_2, and saturated humidity for an additional hour to recover. For to the exposure to UV light, cells were exposed to 5, 10, and 15 minutes UV radiation, by placing the 96-well plate on a piece of non-reflective paper in a Captair workstation (Captair Biocap RNA/DNA, Erlab DFS SAS, Val-de-Reuil, France), right below (0.5 m) the germicidal lamp (Sylvania G15W lamp, peak wavelength 255 nm, Feilo Sylvania Germany GmbH, Germany). Cells were incubated for another hour at 37 °C and 5% CO_2 before harvesting.

3.9 Sample preparation

For bacteria and yeasts, after incubation the 384-well plates were centrifuged (Rotina 420R, Hettich Lab Technology, Tuttlingen, Germany, equipped with a swinging bucket rotor) at 2000×g for 10 minutes. Supernatant was discarded and cell pellets were washed with 100 µL 35% ethanol (v/v%) and incubated in the microplate incubator for 5 minutes at 1150 rpm. Cell debris was centrifuged again and washed a second time with 100 µL of 35% ethanol. After removal of 90 µL the supernatant, cells were resuspended in the remaining 10 µL 35% ethanol, sealed, and stored at 4 °C. Prior to MALDI-TOF MS analysis, cell pellets were resuspended in the plate by shaking in the microplate incubator for 5 minutes at 1150 rpm. Cell suspension (3 µL) was mixed in 1:1 ratio with freshly prepared α-cyano-4-hydroxycinnamic acid (CHCA; 10 mg/mL in 50.0% acetonitrile, 47.5% H_2O, and 2.5% trifluoroacetic acid) by aspirating the matrix and sample sequentially using the VIAFLO 384 automatic pipettor, followed an air gap of 3 µL. Then, 1.5 µL was spotted on a MALDI target plate (MSP 96 polished steel BC microScout target, Bruker Daltonics, Bremen, Germany). Samples were air-dried at room temperature before being placed in the mass spectrometer.

In the case of experiments with HeLa cells, cells were washed in the 96-well plate with 100 µL DPBS and resuspended in ice-cold 50 µL 35% ethanol. Using a disposable micropipette tip the well surface was scratched manually to promote cells detachment. The cell suspension was mixed with CHCA matrix and spotted as described above using a VOYAGER adjustable spacing multichannel pipette (12.5 µL capacity, INTEGRA Biosciences GmbH, Biebertal, Germany).

3.10 MALDI-TOF settings

Target plates were positioned in the mass spectrometer (MALDI-TOF microflex LT, Bruker Daltonics, Bremen, Germany) fitted with a nitrogen laser (337 nm, set to 60 Hz). Spectra were acquired in linear mode with a mass range of m/z 2,000-15,000 using AutoXecute runs of the FlexControl software (Version 3.3, Build 108.2, Bruker Daltonics). The laser was set to fire 100 shots at 80% power (approximately 52 µJ) per location, with the attenuator set to range 22-30%, while moving in a small spiral raster over 7 locations per sample spot to assure appropriate signal intensity. The sum of 700 shots yielded spectra with ion intensities in the order of 10^4-10^5 ion counts for the most abundant ions. Sample rate was set to 1.00 GS/s; detector gain was set to 3.7×; electronic gain was set to 200 mV and the *Realtime Smooth* function was disabled. Default delayed ion extraction was fixed at 140 ns. Calibration of the instrument was regularly evaluated using Bruker Daltonics *Protein Calibration Mix I* and, if necessary, adjusted according to manufacturer's guidelines to be within 300 ppm.

3.11 Spectral pre-processing

Using Bruker's FlexAnalysis software, the collected raw spectra were exported to a *.txt-file in ASCII format using a custom script. Subsequently, the spectra were imported in MATLAB (R2018a; The MathWorks Inc., Natick, USA) installed on a desktop PC (i5-4690 CPU @3.50GHz equipped with 16 GB RAM and a 64-bit Windows 7 Professional operating system) and pre-processed using an in-house developed MATLAB script. First, spectra were resampled (MATLAB function *resample(MZ, Y, MZ, 'showplot', 'off');*) to 30000 data points in order to obtain a homogenous mass/charge (m/z) vector for each sample in the range of m/z 3850-15000. The baseline of each individual spectrum was estimated and subtracted using a sliding window filter (MATLAB function *msbackadj(MZ, Y, 'STEP', 25, 'WINDOW',50);*). Noise was reduced using locally weighted scatter plot smoothing regression method (commonly referred to as LOWESS filter; MATLAB function *mslowess(MZ, Y, 'span', 50, 'RobustIterations', 1);*). Spectra were normalized to their total ion current (TIC; MATLAB function *msnorm(MZ, Y, 'LIMITS', [3850 15000], 'method', 'mean', 'MAX', 100);*) and rescaled such that the highest peak in each mass spectrum had a relative intensity of 100%. For *S. cerevisiae*, the mass limits were set to range m/z 2520 -10000.

Each mass spectrum was aligned towards known, conserved, high intensity peaks (MATLAB function *msalign*). By aligning spectra during the initial processing step towards several of these highly intense and consistently observed peaks, errors in peak location are reduced before peak detection is performed. The majority of the proteins that can be observed in a typical bacterial mass spectrum are large (50S) and small (30S) ribosome-associated proteins (RL and RS) [160]. Peaks in the observed mass spectra were tentatively identified using the TagIdent tool [161]. The following reference proteome sets in the UniProt database [162] have been used: up000000625 (*E. coli*), UP000008816 (*S. aureus*), UP000000559 (*C. albicans*), UP000002311 (*S. cerevisiae*), and UP000005640 (Human reference proteome). For *E. coli* and *S. aureus*, only reviewed proteins in the UniProt database (release 2019_11) were considered. Subsequently, average m/z and theoretical isoelectric points (pI's) of proteins were calculated using the primary sequence data and the Fragment Ion Calculator [163]. Details of the alignment peaks of the respective organisms are provided in the corresponding chapters (*E. coli*: Table 4; *S. aureus*: Table 12; *S. cerevisiae*: Table 22; *C. albicans*: Table 28; HeLa: Table 32).

A peak detection algorithm based on the undecimated discrete wavelet transform was applied on the average spectrum of replicate experiments to identify centroid peak locations [103, 141] (MATLAB function *mspeaks*). Subsequently, peak binning was performed to obtain a common m/z vector to describe the peaks observed in the spectra. This yielded a common m/z vector containing 175 peaks in the m/z 3850-15000 Da region in the case of *E. coli*. Comparable numbers of peaks were observed for mass spectra of *S. aureus* (135 peaks, in the range of m/z 2520-10000), *S. cerevisiae* (139-155 peaks,

depending on experiment), *C. albicans* (88 peaks) and HeLa cells (127-158 peaks, depending on experiment).

3.12 Spectral quality control

Spectral quality control procedures as described in this section were applied to all mass spectra, regardless of the organism, unless indicated otherwise. The TIC value was used as a unit of measure for spectral quality. This eliminates the requirement to visually inspect each spectrum, which is a laborious and subjective task. Instead, the TIC allows for an objective evaluation of the mass spectrum signal quality. Based on the TIC values of the whole dataset, the data was grouped into quartiles (Q). Subsequently, the interquartile range (IQR) of the TIC was calculated. To determine outliers spectra from the bulk TIC data, the upper fence (UF) and the lower fence (LF) were computed using Equation 3 and Equation 4, as described previously by Tukey and coworkers [164, 165].

$$UF = Q3 + 1.5 \times IQR \qquad \text{Equation 3}$$

$$LF = Q1 + 1.5 \times IQR \qquad \text{Equation 4}$$

In Equation 3 and Equation 4, Q3 represents the third quartile (75th percentile) and Q1 the first quartile (25th percentile) of the TIC values. Spectra with TIC values above the upper fence or below the lower fence were considered outliers and removed from the data set.

In addition, an outlier filter was added that removes any spectrum of which the intensity was higher than the upper fence based on the intensity of the mass spectrum at m/z 12500, where for all organisms (unless indicated otherwise) no peak was observed. At that position in the mass spectrum, the relative intensity should be equal to the background signal and is expected to be low (generally <1.5% relative intensity). Thus, the relative intensity at this m/z provides an easy way of removing spectra with poor (noisy) signal quality. The relative intensity at m/z 12500 was determined for each spectrum. Subsequently, the UF and the LF of the relative intensity at m/z 12500 was computed in a similar fashion as for the TIC values (see Equation 3). As a threshold, spectra with relative intensity above Q3+2×IQR were removed. In practice, this threshold meant that all spectra with intensity roughly above 1-1.5% at m/z 12500 were removed. For experiments with *S. cerevisiae*, this threshold was determined at m/z 9000.

3.13 Feature selection

Not all peaks in the mass spectra contain sufficient discriminatory information for model construction. Peaks need to be removed from the data set, as some peaks might cause

overcomplicating and overfitting (poor generalization) of the models. Therefore, two types of feature selection algorithms have been applied in order to remove noisy and redundant peaks: (1) a random forest (RF) of decision trees and (2) sequential (forward; SFS and backward; SBS) feature selection. Using these three subsets of features, an additional feature subset was created, which contained the aggregated features which were selected by two or all three of the applied feature selection methods (RF, SFS, and SBS).

Firstly, the relative feature importance was determined by evaluating the out-of-bag error (OOB error) using a random forest of decision trees, a so-called embedded feature selection method [154]. The evaluation of feature importance was performed for two different scenarios with different class labelling: (1) by using binary labelling of the data: spectra were labelled either as 'treated' or 'untreated' with a drug or stressor, regardless of the drugs' mechanism of action or concentration. The second labelling (2) was done according to drug mechanism of action, regardless of drug concentration.

Peak selection was based on the relative contribution to the correct classification of binary and multiclass mechanism of action problems. For this, a bootstrap aggregated (bagged) random forest of 200 (in case of binary classification), or 250 (in case of multiclass MoA classification) of decision trees was grown (MATLAB function *TreeBagger*). Subsequently, the OOB error was evaluated. By evaluating the OOB error, the relative importance of each peak regarding its impact on classification performance was given a score. As a threshold, features with a relative feature importance higher than the mean importance plus 1.5× standard deviation of the relative feature importance were considered for incorporation in the models.

Next, sequential forward and backward feature selection (wrapper methods) were used to select a subset of peaks that best classifies the data. Features considered for sequential feature selection were only the features that had a relative feature importance higher than the mean feature importance minus 1× standard deviation as determined by the RF. This was done in order to reduce calculation time, as sequential feature selection is a computationally expensive method.

For sequential forward feature selection (SFS), a subset of features was selected that best classified the data until there was no improvement in classification accuracy. This was done by creating an initial empty feature subset and subsequently adding more features (MATLAB function *sequentialfs*). After the addition of each feature, the classification performance of a linear discriminant classifier was evaluated using 10-fold cross-validation. For each fold, the number of misclassified samples (misclassification rate) for was determined. As a stopping criterion for sequential feature selection, the minimum misclassification rate was taken. This was defined as the point where the misclassification rate did not decrease anymore upon adding more features, and sequential feature selection stopped. The process of SFS was performed 100 times. Based on the 100 iterations of sequential feature selection, a final

feature set selected by SFS was created based on the average amount of times they were selected out of the 100 iterations. As selection threshold, features were considered for modeling if they were selected more than the mean amount of times they were selected plus 1.5× standard deviations the total amount they were selected. If selection threshold happened to be >100, which would result in no features being selected, a threshold of >99 was taken. In the case of *C. albicans* the selection threshold of SFS was set to the mean amount of times features were selected for data set complexity reasons.

Additionally, sequential backward selection (SBS) was performed, where initially all features (that is: only the features with a relative feature importance higher than the mean feature importance minus one standard deviation as determined by the RF) were considered. For SBS, features were removed from the initial subset until accuracy no longer improved (according to the same criterion stated for SFS). The process of SBS was performed 100 times. Out of the 100 iterations of SBS, only those features were considered for modeling according to the same selection criteria stated for SFS.

Using the three sets of features selected by the RF, and the SFS and SBS procedures, a fourth set was created by aggregating the selected features into one set. As a threshold, only features selected by two or all three of the feature selection methods were included in this aggregated feature set.

3.14 Modelling and model evaluation

For *E. coli*, several classification models were constructed employing MATLAB's default settings. The models that were built are as follows: linear and quadratic discriminant classifier, Naïve Bayes classifier, Support vector machine (SVM) classifiers using linear, quadratic, cubic, and Gaussian kernel functions, k-nearest neighbor (KNN) with a cosine kernel and a decision tree. Each of the models was constructed using the feature sets selected by the RF, SFS, SBS, and the aggregated feature set.

For *E. coli*, two classification types for all models were extensively evaluated for each feature set: firstly a binary model, which should identify only whether a mass spectrum originated form a cell culture treated with an antibiotic or not, and secondly, a model that would identify the mechanism of action with which the cells were treated.

Evaluation of the models was done using stratified 10-fold cross validation. This means that the data was partitioned into ten subpopulations (folds) using proportional inclusion of data from each class. The model is then trained using data out of nine folds, and is evaluated based on the remaining 10th fold. This process is repeated and the overall model accuracy is averaged over the ten folds.

Model performance was evaluated with the overall accuracy, a number between 0 and 1, indicating the fraction of spectra classified correctly (see Equation 5). In addition, for each class in the models, the recall and precision for each class are given, calculated according to Equation 6 and Equation 7, respectively.

$$Overall\ accuracy = \frac{(amount\ of\ positive\ samples)}{(amount\ of\ samples)} \qquad \text{Equation 5}$$

$$Recall = \frac{(true\ positives)}{(true\ positives + false\ negatives)} \qquad \text{Equation 6}$$

$$Precision = \frac{(true\ positives)}{(true\ positives + false\ positives)} \qquad \text{Equation 7}$$

The recall value (also known as sensitivity) is the fraction of correct predictions (true positives) divided by the sum of the correct (true positives) and incorrect (false negatives) classified samples. The precision (also known as positive prediction value) is defined as the amount of correctly classified samples (true positives) divided by the sum of the true positives and the false positives. Both precision and recall also yield a number between 0 and 1, the higher the number, the better the model performs.

Based on the results from *E. coli*, it was found that SVMs with a quadratic kernel (Q-SVM) built with the aggregated feature sets performed best. Therefore, for the other organisms and drugs mentioned, only the aggregated feature sets and Q-SVM classification models are discussed.

3.15 External validation

For *E. coli*, *S. aureus*, and *S. cerevisiae*, trained classification models were externally validated by classifying drugs' activity and drugs' mechanism of action on novel data, which was not included in the model training phase. External validation was performed with a blind set of 20 drug compounds for *E. coli* and *S. aureus* and with a set of eight drugs for *S. cerevisiae*. These compounds were subjected to the screening method using a fixed and typical concentration in high-throughput screening campaigns of 10 µM. For the external validation, two models were built for each organism: one model was built as a binary classifier, returning only whether spectra belonged to cells treated with an antibiotic or antifungal drug (outcome 'treated') or is untreated (outcome 'untreated'). The second model used the mechanism of action of the antibiotics or antifungal drugs as class labels (see Table 2, Table 11, Table 21, Table 27, and Table 31 for *E. coli*, *S. aureus*, *S. cerevisiae*, *C. albicans*, and HeLa cells, respectively).

In the case of *S. aureus*, treatment of cells with some of the drug compounds yielded spectra that did not pass the spectra quality control thresholds and, therefore, no classification could be performed. For these compounds, it was assumed that the spectra were of insufficient quality due to the fact that the cells were treated with such relative large amounts of antibiotic (>>MIC) that not enough cells had grown to generate a mass spectral signal. These compounds were screened again at a 1 μM screening concentration instead of 10 μM. In that case, the training set for internal validation was reduced to include 13 antibiotics. The antibiotics amoxicillin, cefotaxime, cefuroxime, chloramphenicol, clarithromycin, doxycycline, erythromycin, gentamycin, moxifloxacin, neomycin, penicillin, rifampicin and trimethoprim) at concentrations ranging only from 1×MIC to $^{1}/_{8}$xMIC (instead of down to $^{1}/_{32}$×MIC) were included, thereby reducing the data set.

4 Results & Discussion

In the following subchapter, the development of the drug screening assay will be extensively presented and discussed with reference to *E. coli* and the treatment with antibiotics (subchapter 4.1). In the subsequent subchapters, the application of the method is demonstrated on the Gram-positive bacterium *S. aureus* (subchapter 4.2), the eukaryote fungi *S. cerevisiae* (subchapter 4.3.1) and *C. albicans* (subchapter 4.3.2), and lastly on the mammalian human HeLa cell line (subchapter 4.4). In the first sections of the *E. coli* subchapter (4.1), the determination of the MIC, cell synchronization, and detailed insights on peak pre-processing of the mass spectra for *E. coli* will be discussed in more depth, which is largely omitted for the other organisms.

4.1 Escherichia coli

4.1.1 Minimal inhibitory concentration determination

The minimal inhibitory concentration (MIC) values were determined using the broth microdilution method [157, 158]. MIC values found for *E. coli* are listed in Table 2. The MIC values were within the acceptable range (± two dilution steps) of the reference values, as determined by the EUCAST guidelines, and were used as benchmark values for treatment of *E. coli* for the MALDI-TOF MS-based assay. It must be noted that the proposed MALDI-TOF based assay uses relatively high cell densities (10^8 CFU/mL) and short incubation times (2 hours) compared to the MIC determination protocol (10^4 CFU/mL and overnight incubation), two factors known to cause deviations of the actual MIC [158]. However, it has been shown that the combination of such high cell densities with short incubation times can be used to accurately determine the MIC using MALDI-TOF MS [127, 166], and therefore it is assumed that the determined MIC values with the broth microdilution method are proper benchmarks for the proposed MALDI-TOF MS assay.

Table 2. List of antibiotics used for *E. coli* (reference strain ATCC 25922) experiments. Indicated is the antibiotic chemical class and main target, next to the mechanism of action (MoA) abbreviation used for classification model training (CWL: cell wall synthesis, NUC: nucleic acid synthesis/repair, PRT: protein synthesis, and OTH: other mechanism of action), and the antibiotics' respective minimal inhibitory concentration (MIC) values (mg/L) according to reference values by European Committee on Antimicrobial Susceptibility Testing (EUCAST) and as determined in this thesis. NA = not available.

Antibiotic	Chemical class, main target	MoA class	EUCAST [157] MIC (mg/L)	This thesis MIC (mg/L)
Amoxicillin	β-lactam, DD-transpeptidase inhibitor	CWL	4	8
Benzylpenicillin	β-lactam, DD-transpeptidase inhibitor	CWL	NA	32
Cefotaxime	β-lactam, DD-transpeptidase inhibitor	CWL	0.06	0.031
Cefuroxime	β-lactam, DD-transpeptidase inhibitor	CWL	4	8
Chloramphenicol	Inhibits peptidyl transferase	PRT	8	8
Ciprofloxacin	Fluoroquinolones inhibiting DNA gyrase and topoisomerase IV	NUC	0.02	0.004
Clarithromycin	Macrolide, binds to the 50s ribosomal subunits, inhibiting peptidyl transfer	PRT	NA	16
Doxycycline	Tetracycline, steric hindrance of A-site by binding 30S ribosomal subunit	PRT	2	2
Erythromycin	Macrolide, binds to the 50s ribosomal subunits, inhibiting peptidyl transfer	PRT	NA	32
Gentamicin	Macrolide, binds to the 50s ribosomal subunits, inhibiting peptidyl transfer	PRT	0.5	1
Moxifloxacin	Fluoroquinolone, inhibiting DNA gyrase and topoisomerase IV	NUC	0.06	0.063
Neomycin	Macrolide, binds to the 50s ribosomal subunits, inhibiting peptidyl transfer	PRT	1	2
Nitrofurantoin	Nitrofuran, reactive metabolites damage macromolecules	OTH	NA	16
Rifampicin	Rifamycin, inhibits DNA-dependent RNA polymerase	OTH	NA	16
Tetracycline	Tetracycline, steric hindrance of A-site by binding 30S ribosomal subunit	PRT	2	1
Trimethoprim	Dihydrofolate reductase inhibitor	NUC	0.5	2
Vancomycin	Glycopeptide, steric hindrance of terminal D-alanyl-D-alanine moieties	CWL	NA	128

To construct a model that is able to identify weakly active antibiotic compounds, the determined MIC values were used as an upper boundary of drug screening concentration. Starting from 1×MIC, a 2-fold serial dilution series was prepared and bacterial cultures were treated with a fraction of the MIC (i.e., ½ times the MIC, ¼ times the MIC, and ⅛ times the MIC). For example, amoxicillin was used at 8 mg/L, 4 mg/L, 2 mg/L, 1 mg/L, and 0.5 mg/L. Implementing these concentrations allows one to train a model for sub-lethal variations in the mass spectra. This may lead to the detection of antibiotics that would be missed by conventional growth inhibition assays, which will only pick up strongly active compounds inhibiting growth.

4.1.2   Cell synchronization

In initial experiments it was observed that despite constant inoculum density (measured in McFarland units) and viable cell count (colony forming units/mL, measured by means of agar plating), *E. coli* cell cultures showed considerable differences in their mass spectra at

different days of experimentation. It is known that a culture of *E. coli* cells within a constant environment (i.e., exponential growth phase) shows a variability in growth rate, generation time, and cell size [167]. To circumvent dealing with such a heterogeneous cell culture, and thereby avoiding considerable differences between mass spectra of cell cultures beyond the inter-day differences that are present, the *E. coli* cells' replication and division cycles of each culture batch were synchronized. For this, *E. coli* cell cultures are grown in a nutrient-limiting environment, which exhibits synchronous division after supplementation with a complete medium [168, 169]. For the proposed MALDI-TOF screening assay, cells were starved of essential nutrients in DPBS, after which they were supplemented with fresh MH medium. The starvation period arrests all cells at the same point in their cell division cycle and the subsequent fresh MH medium supply causes the cell culture to undergo synchronized division. After overnight starvation in DPBS, a McFarland value of 1.0 corresponded to approximately 1×10^8 CFU/mL. Cells were allowed to adapt to the nutrient rich medium for at least one division cycle, which was approximately 70 minutes in the case of *E. coli* to a McFarland of 2.0 before addition of antibiotics. An exemplary figure of synchronization results of *E. coli* cells is provided in Appendix Figure 1.

The average mass spectral intensities at the reference peaks from synchronized cells were compared with unsynchronized cells to show the effect of synchronization on the mass spectral intensity deviation. For this comparison study, the *E. coli* cell cultures were not treated with antibiotics. At the reference peaks (see Table 4 in section 4.1.3 for details), the average intensity and the mean absolute deviation (MAD) were determined. The results are listed in Table 3.

Table 3. Average relative intensity (I; in %) and mean absolute deviation (MAD; in percent point) of alignment peaks before and after synchronization of the cells. RL = ribosomal large subunit, RS = ribosomal small subunit, UniProtKB accession number is indicated for each protein.

			unsynchronized		synchronized		
m/z	Name	UniProtKB	I (%)	MAD (%.)	I (%)	MAD (%.)	MAD reduction (%)
4365.3	RL36	P0A7Q6	97.1	2.8	99.3	0.3	89
5381.4	RL34	P0A7P5	85.6	8.4	64.7	8.2	3
6255.4	RL33	P0A7N9	73.4	7.8	63.9	3.9	50
6316.2	RL32	P0A7N4	52.8	5.2	46.5	2.8	47
7158.7	RL35	P0A7Q1	38.4	9.6	18.3	5.5	42
7274.5	RL29	P0A7M6	60.8	10.2	30.3	7.0	32
10300.1	RS19	P0A7U3	13.6	2.5	5.2	1.6	37

Table 2 shows a reduction in the MAD for each reference peak, with an average of 43% for each of the reference peaks. For the peak at m/z 4365.3 (RL36; P0A7Q6; the highest peak in the spectrum), the MAD is even reduced by 89% (from 2.8% to 0.3% relative intensity). For

the peak at m/z 5381.4 (RL34; P0A7P5), the average intensity change was smallest (from 8.4% to 8.2%), represented by a 3% MAD reduction. Thus, the synchronization of the cells assists in eliminating unnecessary errors (noise) from the data, as the MAD of replicate spectra is decreased compared to unsynchronized cells.

4.1.3 Peak alignment

Mass spectra need to be preprocessed before they can be properly analyzed, as a typical raw mass spectrum contains several noise elements. This includes, but is not limited to, electrical signal noise, chemical noise, and noise introduced by temperature fluctuations of the flight tube [112]. Most of these noises can be removed with established pre-processing techniques such as smoothing, baseline correcting, and normalization of the mass spectral signal [96]. However, a degree of peak drift remains in the MALDI-TOF mass spectra, due to small fluctuations in the time-of-flight of the molecules [112]. This can be corrected for by aligning the mass spectra to known reference peaks of the mass spectrum. For this pre-processing step, it is required to select highly abundant and consistently present reference peaks across the whole m/z range, as the mass drift can be non-linear [170]. In the case of *E. coli*, a set of reference peaks across the range of m/z 4000-10000 was selected, consisting of peaks from proteins which were either previously identified by Arnold and Reilly [160] or are part of Bruker's calibration kit. By identifying several of these high abundant proteins and aligning the mass spectra accordingly, the errors in peak locations across the mass spectrum were reduced. Listed in Table 4 are the errors observed for the selected reference peaks after alignment in mass spectra from *E. coli* (inset in Table 4).

Table 4. Reference peaks used for spectra alignment during spectral processing of *E. coli* data set. Listed is the respective protein name, where RL corresponds to Ribosomal Large subunit (50S) and RS to Ribosomal Small subunit (30S), followed by the respective protein unit number. Second column lists corresponding UniProtKB accession number, third column indicates whether the initiator methionine (M) is removed. Fourth column lists the theoretical m/z value, followed by the observed m/z value in the fifth column. Sixth column lists absolute mass error in ppm. Last column shows theoretically calculated isoelectric point (pI). Inset on the right shows average mass spectrum of *E. coli* with asterisk indicating reference peaks.

Name	UniProtKB	M removed	Theoretical m/z	Observed m/z	Error (ppm)	pI
RL36	P0A7Q6	No	4365.3	4366.0	148	10.7
RL34	P0A7P5	No	5381.4	5382.2	145	13.0
RL33	P0A7N9	Yes	6255.4	6256.2	127	10.2
RL32	P0A7N4	Yes	6316.2	6316.6	59	11.0
RL35	P0A7Q1	Yes	7158.7	7159.2	69	11.8
RL29	P0A7M6	No	7274.5	7275.0	72	10.0
RS19	P0A7U3	Yes	10300.1	10300.7	55	10.5
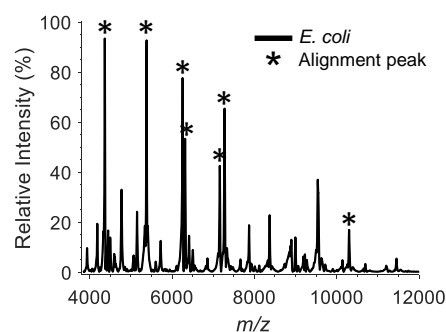
Multiple high-abundance proteins have been previously identified in mass spectra of *E. coli* [160, 171, 172], with the majority being ribosomal proteins. The mass spectra contain a large number of ribosomal associated proteins as these are relatively abundant (up to 21% of a cell's protein content is ribosomal), and have a relatively high isoelectric point (pI >10.0), which makes them highly ionizable [160]. After alignment to the reference peaks, the errors remain well within the mass tolerance limit of ± 300 ppm, which is recommended by the manufacturer of the MS instrument (Bruker Daltonics) for biotyping purposes.

4.1.4 Feature selection

Processing of the mass spectra of *E. coli* resulted in the identification of 175 peaks. However, not all peaks are features with discriminatory information for a classification model. The redundant peaks in the mass spectra need to be removed from the data set, as they can cause overcomplicating and overfitting (poor generalization) of classification models, and complicate model interpretation. Three feature selection approaches have been investigated in depth to select the appropriate peaks, namely feature selection using random forest (RF) and sequential forward (SFS) and backward selection (SBS). These were selected in order to include a wrapper method (sequential feature selection) and an embedded method (RF). All these feature selection approaches have shown their worth in the field [143, 173], and are commonly applied in the context of MALDI-TOF MS data analysis for identification purposes [145, 174]. For feature selection, the data was analyzed for two different scenarios. Firstly, the features were evaluated based on how well the algorithms performed when distinguishing mass spectra obtained with treated and untreated *E. coli* cells. This is referred to as the binary classification problem. For these cases, the antibiotic mechanism of action (MoA) and relative concentration of the MIC were not considered, and all merged into one class of 'treated' mass spectra. Secondly, the algorithms were evaluated based on how well they could distinguish between the different MoA of the used antibiotics, regardless of their sub-MIC treatment. This is referred to as the MoA classification problem.

The embedded method used to grow the RF employs aggregated bootstrapping of the trees, but this inherently results in oversampling classes with large prior probabilities [175]. As bootstrapping extracts data from the training set uniformly, any imbalance (non-uniformity) present in the training data set will consequently be present in the bootstrapped sample population. Therefore, the resulting classification trees in the forest will be biased towards the overrepresented class(es), due to the higher prior probability of those class(es). This bias influences the relative feature importance, and thus feature selection, as feature importance is based on the error of prediction of samples not included in the bootstrapped aggregated data set (the out-of-bag error, OOB) [176]. Thus, one has to evaluate and consider the data set balance when using the RF feature selection approach. For a binary

classification of the employed *E. coli* data set consisting of 920 mass spectra, 162 (17.6%) spectra were obtained with untreated cells while the majority (82.4%) of the data belongs to spectra from cells treated with antibiotics. A class imbalance is also seen for the MoA classification forest, as out of the five classes (CWL, NUC, PRT, OTH, and untreated) only 8.9% (82 spectra) of the data observations are obtained with antibiotics from the class OTH (other antibiotic MoAs), while the protein synthesis inhibiting (PRT) antibiotics make up one-third of the data (36%, 328 spectra). The classes untreated (UNT), CWL, and NUC are relatively balanced, comprising 17.6%, 23.0%, and 14.8% of the data, respectively.

The stratified cross-fold validation sequential feature selection approach does not suffer from selection biases as a result of class imbalance [177]. However, sequential feature selection is a computationally intensive step, resulting in a computational time of approximately 2 hours for the binary problem and 6 hours for the MoA problem for the *E. coli* data set. To reduce computational time, the number of features was preliminary reduced by excluding features with insignificant relative feature importance, which was determined by means of the RF algorithm. As a threshold, features with a relative feature importance lower than the mean feature importance of all peaks were excluded for sequential feature selection. It is assumed that the selection bias does not influence peaks with such relatively low feature importance.

Feature selection was first evaluated employing the RF approach. Depending on the class labels, binary or MoA, a forest of defined size was grown (200 and 250 trees for the binary and MoA problem, respectively) and the relative feature importance for each peak was determined. Details of the feature selection approach using RFs are provided in Figure 7.
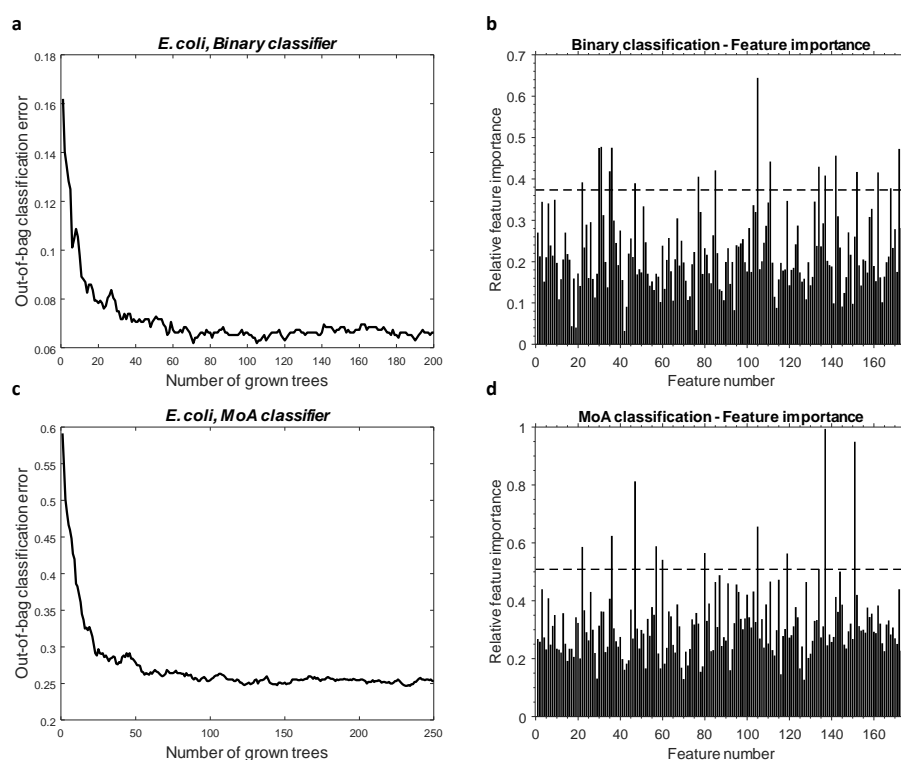
Figure 7. Feature selection details using Random Forest (RF) on *E. coli* data set. Exemplary data showing (a) the elbow plot of the out-of-bag error for 200 decision trees for the binary classifying trees. Depicted in (b) is the relative feature importance of each of the 175 peaks in the mass spectrum of *E. coli* for the binary classification problem using 200 decision trees. Horizontal dotted line shows the feature selection threshold (mean feature importance + 1.5 × feature importance standard deviation). Depicted in (c) is the elbow plot of the out-of-bag error for 250 decision trees for the mechanism of action (MoA) classifying trees. Shown in (d) is the relative feature importance of each of the 175 peaks in the mass spectrum of *E. coli* for the MoA classifying trees using 250 decision trees.

Figure 7a and Figure 7c show the OOB error over the number of grown trees for the binary and MoA model, respectively. As mentioned before, the OOB gives an estimate of the misclassification probability of the RF based on the samples that are not included in the training set. Thus, increasing the number of trees reduces the OOB, resulting in a so-called elbow plot. The elbow plot in Figure 7a shows that growing a RF with 200 trees was sufficient for stabilization of the OOB error for the binary classification problem, and growing additional trees would not benefit the OOB error. As a result of a more complex classification problem for the MoA classification forest (with a total of 5 classes), a larger forest of 250 trees was grown to assure stabilization of the OOB error (see Figure 7c). Thus, feature importance per peak was determined based on 200 and 250 trees for the binary and MoA classification model, of which the results are shown in Figure 7b and Figure 7d, respectively. These results show that peaks have different importance values for each classification problem. This difference leads to different selection thresholds, as the thresholds are data-dependent, and consequently different feature sets are obtained for

each classification problem. This observation is explained by the variability that needs to be described per classification problem, where peaks which contain information on a more antibiotic specific response might be required in the MoA classification problem, compared to peaks that are selected for a more general response to stress for the binary classification problem.

Sequential feature selection results are shown in Figure 8, where details of SBS and SFS on *E. coli* data for the binary classification problem are provided in Figure 8a and Figure 8b. Details of SBS and SFS on *E. coli* data for the MoA classification problem are provided in Figure 8c and Figure 8d.
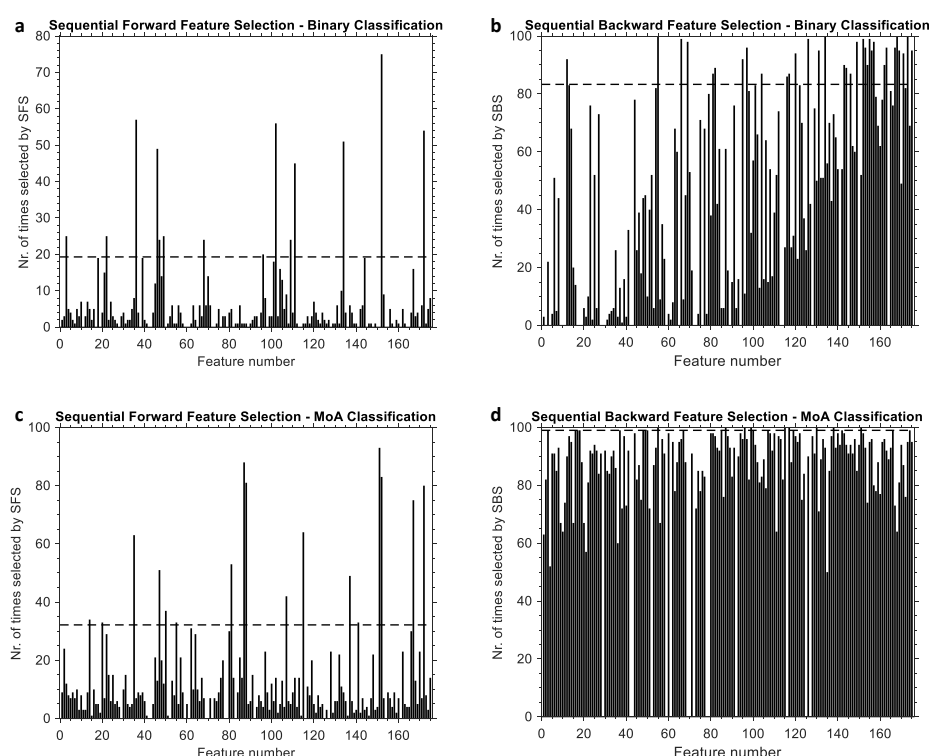

Figure 8. Feature selection details using sequential feature selection. Evaluation results using sequential forward feature selection (SFS) is depicted in (a) and (c), and sequential backward selection (SBS) is depicted in (b) and (d). Feature selection frequency by each algorithm is shown for the binary classification (a) and (b), and the mechanism of action (MoA) classification in (c) and (d). The horizontal line indicates the feature selection threshold (mean times selected + 1.5 × standard deviation times selected). For SBS on the MoA classification problem in (d), the threshold was set to 99, as the data-dependent threshold was > 100.

The selected feature sets vary widely depending on whether SFS or SBS is performed (compare Figure 8a-b, the binary classification model or Figure 8c-d, the Moa classification problem). This is because SFS and SBS have different starting points for feature selection. SFS starts out with an empty feature set, and keeps adding features until the classification

accuracy does not increase anymore. On the contrary, SBS initially considers all features for the classification problem, and eliminates features one by one until the accuracy does not increase anymore. Due to the nature of feature elimination in SBS, one often ends up with subsets of weak features that by themselves do not explain variance in the data very well, but combined they show a synergistic effect on the classification accuracy [178].

Upon comparison of the SFS binary classification (Figure 8a) and SFS MoA classification (Figure 8c), it was observed that for the binary classification problem that the SFS algorithm selects peak number 151 (m/z 9721.5) in 0% of the cases and peak number 152 (m/z 9906.7) in 75% cases. Yet, for the MoA classification problem, peak 151 (m/z 9721.5) is selected in almost all (93%) of the cases, while peak 152 (m/z 9906.7) is selected approximately to the same degree (83%). The influence of the classification problem (binary or MoA) on sequential feature selection is also visible for SBS (see Figure 8b and Figure 8d). For the binary problem only a few peaks are assigned frequently above the selection threshold (83 times selected), whereas for the MoA model, which needs to capture small differences, a multitude of features are selected multiple times. Consequently, the selection threshold of the MoA is higher (> 99) compared to the selection threshold for the binary problem (> 83 times selected).

These observed differences in selected peaks highlights the importance of selecting features while considering the classification problem, as different data patterns determine the desired distinction between classes. It also shows that the data-dependent feature selection approach can direct specific attention to certain peaks, which may otherwise be ignored, as the overall outcome of selected peaks can vary so widely between the algorithm and class labeling used.

To combine the strengths of the three selection algorithms, a fourth feature set was created as well. Here, features which were consistently selected by two or all three of these methods (RF, SFS, SBS) were combined into the so-called aggregated feature set. In total four different feature sets were evaluated for modeling and validation: (1) the feature set as determined by the RF, (2) the feature set selected by SFS, (3) the feature set selected by SBS, and (4) the feature set selected with the aggregated approach.

4.1.5   Model selection

After feature selection, the applicability to distinguish mass spectra obtained from untreated cells and cells treated with antibiotics (binary and MoA specific) was evaluated for each of the four different feature selection approaches. As classification model performance is not only influenced by the selected features that represent data variation, but also by the classifier type, the suitability of various classifiers for the *E. coli* data set was evaluated. Nine classifier types were investigated: linear discriminant analysis and quadratic discriminant

analysis classifiers, but also more complex and modern classifiers, such as Naïve Bayes, several support vector machines (SVM) with different kernel functions (linear, quadratic, cubic and medium Gaussian kernels were invesigated), k-nearest neighbor (KNN), and a decision tree classifier. Support vector machines are of particular interest, as it has been shown that this classifier type works exceptionally well on MALDI-TOF MS data for bacterial identification purposes [145, 147].

For the binary and MoA classification problems, the nine models were trained using *E. coli* data for each of the four feature sets (RF, SFS, SBS, and the aggregated feature set), which resulted in training and evaluating 72 models in total. All obtained classification models were internally validated using stratified 10-fold cross-validation and externally validated with a blind data set of 20 drugs. Internal validation estimates the classification performance of a model, and external validation confirms whether the models generalize well towards unknown data. Evaluation results of all 72 models are combined in Figure 9.

a Internal validation, binary

Feature selection	RF	SFS	SBS	Aggregate	Mean accuracy
No. of features	17	14	33	9	
Linear discriminant	0.92	0.94	0.96	0.91	
Quadratic discriminant	0.93	0.92	0.95	0.91	
Naive Bayes	0.89	0.88	0.76	0.87	
Linear SVM	0.94	0.95	0.97	0.92	
Quadratic SVM	0.95	0.94	0.96	0.93	
Cubic SVM	0.95	0.94	0.96	0.93	
Medium Gaussian SVM	0.95	0.95	0.95	0.94	
Cosine KNN	0.94	0.94	0.94	0.93	
Decision tree	0.95	0.94	0.93	0.93	

b External validation, binary

Feature selection	RF	SFS	SBS	Aggregate	Mean accuracy
No. of features	17	14	33	9	
Linear discriminant	0.85	0.85	0.80	0.85	
Quadratic discriminant	0.95	0.90	0.95	0.95	
Naive Bayes	0.80	0.85	0.70	0.85	
Linear SVM	0.95	0.95	0.80	0.90	
Quadratic SVM	0.90	0.90	0.90	0.95	
Cubic SVM	0.95	0.90	0.85	0.95	
Medium Gaussian SVM	0.95	0.95	0.80	0.95	
Cosine KNN	0.90	0.95	0.75	0.90	
Decision tree	0.85	0.85	0.80	0.90	

c Internal validation, mechanism of action

Feature selection	RF	SFS	SBS	Aggregate	Mean accuracy
No. of features	11	17	9	6	
Linear discriminant	0.64	0.73	0.63	0.63	
Quadratic discriminant	0.71	0.69	0.65	0.62	
Naive Bayes	0.59	0.57	0.50	0.56	
Linear SVM	0.69	0.75	0.64	0.65	
Quadratic SVM	0.77	0.77	0.70	0.66	
Cubic SVM	0.76	0.79	0.68	0.67	
Medium Gaussian SVM	0.77	0.74	0.69	0.69	
Cosine KNN	0.75	0.72	0.63	0.66	
Decision tree	0.74	0.73	0.67	0.66	

d External validation, mechanism of action

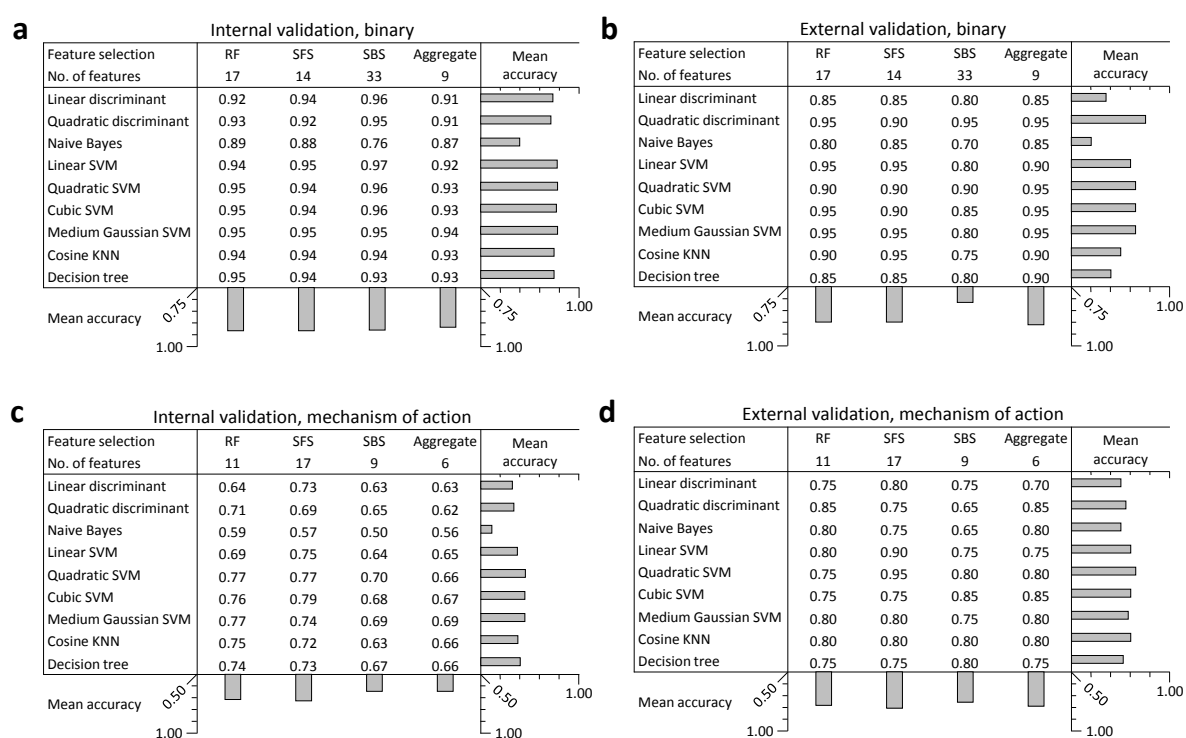| Feature selection	RF	SFS	SBS	Aggregate	Mean accuracy
No. of features	11	17	9	6	
Linear discriminant	0.75	0.80	0.75	0.70	
Quadratic discriminant	0.85	0.75	0.65	0.85	
Naive Bayes	0.80	0.75	0.65	0.80	
Linear SVM	0.80	0.90	0.75	0.75	
Quadratic SVM	0.75	0.95	0.80	0.80	
Cubic SVM	0.75	0.75	0.85	0.85	
Medium Gaussian SVM	0.80	0.80	0.75	0.80	
Cosine KNN	0.80	0.80	0.80	0.80	
Decision tree	0.75	0.75	0.80	0.75	

Figure 9. Overall classification accuracies of 72 classification models on *E. coli* data. Shown are internal (a, c) and external (b, d) validation accuracy of binary (a, b) and mechanism of action (c, d) classification models using four different feature subsets of *E. coli* data set. Feature sets were selected by Random Forest (RF), sequential forward and backward selection (SFS and SBS, respectively) and an aggregated feature set (Aggregate). Listed are the model accuracies and the bars show the mean accuracy of the model across all feature sets (indicated on the right of each panel in bar graph) and the mean accuracy across all models per feature set (indicated in bar graph at the bottom of each panel). SVM: support vector machine; KNN: k-nearest neighbor.

50

Validation of the binary models is shown in Figure 9a (internal validation) and Figure 9b (external validation). Validation of the MoA models is shown in Figure 9c (internal validation) and Figure 9d (external validation). All accuracies are listed in the table of each panel and the mean accuracy per model type and feature subset is shown as a bar graph inset. Evaluation results of the 36 binary and the 36 MoA models will be discussed separately in the following subsections.

4.1.5.1 Binary classification models

Internal validation of binary classifiers showed a relatively good performance for all classifier types (see Figure 9a). This is reflected by a mean accuracy above 0.93 for all classifier types in combination with each feature set, with the exception of the Naïve Bayes classifier (accuracy ranging 0.76-0.89, depending on feature set). Comparing the average internal validation accuracies for each feature set shows there are no major differences between the feature sets, as each feature set has a mean validation accuracy of 0.92-0.93.

Subsequent external validation of the binary models (see Figure 9b) shows a starker contrast between the different model types and feature sets. Similar to the internal validation, external accuracies of the Naïve Bayes classifiers are relatively low (average accuracy for all feature sets 0.80). In contrast to the internal validation, the linear discriminant model has relatively poor performance, with an accuracy of only 0.84. The KNN- and decision tree-based classifiers also perform relatively poor, having an average accuracy of 0.88 and 0.85 respectively. All SVM-based classifiers perform among the best, having an average classification accuracy of 0.90-0.91. The quadratic discriminant models showed the best performance with an average accuracy of 0.94.

When comparing the different feature sets, the aggregated feature subset showed the best performance during external validation, reflected by highest number of classifiers with an accuracy of 0.95 (quadratic discriminant, linear SVM, quadratic SVM, and cubic SVM), and an overall mean accuracy of 0.91. Notably, the SBS feature set (composed of 33 peaks) performs overall worst, with an accuracy of 0.82 on average. The feature sets selected by RF (composed of 17 peaks), SFS (composed of 14 peaks), and the aggregated feature set (composed of only 9 peaks) show higher, and more comparable model accuracies, with average accuracies of 0.90, 0.90, and 0.91, respectively. This can be explained by the fact that the SBS feature set is the largest feature set (33 peaks). Presumably, the selection of multiple irrelevant peaks introduced noise and caused overfitting of the models, resulting in a poor generalization to the unseen (blind) data. The SBS feature set produced the seemingly best performing model when only internal validation was considered, but external validation showed that models trained with the SBS feature set have the worst

performance overall. This highlights the importance of both internal and external validation of the classification models. In addition, it also underlines that one should aim to reduce the number of features for modeling as much as possible. By including relatively few features, model overfitting is avoided, and also makes the model more transparent and thereby easier to interpret [179].

Based on the internal and external validation of the 32 binary classification models to distinguish mass spectra of treated and untreated *E. coli* cells, it is observed that SVM-based as well as quadratic discriminant classifiers result in the best performance. Considering the predictive power and relative sizes of the feature sets, the aggregated feature set was found the preferred feature set to use for binary classification modeling.

4.1.5.2 Mechanism of action classification models

Compared to the internal validation of binary classifiers (overall mean accuracy 0.76 – 0.97), classifiers trained with MoA class labels generally show a lower accuracy (overall mean accuracy 0.50 – 0.79, see Figure 9c). This is a result of the variation in the data that has to be captured by the mass spectral peaks upon increasing the number of classes. As seen for the binary classifiers, the Naïve Bayes classifiers performed relatively poor compared to the other MoA classifiers for each feature set, reflected by a mean accuracy of 0.56. The low accuracy of Naïve Bayes classifiers seen for both classification problems, regardless of feature set, is presumably due to the fact that Naïve Bayes assumes each feature as an independent variable which has no interaction with any of the other features [180]. The validation results indicate that this is not the case for this data set. This can be explained by the origin of the mass spectral peaks, which are all part of a complex protein expression network originating from one cell. Therefore, all features are inherently depending on each other to some degree. In addition, performance of Naïve Bayes is sensitive to imbalanced data [181], contributing to its relatively poor performance.

Contrary to the binary models, the linear and quadratic discriminant MoA classifier do not perform among the best models (only 0.66 and 0.67 overall accuracy). This is possibly due to the higher complexity required for the classifier with more classes, which are better handled by the more advanced SVM models. This statement is supported by the highest model accuracies (0.72-0.73) for all feature sets for the quadratic, cubic, and medium Gaussian kernel SVM classification models.

Where the internally validated binary models all had a roughly equal mean accuracy for the four feature sets (0.92-0.93, see Figure 9a), internal validation of the MoA classifiers shows a larger difference between different feature sets (see Figure 9c). Models using features selected by the RF and SFS show a better classification performance (mean model accuracy of 0.71 and 0.72, respectively) than models using peaks selected by SBS and the aggregated

feature set (both having a mean accuracy of 0.64). This may be a result of the relatively larger sized feature sets selected by the RF and SFS (11 and 17 peaks, respectively) compared to the somewhat smaller feature sets selected by SBS and the aggregated feature set (9 and 6 peaks, respectively), where the latter fail to capture all relevant variation in the data. It appears that in the case of the MoA models, internal validation accuracy benefits from a relatively larger feature set. This effect disappears in external validation results, where it was also found that the RF and SFS feature sets only have a slightly higher accuracy (0.78 and 0.81, respectively) than the SBS and aggregated feature set (0.76 and 0.79, respectively). The relatively poor performance of SBS was also observed during external validation of the binary classifiers, indicating that SBS is not the preferred method for feature selection for the evaluated data set.

Differences in external validation performance between the model types were less distinct for the MoA models compared to the binary models. External validation of MoA-based classifiers showed good generalization of most models, with a mean accuracy of 0.78 considering all trained MoA classifiers (see Figure 9d). The model accuracy of 0.78 is even higher than what was observed for the internal validation (overall average accuracy 0.68). Similar to binary models and the internal validation of MoA models, the poorest performance during external validation of the MoA classifiers was found for the Naïve Bayes classifier, reflected by a mean accuracy of 0.75. The linear and quadratic discriminant analysis (0.75 and 0.78, respectively) and the decision tree (overall accuracy 0.76) had roughly equal performance. Similar to the external validation of the binary models, the SVM-based models performed best using either of the four feature sets (overall mean accuracy 0.79-0.83). The quadratic SVM (Q-SVM) performs best on average in the external validation of MoA classifiers, regardless of feature set (mean accuracy of 0.83).

As the external validation performance of MoA classifiers trained with RF (accuracy 0.78), SFS (accuracy 0.81), and aggregated feature (accuracy 0.79) sets are comparable, the preferred feature set for MoA classifiers would be the aggregated feature set due to having the smallest size of the three. This feature set consists of only 6 peaks, which is relatively small compared to the RF and SFS (11 and 17 peaks, respectively). Although the models trained with RF and SFS performed slightly better than the models trained with aggregated feature set, maintaining a low the number of features low is an acceptable trade-off for a marginally lower accuracy. By reducing the numbers of features, the model becomes more transparent, easier to interpret, and the chances of overfitting are minimized.

It was found for both the binary and the MoA classification problem that the aggregated feature set in combination with the Q-SVM models give on average the best classification performance on the external validation set. Based on these results, this combination of feature selection algorithm and classifier type was selected and applied to distinguish mass spectra based on proteomic response as a result of sub-MIC antibiotic treatment.

4.1.6 Model evaluation

In this subsection, the selected peaks in the aggregated feature sets of both the binary and the MoA models are evaluated in more detail. In addition, the internal and external validation results of the binary and MoA model are discussed to generate a more in-depth understanding of the models' performance.

4.1.6.1 Aggregated feature set of the binary model: peak identification

Details of peaks in the aggregated feature set selected for the binary model are listed in Table 5. Mass spectral details of peaks indicated with asterisk (*) in Table 5 are provided in Figure 10 to illustrate peak differences that are detected during feature selection. These peaks and their relative intensity will be discussed in the following sections, were the relative intensity value will be mentioned in percentage, ± the mean absolute deviation (MAD) in percent point.

Table 5. Aggregated feature set of peaks selected from *E. coli* spectra for the binary model. Listed are the observed m/z value and the theoretical m/z value of the protein, if identified. For identified proteins is indicated the relative mass error in ppm, UniProt accession number, theoretical isoelectric point (pI), and the corresponding name and notes of the protein, and post-translational modifications (PTMs) if applicable. Details of peaks marked with asterisk (*) are depicted in Figure 10.

Observed m/z	Theoretical m/z	Δ Error (ppm)	UniProtKB	pI	Name; notes; PTMs
4531.7	-	-	-	-	-
4859.5	4859.8	71	P64567	9.2	Uncharacterized protein YqgB; response to acidic pH
5097.9	5096.8	203	P68191	11.0	Stationary-phase-induced ribosome-associated protein
7661.0*	-	-	-	-	-
8898.2*	8898.3	1	P0A7T7	10.6	30S ribosomal protein S18, stabilizes the platform of the 30S subunit; N-terminal acetylated;, initiator methionine removed
9906.7	-	-	-	-	-
10650.7	10652.2	135	P0A6Y1	9.3	Integration host factor subunit beta; involved in transcriptional and translational control
11405.4	-	-	-	-	-
12654.0	12654.4	28	P0AD49	6.2	Ribosome-associated inhibitor A; general stress response element; initiator methionine removed

Table 5 shows that 5 out of 9 peaks in the aggregated feature set of the binary model have been tentatively identified. Notably, only for 30S ribosomal protein S18, observed at m/z 8898.2, no specific regulatory or stress related role was previously reported in the UniProt database. The 30S ribosomal protein S18 is a protein reported to be involved in stabilizing the 30S ribosomal subunit [182]. The other four identified proteins selected for the binary model all have a regulatory or stress-associated function annotation in the UniProt database. One of these peaks, observed at m/z 4859.5, is uncharacterized protein YqgB, which is a protein that is known to respond to acidic pH [183]. The peak at m/z 5097.5 was tentatively identified as stationary-phase-induced ribosome-associated protein. Previously, Arnold and coworkers had found this specific peak to be altered in abundance dependent

on the growth stage of bacterial cultures [160] using MALDI-TOF MS. It is known that this protein associates with the 30S subunit of the ribosome and that its copy-number increases from 0.1 per ribosome particle in the exponential growth phase to 0.4 per ribosome particle once the culture reaches its stationary growth phase [184]. The peak at m/z 10650.7 was identified as integration host factor subunit beta, which is known to be involved in transcriptional and translational control [185]. Interestingly, the stationary-phase-induced ribosome-associated protein is long known to be under control by global regulators like integration host factor (composed of the alpha and beta subunit) [184]. Although the beta subunit was observed and selected for the binary model, the alpha subunit (expected at m/z 11223.7) was not observed. Lastly, the selected peak at m/z 12654.0 was identified as ribosome-associated inhibitor A. This protein is known to be elevated during environmental stresses, such as cold shock and cell dense conditions in the stationary phase, where it regulates translation [186]. To further illustrate as to why the peaks listed in Table 5 were selected by the feature selection methods, exemplary details of the unidentified peak at m/z 7661.0 and the peak at m/z 8891.2 (RS18) are depicted in Figure 10.
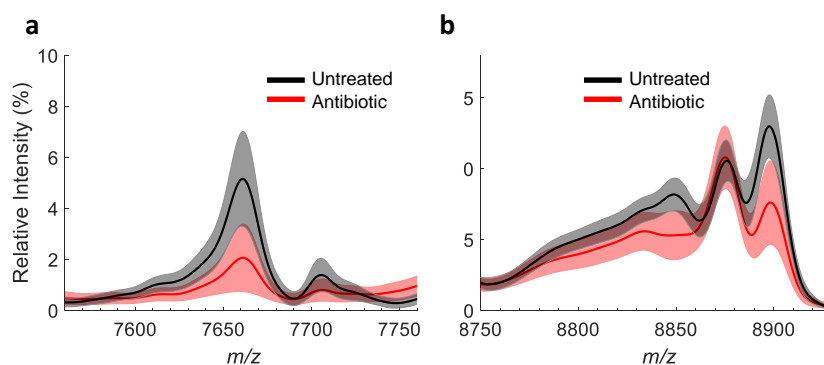
Figure 10. Details from *E. coli* mass spectra. (a) Detail of the unidentified peak at m/z 7661.0. Average mass spectra of untreated cells (black) and treated cells (red), ± mean absolute deviation (MAD) indicated with shades. (b) Details of the peak at m/z 8898.2, identified as 30S ribosomal protein S18. Colors are described in (a).

Figure 10a depicts two adjacent peaks, m/z 7661.0 (peak 111 in Figure 7 and Figure 8) and m/z 7705.4 (peak 112 in Figure 7 and Figure 8), of which the first peak is part of the aggregated feature set for the binary problem. The peak details in Figure 10a allow for an insight in why the peak at m/z 7661.0 has been selected by the feature selection algorithms, and the peak at m/z 7705.4 was not. The relative intensity at m/z 7661.0 is strongly reduced upon treatment with antibiotics (red; average 2.1% ± 1.3) compared to spectra from untreated cells (black; average 5.2% ± 1.9). Contrarily, the peak at m/z 7705.4, does not allow for a reliable distinction between the two classes (treated average 0.8 ± 0.4; untreated 1.4% ± 0.7). Another example is given in Figure 10b. The peak shown at m/z 8898.2 was selected by all three feature selection algorithms, as the relative intensity for spectra obtained from untreated cells is 13.0% ± 2.2 and goes down to 7.6% ± 2.9 for spectra from

cells which were treated with antibiotics. In the same Figure 10b, the peak on the left at m/z 8875.2 was selected neither by the RF nor the sequential feature selection methods. This peak is evidently incapable of making a distinction between the two classes, as its average relative intensity is 10.5% ± 1.5 for spectra obtained from untreated cells and an almost identical intensity of 10.8% ± 2.2 for spectra obtained from cells treated with antibiotics.

4.1.6.2 Aggregated feature set of the MoA model: peak identification

For the MoA model, six peaks were included in the aggregated feature set of which three were tentatively identified. Details of the peaks are provided in Table 6.

Table 6. Aggregated feature set of peaks selected from *E. coli* spectra for the mechanism of action (MoA) model. Listed is the observed m/z value and the theoretical m/z value of the protein, if identified. For identified proteins is indicated the relative mass error in ppm, UniProt accession number, theoretical isoelectric point (pI), and the corresponding name and notes of the protein, next to post-translational modifications (PTMs) if applicable. Details of peaks marked with asterisk (*) are depicted in Figure 11.

Observed m/z	Theoretical m/z	Δ Error (ppm)	UniProtKB	pI	Name; notes; PTMs
5097.9*	5096.8	203	P68191	11.0	Stationary-phase-induced ribosome-associated protein
5340.5	5339.1	-251	C1P5Z7	7.6	Putative inhibitor of glucose uptake transporter SgrT; involved in recovery from glucose-phosphate stress
6504.2	-	-	-	-	-
7929.2	-	-	-	-	-
9065.5*	9066.2	75	P0AET2	4.9	Acid stress chaperone HdeB; matured, maturated, position 30-108
9721.5	-	-	-	-	-

Regulatory and stress-associated proteins were also identified in the MoA feature set. Similar to the binary feature set, the peak at m/z 5097.7 (stationary-phase-induced ribosome-associated protein) was selected for the MoA classification model. Two other proteins involved in stress-response mechanisms were identified as well. The peak at m/z 5340.5 was identified as putative inhibitor of glucose uptake transporter SgrT. This protein is known to be involved in the recovery process from glucose-phosphate stress by disruption of the glycolytic pathway [187]. The peak observed at m/z 9065.5 was identified as acid stress chaperone HdeB. This protein is known to prevent the aggregation of periplasmic proteins at acidic pH values using chaperone-like activity [188]. The other three peaks in the aggregated feature set, observed at m/z 6504.2, m/z 7929.2, and m/z 9721.5, were not identified. Exemplary details of the identified peaks at m/z 5097.9 (stationary-phase-induced ribosome-associated protein) and m/z 9065.5 (acid stress chaperone HdeB) are provided in Figure 11a and Figure 11b, respectively.
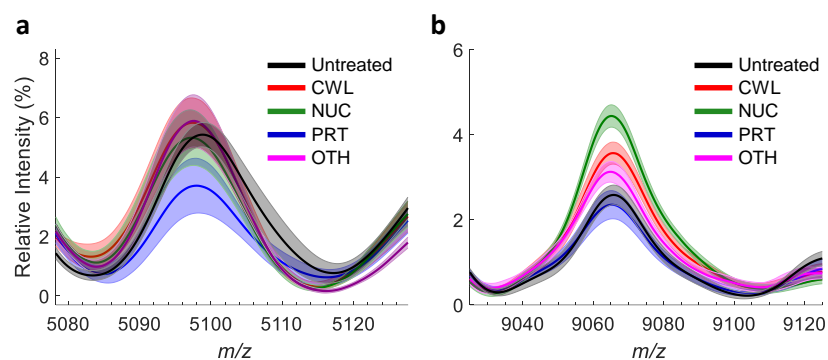
Figure 11. Details from averaged *E. coli* mass spectra ± ½ mean absolute deviation (MAD; shades). (a) Detail of the peak at m/z 5097.9, identified as stationary-phase-induced ribosome-associated protein. Colors are as follows: average mass spectra from untreated cells (black); cells treated with cell wall synthesis inhibitors (CWL, red), the class nucleic acid synthesis and processing inhibitors (NUC, green), protein synthesis inhibitors (PRT, blue) and cells treated antibiotics with another mechanism of action (OTH, pink). Exemplary mass spectra shown in (a) and (b) were treated at ⅛×MIC of antibiotics (b) Details of the peak at m/z 9065.5, identified as acid stress chaperone HdeB. Colors are as described for (a).

The relative intensity of the peak at m/z 5097.9, in relation to untreated cells (black; 5.4% ± 0.8), increases marginally up to 5.9% ± 1.7 upon treatment with antibiotics of the class OTH, as well as for the class CWL (5.8% ± 1.6). For cells treated with class NUC, the relative intensity is slightly lower at 5.3% ± 1.8, but especially the antibiotics of the class PRT show a strong decrease to 3.7% ± 1.8. Considering that the proteins' abundance is known to increase in upon growth progression into the exponential growth phase [160, 184], it seems counterintuitive that there is an increase observed upon treatment with antibiotics of any class (as is observed here for the classes CWL and OTH). Treatment with antibiotics would cause the cell culture not to progress into the exponential growth phase, and therefore the observed decrease in peak intensity upon treatment with antibiotics (especially visible for the class PRT) is in line with those previous reports. As this peak was also selected for the binary classification problem, it seems that the proteins' response to growth stage is more complex than solely up- and downregulation upon treatment with the antibiotics.

Details of the peak corresponding to the acid stress chaperone HdeB (m/z 9065.5) are shown in Figure 11b. Its relative intensity increases from 2.6% ± 0.2 for untreated cells, upon treatment with antibiotics of all classes (CWL: 3.6% ± 0.3; NUC: 4.4% ± 0.3; OTH: 3.1% ±0.2) except protein synthesis inhibitors (PRT: 2.4% ±0.3). This illustrates the responsiveness of this peak to the antibiotic treatments.

Although none of the proteins in the aggregated feature sets of both binary and MoA models are annotated in the UniProtKB database or known from literature as being involved in specifically antibiotic responses, their reported involvement in different regulatory

processes and general stress response mechanisms, indicate that the feature selection algorithms are able to extract relevant peaks from the mass spectra for modeling.

4.1.6.3 Internal validation of the binary model

In the following subsections, more detailed results of the internal and external validation of the binary and MoA models trained with the previously discussed peaks are shown. These results allow for a more in-depth discussion of the performance of the Q-SVM modeling approach. Details of the models performance will be provided in the form of confusion matrices. This is a table where each column represents the instances of the prediction by the model and each row represents the true class.

Details of the classification results for internal validation of the binary Q-SVM model are provided in Table 7. The binary Q-SVM model was trained with 920 mass spectra, of which 162 originated from cells that were not treated with any antibiotics (the class untreated). The other 726 mass spectra originated from cells treated with 17 antibiotics (see Table 2), at (sub-)lethal concentrations ranging from $^1/_{32}\times$ to 1×MIC.

Table 7. Confusion matrix of the 10-fold cross-validation of binary quadratic support vector machine model with the aggregated feature set of *E. coli*, encompassing 920 mass spectra (all antibiotics at all concentrations). Indicated is the total number of spectra per class (either spectra from cells that are 'treated' or 'untreated') and the corresponding recall and precision value per class, and the overall accuracy in the bottom right in bold.

	Model classification			
Class labels	Treated	Untreated	Total	Recall
Treated	726	32	758	0.96
Untreated	39	123	162	0.76
Total	765	155	920	
Precision	0.95	0.79		**0.92**

The confusion matrix of the binary model shows an overall accuracy of 0.92, classifying 726 out of the 920 mass spectra to the correct class (green, on the diagonal). However, both the recall (true positive rate) and precision (positive predictive value, indicating the fraction of true positive) values for both classes deviate significantly from the overall accuracy. The overall precision for the class treated with antibiotics is 0.95, relatively close to the overall accuracy of 0.92. However, the precision for the class untreated is only 0.79. The same holds true for the recall values of both classes, which is high for the class of treated spectra (0.96), but is lower (0.76) for the untreated class. This is due to the relatively large class imbalance, as only 18% of the data (162 spectra) originate from untreated cells, while the vast majority of the spectra (758 spectra, 82% of the data) originate from antibiotic treated cells.

58

Therefore, although the number of spectra misclassified is comparable (32 and 39 spectra, indicated in Table 7 in red), their impact on the recall and precision value for the class untreated is relatively large. In future experiments it would be advised to reduce the class imbalance that is currently present, to avoid such effects. Nevertheless, considering that the class treated consists of 758 mass spectra, all dosed at relatively low, sub-lethal concentrations (between $^1/_{32}×$ and 1×MIC) the model is very capable at distinguishing those from untreated cells' spectra, as only 39 of the treated cells' spectra were misclassified to the class untreated. This indicates that the combination of the aggregated feature selection algorithm and Q-SVM classifier type is able of identifying antibiotic effects at sub-MIC concentrations in mass spectra obtained from *E. coli* cell cultures.

4.1.6.4 External validation of the binary model

After internal validation of the binary Q-SVM model, the binary model was also validated with an external data set. This entailed screening 20 blind drugs with the developed assay at a single fixed concentration of 10 µM, among which antibiotic drugs and drugs with no antibiotic activity. This concentration was selected, as it represents a typical high-throughput screening dose [189]. After recording the mass spectra from the corresponding cell cultures exposed to this set of drugs, mass spectra were imported and processed as shown for the training data. Mass spectral details of the selected features in the aggregated feature set were extracted from this external data set and fed into the previously trained binary Q-SVM model. The binary model then returned whether the mass spectrum belonged to a *E. coli* cell culture treated with an active antibiotic ('treated'), or an inactive drug ('untreated'). Details of the external validation are listed in Table 8.

Table 8. Classification details of the binary quadratic support vector machine classification model using the aggregated feature set (9 peaks) for *E. coli* for external validation on the blind data set. Drugs, listed in the first column, were screened at fixed concentration of 10 µM. The second column (True class) indicates the actual class of the drug, therefore the expected result of the classifier. The third column, labeled Literature MIC (µM), lists the literature minimal inhibitory concentrations of the antibiotic in question as reference. Model classification details are given in the fourth column, incorrect classifications are stated in brackets. Overall performance of the model was evaluated using the overall accuracy, indicated at the bottom in bold.

Drug	True class	Literature MIC (µM)	Model classification
Brucine	Untreated	-	Untreated
Ephedrine	Untreated	-	Untreated
Ergotamine	Untreated	-	Untreated
Fenbendazole	Untreated	-	Untreated
Loperamide	Untreated	-	Untreated
Metoprolol	Untreated	-	Untreated
Paroxetine	Untreated	-	Untreated
Sumatriptan	Untreated	-	Untreated
Thalidomide	Untreated	-	Untreated
Umifenovir	Untreated	-	Untreated
Ampicillin	Treated	23 [157]	Treated
Azithromycin	Treated	11 [157]	Treated
Cefuroxime	Treated	19 (this thesis)	Treated
Chlortetracycline	Treated	17 [190]	Treated
Fusidic acid[a]	Untreated	-	Untreated
Nalidixic acid	Treated	34 [157]	Treated
Novobiocin	Treated	104 [191]	Treated
Paromomycin	Treated	6 [192]	Treated
Tiamulin	Treated	16 [193]	(Untreated)
Trimethoprim	Treated	7 [157], (this thesis)	Treated
		Overall accuracy	**0.95**

a) Inactive on Gram-negative bacteria, such as *E. coli*.

The external validation of the binary model shows an overall accuracy of 0.95, with 19 out of 20 correct classifications. This is in agreement with values obtained for internal validation (overall accuracy 0.92), indicating that the binary model trained with the aggregated feature set generalizes well to unseen data.

All drugs in the blind set which have no antibiotic activity were correctly classified as being inactive. This performance is better than during internal validation, where a relatively large fraction (21%) of the untreated samples was misclassified as being treated with an antibiotic. It should also be noted that spectra from *E. coli* cells treated with fusidic acid were correctly identified as 'inactive', as fusidic acid has no activity on Gram-negative bacteria.

The single misclassification occurred for spectra from cells treated with tiamulin. This misclassification of tiamulin was not only confined to the Q-SVM binary model, but was interestingly observed for all other binary classification model types that were assessed for classification modeling with the aggregated feature set (for details see Appendix Table 1). Tiamulin is a diterpene pleuromutilin antibiotic, which inhibits protein synthesis by binding to the peptidyl transferase unit of the large 50S ribosomal subunit [194]. It seems unlikely that the selected features could not capture the effect of this specific inhibitor, as there are ample antibiotics in the training data set that are known to bind to the peptidyl transferase subunit in the training data set (chloramphenicol and the macrolides erythromycin and clarithromycin). Additionally, the Q-SVM model, as well as the other classifier types, correctly classified the other macrolide (azithromycin) in the blind test set. As the model was trained with antibiotics at the sub-lethal concentrations ranging from 1×MIC down to $^1/_{32}$×MIC, it is surprising that none of the binary models could identify tiamulin at the employed screening concentration. At the screening concentration of 10 µM an effect was expected, as it is approximately $^5/_8$×MIC tiamulin (literature MIC: 8 mg/L; 16 µM [193]). Currently, there is no clear explanation for this misclassification, and it is speculated that the consistent misclassification of tiamulin by the Q-SVM, and other models, is due to a lower susceptibility of *E. coli* than was expected based on the literature MIC.

The correct classification of the antibiotics in the blind test set (with the exception of tiamulin) exceeds initial expectations, as the literature MIC values of most of these drugs is significantly higher than the screening concentration of 10 µM. For example, for ampicillin the MIC was reported to be 23 µM, over a factor two higher than the screening concentration. Even more remarkable is the correct classification of nalidixic acid and novobiocin, having a reference MIC of 34 µM and 105 µM, respectively, over a factor 3 and 10 higher than the screening concentration of 10 µM. A slightly lower MIC compared to the screening concentration of 10 µM was present in the blind data set for two antibiotics (trimethoprim, MIC of 7 µM, and paromomycin, MIC 6 of µM), which were nonetheless classified correctly. The results of the binary model show the powerful capabilities of the aggregated feature set in combination with the Q-SVM modeling approach, which is able to detect relatively weak antibiotic activity from the cells' mass spectra at concentrations around and far below their MIC values.

4.1.6.5 Internal validation of the MoA model

The MoA model was trained with the same 920 mass spectra as the binary model, but with the aggregated feature set specifically selected for the MoA classification problem. Now, the 726 mass spectra that originated from cells treated with antibiotics were further divided according to their respective MoA. Results of the internal validation of the Q-SVM model are listed in the corresponding confusion matrix in Table 9.

Table 9. Confusion matrix of the 10-fold cross-validation of mechanism of action (MoA) quadratic support vector machine model with the aggregated feature set of *E. coli*, encompassing 920 mass spectra (all antibiotics at all concentrations). Antibiotics were grouped according to their MoA: cell wall synthesis inhibitors (CWL), protein synthesis inhibitors (PRT), nucleic acid synthesis and repair inhibitors (NUC), inhibitors of other type (OTH), and untreated (UNT). Indicated is the total number of spectra per class, the corresponding recall and precision value per class, and the overall accuracy in the bottom right in bold.

		Model classification						
	Class labels	CWL	NUC	OTH	PRT	UNT	Total	Recall
True class	CWL	130	14	8	32	28	212	0.61
	NUC	27	84	4	17	4	136	0.62
	OTH	18	8	9	37	10	82	0.11
	PRT	25	6	4	261	32	328	0.80
	UNT	22	1	0	10	129	162	0.80
	Total	222	113	25	357	203	920	
	Precision	0.59	0.74	0.36	0.73	0.64		**0.67**

The MoA model classified 613 out of the 920 mass spectra to the correct class (overall accuracy 0.67), which reflects a mediocre performance. Notably, the recall value for the class containing other types of antibiotics (OTH) is exceptionally low, with only 9 out of the 82 spectra being classified correctly. The observed classification difficulty for the class OTH is presumably due to several factors. The first factor contributing to this specific classification error is that the class OTH is relatively small compared to the other classes. This class imbalance causes an underrepresentation during both feature selection and model training. A second factor contributing to the models' poor performance with the class OTH is considering the nature of the included antibiotics. The OHT class consists of only two antibiotics (nitrofurantoin and rifampicin) that do not fit to any of the other specific antibiotic classes (CWL, PRT, or NUC). Nitrofurantoin has a very distinct and unique MoA. Nitrofurantoin is intracellularly converted to reactive intermediates that attack macromolecules within the bacterial cell, among which ribosomal proteins and DNA, and disrupt the respiratory chain and pyruvate metabolism [195]. Rifampicin also has a relatively unique MoA among the employed set of antibiotics. It does not interfere directly with ribosomal subunits, but inhibits bacterial DNA-dependent RNA polymerase, thereby inhibiting RNA synthesis and, consequently, inhibiting protein synthesis. Therefore, rifampicin was not incorporated to the class NUC nor to the class PRT, but to the class OTH. Thus, the class OTH consists of only two widely different antibiotics, which makes it hard to find specific features that are unique for this specific class, but still distinct from the other classes. In short, the classification model struggles with the OTH class due to its intra-class variability and low number of training samples, and assigns the majority of its spectra to the protein synthesis inhibiting class (PRT, 37 spectra) and cell wall synthesis inhibitors (CWL, 18 spectra).

Contrary to the class OTH, the protein synthesis inhibitors (PRT) shows a high recall value, with 80% of the spectra assigned correctly (261 out of 328 correctly classified). The model seems to handle the class of untreated spectra (UNT) equally well, with a recall value of 0.80. However, the UNT class has a considerably lower precision of only 0.64. This low precision of the class untreated is mainly caused by misclassification of all other classes of antibiotics (CWL, OTH and PRT), except class NUC. Upon closer inspection, it was observed this was mainly due to the misclassification of spectra from cells that were treated with the lowest fractions of the MIC ($^1/_{16}\times$ and $^1/_{32}\times$MIC), which are hardest for the model to accurately distinguish from untreated cells' spectra by the model (data not shown).

The class of CWL synthesis inhibitors, comprising 23% of the spectral data, suffers like the class PRT and UNT from relatively low precision (0.59). This is mainly due to a roughly equal confusion by the model with all the other classes (27 spectra misclassified to NUC, 18 misclassified to OTH, 25 misclassified to PRT, and 22 misclassified to UNT). Overall, the model is able to make the distinction between the other three largest classes (PRT, NUC and UNT), reflected in their relatively high recall (0.62, 0.80, and 0.80, respectively) and precision values (0.74, 0.73, and 0.64, respectively). As stated for the binary model, it is advised to balance the data set more into equally large classes to avoid bias towards one (or several) classes during the feature selection, which subsequently skews model performance. Based on the presented results, the MoA model accuracy could also be improved by substituting the loosely defined class OTH by a more defined class of antibiotics.

4.1.6.6   External validation of the MoA model

Similar to the binary model, the MoA model was externally validated with the same blind data set of drugs, screened at 10 µM. Spectra from *E. coli* cells treated with the blind drugs were processed and the data for the six features in the aggregated feature set was extracted and fed into the MoA model. The model classified the mass spectra and returned the corresponding MoA, (CWL, NUC, PRT, or OTH), or the model would indicate that the mass spectrum came from a *E. coli* cell culture which was treated with an inactive drug and therefore would return the outcome 'untreated' (UNT). Detailed classification results of the MoA Q-SVM model trained with the aggregated feature set are listed in Table 10.

Table 10. Classification details of the mechanism of action (MoA) quadratic support vector machine classification model using the aggregated feature set (6 peaks) for *E. coli* for external validation on the blind data set. Drugs, listed in the first column, were screened at fixed concentration of 10 µM. The second column (True class) indicates the actual class of the drug, therefore the expected result of the classifier. The third column, labeled Literature MIC (µM), lists the literature minimal inhibitory concentrations of the antibiotic in question as reference. Model classification details are given in the fourth column, incorrect classifications are stated in brackets. UNT: untreated; CWL: cell wall synthesis inhibitor; NUC: nucleic acid synthesis inhibitor; PRT: protein synthesis inhibitor; OTH: other MoA. Overall performance of the model was evaluated using the overall accuracy, indicated at the bottom in bold.

Drug	True class	Literature MIC (µM)	Model classification
Brucine	Untreated	-	UNT
Ephedrine	Untreated	-	UNT
Ergotamine	Untreated	-	UNT
Fenbendazole	Untreated	-	UNT
Loperamide	Untreated	-	UNT
Metoprolol	Untreated	-	UNT
Paroxetine	Untreated	-	UNT
Sumatriptan	Untreated	-	UNT
Thalidomide	Untreated	-	UNT
Umifenovir	Untreated	-	UNT
Ampicillin	CWL	23 [157]	CWL
Azithromycin	PRT	11 [157]	PRT
Cefuroxime	CWL	19 [157]	CWL
Chlortetracycline	PRT	17 [190]	PRT
Fusidic acid[a]	Untreated	-	UNT
Nalidixic acid	NUC	34 [157]	(PRT)
Novobiocin	NUC	104 [191]	(PRT)
Paromomycin	PRT	6 [192]	(UNT)
Tiamulin	PRT	16 [193]	PRT
Trimethoprim	NUC	7 [157], (this work)	(PRT)
		Overall accuracy	**0.80**

a) Inactive on Gram-negatives such as *E. coli*.

The external validation of the MoA model shows that the model performs reasonably well, with an overall accuracy of 0.80. This performance is better than expected based on the internal validation (overall accuracy 0.67). This shows that the MoA model generalizes well to unseen data. Notably, all drugs without antibiotic activity (including fusidic acid) are correctly classified as untreated. This performance is also better than was expected based on the internal validation, where the class of untreated had a recall of only 0.80. Most striking is the classification result for spectra from cells treated with tiamulin. Contrary to the binary model, which misclassified tiamulin as an inactive drug, the MoA model is able to classify it correct as belonging to the class of protein synthesis inhibitors (PRT).

64

Overall, the MoA model makes four misclassifications. One of these misclassifications was for the antibiotic paromomycin, misclassified as untreated. Interestingly, the binary model had correctly classified this drug as antibiotic, while here the MoA model does indicate it as an inactive drug. The reference MIC of paromomycin is slightly lower (6 µM) than the screening concentration (10 µM). It is therefore unexpected that the supposedly strong antibiotic effect was not captured by the selected features. However, the misclassification is in line with the relatively low precision of the class UNT seen in the internal validation of the MoA model (0.64).

The other three misclassifications are all from antibiotics of the class NUC: nalidixic acid, novobiocin, both interfering with gyrase proteins, and trimethoprim, which interferes with folate pathway. The misclassification of trimethoprim by the model is unexpected, as it was dosed slightly above its MIC (7 µM) in the screening (10 µM), and it was one of the antibiotics included in the training set of the model. The MoA consistently misclassifies antibiotics of the class NUC with the class of protein synthesis inhibitors (PRT). This is in line with the internal validation of the MoA model, which misclassified 17 spectra from the class NUC incorrectly to the class PRT. Even more of the class NUC (27 spectra) were misclassified to the class CWL during internal validation, but this confusion is not observed in the external validation set.

The bias towards the class of PRT observed during external validation is based on the large class imbalance in the data set, which was also observed for internal validation of the model. However, for most of the other antibiotics in the test set, which were dosed at sub-MIC concentrations (ampicillin, azithromycin, cefuroxime, chlortetracycline, and tiamulin), the model was able to classify them to the correct antibiotic class. As the aim is to devise a screening assay to identify unknown, weakly active drugs with the binary and MoA models, this misclassification between different MoA classes of antibiotics (as for nalidixic acid, novobiocin and trimethoprim) is not as disadvantageous as misclassifying an actual active drug as being untreated using the MoA model (as seen for paromomycin).

Despite the observed incidental misclassifications of the model, both the binary and MoA model can identify the antibiotics and their respective MoA reasonably well. Compared to Raman- [85] and cytological profiling-based assays [83] described in literature, the MALDI-TOF MS-based method described in this thesis outperforms them both. Overall, the Raman-based method described by Athamneh had similar accuracies of 0.45-0.84 for their MoA models, depending on the employed algorithms. However, this was only for bacterial cultures treated with relatively high concentrations of antibiotics, at 3×MIC [85]. The cytological profiling method described by the Pogliano group does not mention specific accuracies of classifiers, as their work relies on unsupervised learning methods, but equally suffers from the drawback of the high concentrations of antibiotics required to see an effect, namely 5×MIC [83]. Contrarily, the MALDI-TOF MS-based method described in this

work is able to detect antibacterial effects at concentrations down to $^1/_{32}$xMIC, making it a superior method to detect weakly active drugs. Moreover, the developed MALDI-TOF MS-based assay is label-free and high-throughput compatible.

4.1.7 Summary

The aim of this thesis was to develop a high-throughput cell-based screening assay which is able to detect sub-lethal effects of antibiotics in bacterial cell cultures using MALDI-TOF mass spectrometry. The assay was developed using *E. coli* cell cultures to illustrate the proof-of-concept. The bacterial cell cultures were exposed to antibiotics with a known activity, and the subsequent proteomic response of the cells was measured with MALDI-TOF mass spectrometry. Based on the presented screening results of *E. coli* cell cultures, the applicability of MALDI-TOF mass spectra to measure sub-lethal effects induced by antibiotic treatment was shown.

By using different feature selection algorithms, relevant peaks in the mass spectra were selected for modeling the proteomic response of the *E. coli* cells to the antibiotics. Feature selection for the binary and the MoA classification problem was performed using a random forest of decision trees, sequential forward and backward feature selection, and the aggregated selection which included mass spectral peaks that were selected by at least two out of these three selection methods. The peak selection criteria for each feature set were data-dependent, to avoid any subjective bias. This resulted in dissimilar feature sets for binary and MoA model training, even though the underlying data is identical.

Nine different model types were evaluated based on their classification performance for both the binary and MoA problem using their respective feature sets. In total, this resulted in the evaluation of 36 binary classification models and 36 MoA classification models. For this, the models were internally validated using 10-fold cross-validation and externally validated using a blind data set. The external dataset was composed of antibiotic and non-antibiotic drugs, screened at a fixed concentration of 10 μM.

Regarding the four feature sets, the aggregated feature set was shown to lead to the best classification performance for both binary and MoA models. As the selection criterion for including features in the aggregated feature set is relatively stringent (peaks must be selected by two out of the three algorithms), the aggregated feature set is inherently smaller than the other feature sets that were evaluated (RF, SFS, SBS). This is advantageous as a smaller feature set reduces the chances of overfitting and increases model transparency and interpretability. In-depth analysis of the aggregated feature set revealed that the majority of the selected peaks correspond to ribosomal associated proteins, most of which have an annotated function indicating their role in general stress responses and

regulatory pathways. This confirms that the employed feature selection algorithms are capable of identifying relevant, stress associated proteins.

Regarding the different model types investigated, it was determined that SVM-based classifiers performed best, showing high classification accuracies for both internal and external validation, for both the binary and MoA models. The binary and the MoA Q-SVM models, trained with their respective aggregated feature set, were further analyzed regarding their classification performance. The binary Q-SVM model showed a good classification performance, represented by an overall accuracy of 0.92 (internal validation) and 0.95 (external validation). The MoA Q-SVM model also showed good performance, having an overall accuracy of 0.67 (internal validation) and 0.80 (external validation), reflecting that the models generalize well towards unseen data.

The results show that training the model with sub-lethal concentrations of known antibiotics allows for detection of weakly active drugs, as the concentration of most antibiotics in the blind drug set were screened below their MIC. However, both models suffered from a class imbalance in the underlying training data, mainly caused by the overrepresentation of spectra from cells treated with antibiotics (binary model) and of the class PRT (MoA model). In addition, the MoA model suffered from an underrepresentation of the poorly defined class OTH, which resulted in a low accuracy for that class in particular. In future experiments it would be advised to prevent class imbalance and define more specific classes. Especially for the MoA model, overrepresentation of the class of protein synthesis inhibitors (PRT) and the underrepresentation of the class nucleic acid processing inhibitors (NUC) resulted in predictive limitations.

The established workflow, summarized in Figure 12, realized a high-throughput cell-based screening assay, able to detect sub-lethal effects of antibiotics in bacterial cell cultures using MALDI-TOF mass spectrometry. By analyzing the proteomic responses provoked by the antibiotics, classification models were generated to determine with which (type of) antibiotic the respective cell culture was treated. These classification models were subsequently used to classify the mass spectra of cells exposed to unknown drugs in a screening setting. Overall, the MALDI-TOF MS based assay, in combination with advanced machine learning approaches, allows for both detecting antibiotic activity, and the distinction between different mechanisms of action of the antibiotics. Having demonstrated the workflow on the *E. coli*, the applicability of the method was subsequently investigated using the Gram-positive bacterium *S. aureus*.
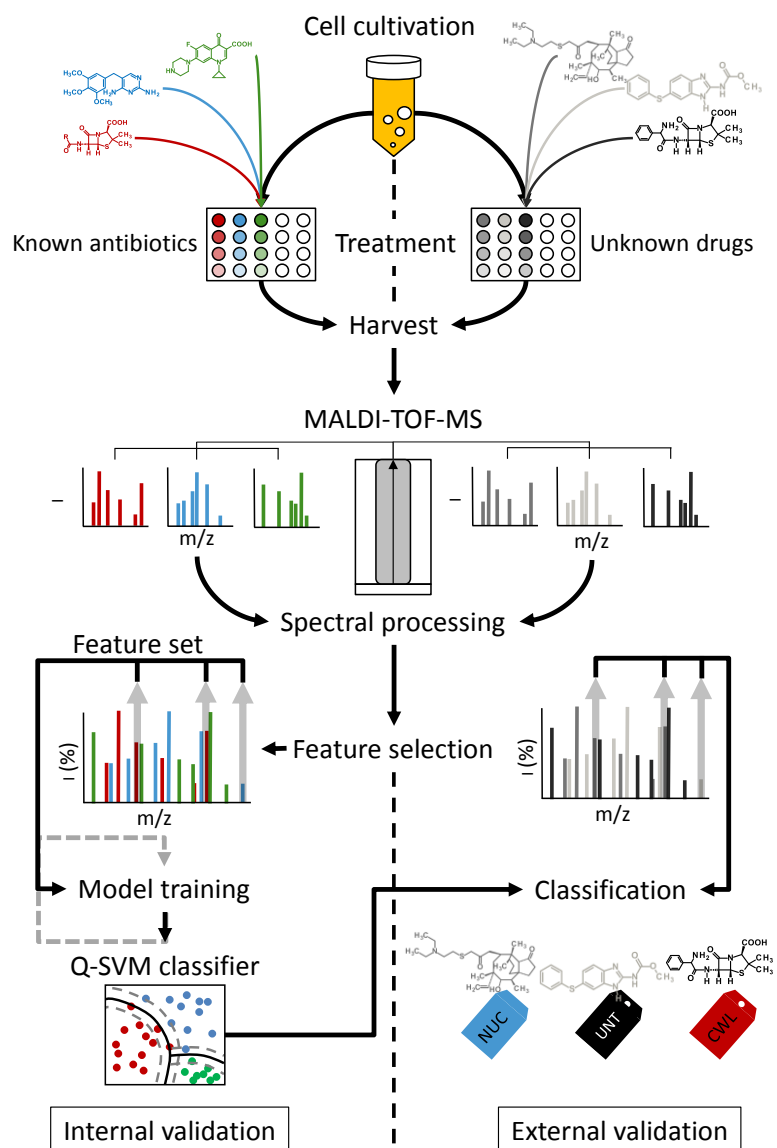
67

Figure 12. Schematic overview of the assay workflow. First, a batch of synchronized cells is cultured and exposed to known antibiotics at concentrations equal or lower than the minimal inhibitor concentration (MIC). From these cells, the MALDI-TOF mass spectra are recorded. Subsequently, feature selection is performed to extract the peak data which best describe the proteomic variation induced by the antibiotics. Using the aggregated feature selection approach, a subset of peaks is used to train a quadratic support vector machine (Q-SVM) classifier model. Then, data from cells treated with a blind screening set of drugs is extracted at the selected features and the data is fed into the model to classify with which (type of) antibiotic the cells were treated, to validate the model. The model then returns the mechanism of action, for example NUC (nucleic acid synthesis and repair inhibitor), CWL (for cell wall synthesis inhibitors) or returns spectra are untreated (UNT).

4.2 Staphylococcus aureus

Drug discovery for Gram-positive bacteria is as important as it is for Gram-negative bacteria, as Gram-positive bacteria are among the most common human clinical infections [196]. As stated in the introduction, an antibiotic screening assay that is adaptable and flexible enough to handle multiple cell types is desirable in the field of drug discovery. Therefore, after the developed assay was thoroughly evaluated using the *E. coli* data set, the assay and data-dependent workflow were applied to *S. aureus*. Firstly, the MIC of the same set of antibiotics used on *E. coli* was determined for *S. aureus* reference strain ATCC 29213. Subsequently, *S. aureus* cells were treated with the set of antibiotics at sub-MIC concentrations (1× down to $^1/_{32}$×MIC) and mass spectra were recorded. Next, feature selection using RF, SFS, and SBS was performed to yield the aggregated feature sets for both the binary and MoA classification problem. With the aggregated feature sets, Q-SVM classification models were constructed. As for *E. coli*, the resulting binary and MoA classification models were internally validated using 10-fold cross-validation, and externally validated with the blind set of 20 drugs.

4.2.1 MIC determination, cell synchronization, and peak alignment

For *S. aureus* (ATCC 29213), the same set of antibiotics as for *E. coli* was employed, and MIC values were determined using the broth microdilution method according to EUCAST guidelines. The MIC values are listed in Table 11.

The obtained MIC values for *S. aureus* were all found to be within the acceptable range (± 2 dilution series for most antibiotics) of EUCAST guidelines reference values. After synchronization of the cells' division cycle, it was found that a McFarland standard of 1.0 corresponded to roughly $1×10^7$ CFU/mL for *S. aureus*. Cells were allowed to adapt to the nutrient rich medium for at least one division cycle of approximately 90 minutes to a McFarland of 2.0 - 2.6 before dilution to McFarland of 1.0 and addition to the 384 well plates of antibiotics, as described in the experimental section.
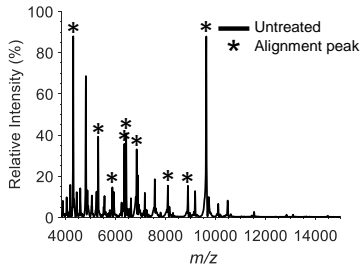
Table 11. Minimal inhibitory concentration (MIC) values of S. aureus experiments. Indicated is the antibiotic chemical class and main target, next to the mechanism of action (MoA) classification abbreviation used for model training (CWL: cell wall synthesis, NUC: nucleic acid synthesis/repair, PRT: protein synthesis, and OTH: other mechanism of action), and the antibiotics' respective MIC values (mg/L) according to reference values by European Committee on Antimicrobial Susceptibility Testing (EUCAST) and as determined in this thesis. NA = not available.

Antibiotic	Chemical class, main target	MoA	MIC (mg/L) (EUCAST)	MIC (mg/L) (this thesis)
Amoxicillin	β-lactam, DD-transpeptidase inhibitor	CWL	NA	2
Benzylpenicillin	β-lactam, DD-transpeptidase inhibitor	CWL	0.125	4
Cefotaxime	β-lactam, DD-transpeptidase inhibitor	CWL	NA	1
Cefuroxime	β-lactam, DD-transpeptidase inhibitor	CWL	NA	1
Chloramphenicol	Amphenicol, binds to the 50s ribosomal subunits, inhibits peptidyl transferase	PRT	8	8
Ciprofloxacin	Fluoroquinolones inhibiting DNA gyrase and topoisomerase IV	NUC	1	0.25
Clarithromycin	Macrolide, binds to the 50s ribosomal subunits, inhibiting peptidyl transfer	PRT	1	0.5
Doxycycline	Tetracycline class, steric hindrance of A-site by binding 30S ribosomal subunit	PRT	1	0.5
Erythromycin	Macrolide, binds to the 50s ribosomal subunits, inhibiting peptidyl transfer	PRT	1	0.25
Gentamicin	Aminoglycoside, binds to the 50s ribosomal subunits, inhibiting peptidyl transfer	PRT	1	4
Moxifloxacin	Fluoroquinolones inhibiting DNA gyrase and topoisomerase IV	NUC	0.5	0.008
Neomycin	Macrolide, binds to the 50s ribosomal subunits, inhibiting peptidyl transfer	PRT	NA	8
Nitrofurantoin	Nitrofuran antibiotic, reactive metabolites damage macromolecules	OTH	64	64
Rifampicin	Rifamycin, Inhibits DNA-dependent RNA polymerase	OTH	0.0625	0.008
Tetracycline	Tetracyclin class, steric hindrance of A-site by binding 30S ribosomal subunit	PRT	1	1
Trimethoprim	Pyrimidine analog, dihydrofolate reductase inhibitor	NUC	8	2
Vancomycin	Glycopeptide, steric hindrance of terminal D-alanyl-D-alanine moieties	CWL	2	2

The raw mass spectra were imported in MATLAB for preprocessing and peak alignment to highly abundant reference peaks, which were identified by TagIdent [161]. Like the reference peaks of *E. coli*, the majority of the high intensity peaks in the *S. aureus* mass spectra are common ribosome associated proteins with relatively high pI, contributing to their high degree of ionization. The alignment peaks are listed in Table 12, next to an exemplary mass spectrum of *S. aureus*.

Table 12. Reference peaks used for spectra alignment during spectral processing of *S. aureus* data set. Listed is the respective protein name, where RL corresponds to Ribosomal Large subunit (50S) and RS to Ribosomal Small subunit (30S), followed by the respective protein unit number. Second column lists corresponding UniProtKB accession number; third column indicates whether the initiator methionine (M) is removed. Fourth column lists the theoretical m/z value, followed by the observed m/z value in the fifth column. Sixth column lists absolute mass error in ppm. Last column shows theoretically calculated isoelectric point (pI). Inset on the right shows average mass spectrum of *S. aureus* with asterisk indicating reference peaks.

Name	UniProtKB	M removed	Observed m/z	Theoretical m/z	Error (ppm)	pI
RL36	Q2FW29	No	4306.7	4306.4	68	10.3
RL34	Q2FUQ0	Yes	5303.8	5303.4	83	12.6
RL33.2	Q2FY22	No	5872.6	5873.7	188	9.7
RL32	P66209	Yes	6353.7	6354.4	95	10
RL30	P0A0G2	Yes	6424.5	6423.5	161	10.1
UPF0337 protein SAOUHSC_00845	Q2FZY9	Yes	6889.1	6888.5	88	5.2
RL29	Q2FW14	No	8091.1	8091.3	18	9.6
RS20	Q2FXY6	Yes	8891.9	8891.2	68	10.5
DNA-binding protein HU	Q5HFV0	No	9627.9	9627.0	92	9.5

After spectral alignment, the relative mass error was within the recommended error range of 300 ppm. From the set of reference peaks, only the UPF0337 protein SAOUHSC_00845 (Q2FZY9) has a significantly lower pI than the pI's calculated for the ribosomal associated proteins (pI of 5.2 versus a pI > 9.4). The UPF0337 protein SAOUHSC_00845 is not a ribosome associated protein, but a member of the CsbD family [197]. This is a family of bacterial general stress response proteins. In addition to the CsbD protein, another non-ribosome associated protein, the DNA-binding protein HU, was used as a reference peak. The HU-protein is a heat stable, bacterial histone-like protein, which also has a relatively high pI (9.5). This protein is known to be one of the most common and abundant nucleoid associated proteins bacteria [198].

4.2.2 Model evaluation and 10 µM validation screen

4.2.2.1 Feature set evaluation

In a similar fashion as for *E. coli*, peaks were evaluated for the binary and MoA classification problem using the RF (for details see Appendix Figure 2), SFS, and SBS (for details see Appendix Figure 3) to yield one aggregated subset of features with high predictive power. The aggregated feature set of *S. aureus* contained 9 peaks for the binary model and 6 peaks for the multiclass MoA model. Details of the binary and MoA aggregated feature sets are listed in Table 13.

Table 13. Aggregated feature set of peaks selected from *S. aureus* spectra for the binary and the mechanism of action model (MoA). Listed are the observed m/z value and the theoretical m/z value of the protein, if identified. For identified proteins is indicated the relative absolute mass error in ppm, UniProt accession number, theoretical isoelectric point (pI), and the corresponding name and notes of the protein, next to post-translational modifications (PTMs), if applicable. Details of peaks marked with asterisk (*) are depicted in Figure 13.

Model	Observed m/z	Theoretical m/z	Error (ppm)	UniProt	pI	Name; notes, PTMs
Binary	4306.7	4306.4	68	Q2FW29	10.3	50S ribosomal protein L36
	4812.5	-	-	-	-	-
	5697.3	-	-	-	-	
	5932.0	5932.9	150	Q2FYU6	9.8	50S ribosomal protein L33 1
	6353.7*	-		-	-	-
	6889.1	6888.5	88	Q2FZY9	5.2	UPF0337 protein SAOUHSC_00845; belongs to the CsbD protein family, a bacterial stress response protein; initiator methionine removed
	8891.9	8891.2	68	Q2FXY6	10.5	30S ribosomal protein S20; methionine removed
	9627.9*	9627.0	92	Q5HFV0	9.5	DNA-binding protein HU
	9724.7*	9723.9	85	Q2FWD8	8.0	50S ribosomal protein L31 type B
MoA	5697.3	-	-	-	-	
	5872.6	5873.7	188	Q2FY22	9.7	50S ribosomal protein L33 2
	5932.0	5932.9	150	Q2FYU6	9.8	50S ribosomal protein L33 1
	6171.8	-	-	-	-	-
	6614.8	-	-	-	-	-
	6978.3	6978.2	15	Q2FZ60	12.2	50S ribosomal protein L28

As for the alignment peaks, most of the selected peaks that were tentatively identified correspond to abundant ribosomal associated proteins with a relatively high pI: all identified proteins except UPF0337 protein SAOUHSC_00845, are relatively basic, having a pI > 8.0. The peak at m/z 6889.1, which was tentatively identified as UPF0337 protein SAOUHSC_00845, was also used for spectral alignment during the pre-processing of the mass spectra. The selection of this peak for the binary model is not surprising, as the protein is a member of the CsbD family, a family of stress-associated proteins [197]. Another identified protein, 50S ribosomal protein L31 type B, observed at m/z 9724.7, was previously implicated to be involved in response to zinc-associated stress [199, 200]. The alignment peak at m/z 9627.9, belonging to DNA-binding protein HU, was also selected for the binary model. This highly conserved protein is known to be involved in stress response mechanism in other bacteria [201].

For both the binary and the MoA model, the peak at m/z 5932.0 was selected. This peak was tentatively identified as 50S ribosomal protein L33 1, a member of the bL33 protein family. This protein is known to be involved in antibiotic response mechanisms in *E. coli* [202]. Another member of the bL33 family was observed at m/z 5872.6. This protein, 50S ribosomal protein L33 2, was also selected for the MoA model. The consistent selection of multiple bL33 family members for both the binary and the MoA model is in line with their annotated role in antibiotic stress response mechanisms. This demonstrates the capability of the feature selection methods to identify relevant, stress associated peaks in the mass

spectra. To illustrate their predictive power, exemplary details of two selected peaks for the binary model are shown in Figure 13.
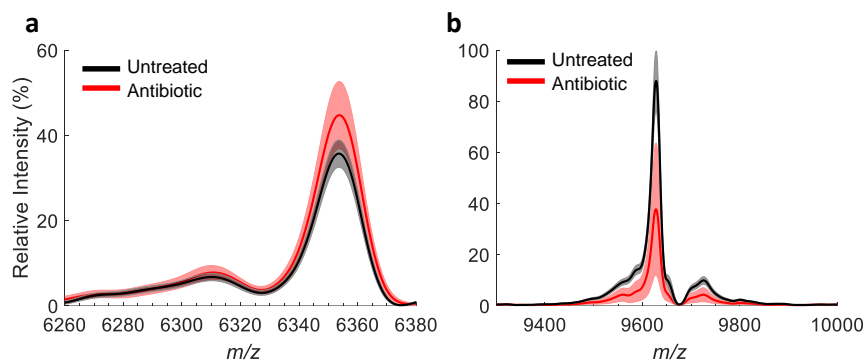

Figure 13. Depicted are mass spectral details from *S. aureus.* (a) Shows detail of unidentified peak at m/z 6353.7. Average mass spectra of untreated cells (black) and treated cells (red), mean absolute deviation (MAD) is indicated with shades. (b) Shows details of peaks at m/z 9627.9 (identified as DNA-binding protein HU) and m/z 9724.7 (identified as 50S ribosomal protein L31 type B). Colors are as described for (a).

In Figure 13a, details of one of the unidentified peaks at m/z 6352.7 are shown. This peak was selected for the binary model, as it allows for a distinct separation between the two classes. The average relative intensity of this peak increased from 35.7% ± 3.2 (black, mean intensity ± MAD) for untreated cells to 44.7% ± 7.9 upon treatment with antibiotics (red). Depicted in Figure 13b is another example of a selected peak, the alignment peak at m/z 9627.6, which was identified as DNA binding protein HU. On its right is another selected peak (m/z 9724.7), which belongs to 50S ribosomal protein L31. Both peaks show over a 2-fold decrease in relative intensity upon treatment with antibiotics. The average relative intensity of the peak at m/z 9627.6 decreases from 87.9% ± 11.7 to 37.7% ± 25.8 upon treatment with antibiotics. The peak at m/z 9724.7 decreases from 9.9% ± 1.5 when cells are untreated to 4.3% ± 2.7 upon treatment with antibiotics.

4.2.2.2 Model internal validation

For *E. coli* it was determined that the aggregated feature set in combination with Q-SVM models yielded the best performing models. Therefore, the same classifier algorithm was applied to the data sets obtained with *S. aureus*. In a similar fashion as described for *E. coli*, the binary and MoA Q-SVM models were evaluated by means of 10-fold cross-validation for internal validation, and by means of the set of blind drugs screened at 10 µM for external validation. The internal validation results for the binary model are summarized in a

confusion matrix, shown in Table 14. The external validation is described in detail in the next subsection (chapter 4.2.2.3).

Table 14. Confusion matrix of the 10-fold cross-validation of binary quadratic support vector machine model with the aggregated feature set of *S. aureus*, encompassing 886 mass spectra (all antibiotics at all concentrations). Indicated is the total number of spectra per class and the corresponding recall and precision value per class, and the overall accuracy in the bottom right in bold.

| | | Model classification | | | |
	Class labels	Treated	Untreated	Total	Recall
True class	Treated	702	17	719	0.98
	Untreated	6	161	167	0.96
	Total	708	178	886	
	Precision	0.99	0.90		**0.97**

Overall, the model accuracy (0.97) is considered high, with 863 out of the 886 mass spectra classified to the correct class. The overall accuracy obtained for the *S. aureus* dataset is similar to what was observed for *E. coli*, which had an accuracy of 0.92. Like the binary model of *E. coli*, the binary model of *S. aureus* is unbalanced, as only 19% of the data (167 out of the 886 spectra) were generated with untreated cells. The imbalance has its main impact on the precision of the class 'Untreated', which is only 0.90, compared to 0.99 for the class 'Treated'. A relatively high amount of false positive observations (17 spectra out of the 178) for the minority class 'Untreated' was observed. This effect of the class imbalance is in line with what was observed for the imbalanced *E. coli* data set. Here, a comparable recall value was found for both the class 'untreated' and 'treated' (0.96 and 0.98, respectively), indicating a relatively high amount of true positive observations for both classes. The results listed in Table 14 show that the Q-SVM classification model in combination with the aggregated feature selection is a robust approach, as it performs equally well on the *S. aureus* data, compared to the results in the previous chapter for *E. coli*.

Next, the MoA model was trained with its corresponding aggregated feature set. Internal validation details of the *S. aureus* MoA model are shown in Table 15.

Table 15. Confusion matrix of the 10-fold cross-validation of mechanism of action quadratic support vector machine model of *S. aureus* using the aggregated feature set, encompassing 886 mass spectra. Spectra from cells were grouped according to the antibiotic mechanism of actions: cell wall synthesis inhibitors (CWL), protein synthesis inhibitors (PRT), nucleic acid synthesis and repair inhibitors (NUC), inhibitors of other type (OTH) and untreated (UNT). Indicated is the total number of spectra per class and the corresponding recall and precision value per class, and the overall accuracy in the bottom right in bold.

	Labels	CWL	NUC	OTH	PRT	UNT	Total	Recall
				Model classification				
True class	CWL	155	22	5	31	5	218	0.71
	NUC	20	74	8	33	2	137	0.54
	OTH	4	9	31	30	14	88	0.35
	PRT	20	13	8	228	7	276	0.83
	UNT	0	2	7	3	155	167	0.93
	Total	199	120	59	325	183	886	
	Precision	0.78	0.62	0.53	0.70	0.85		**0.73**

The MoA model yielded an overall accuracy of 0.73, lower than the binary model (0.97). This is in accordance with internal validation results obtained the MoA model of *E. coli*, which also had a lower model accuracy (0.67) compared to the binary model (0.92). The inadequately defined minority class OTH has relatively poor performance, with recall and precision values of 0.35 and 0.53, respectively. This is similar to what was seen in the internal validation results of the *E. coli* MoA model. Notably, 30 mass spectra from the class OTH are misclassified into the class PRT, the majority of which originate from spectra treated with rifampicin (details not shown). The 14 spectra of the class OTH which are misclassified in the class UNT are almost exclusively mass spectra from cells treated with nitrofurantoin at the lowest concentrations of $^1/_{16}$ and $^1/_{32}$×MIC (details not shown). This further suggests, as was recommended for *E. coli* data set, that the MoA model would benefit from redefining the class OTH.

On average, the recall and precision values for the classes PRT, CWL, and UNT are also on par with what was observed for *E. coli*. The class NUC, which comprises a relatively small fraction of the data (137 out of 886 spectra; 15% of the data set) has relatively low precision (0.62) and recall (0.54). This was mainly due to the confusion of ciprofloxacin and vancomycin by the model (details not shown). Ciprofloxacin is part of the NUC class, but was misclassified as CWL, while vancomycin is part of the CWL class and often misclassified as NUC. The origin of this misclassification cannot be explained by their target sites in the bacterial cell, as their MoA is unrelated. Vancomycin binds to components of the bacterial cell wall to prevent their polymerization through steric hindrance of peptidoglycan glycosyltransferase, thereby disrupting proper cell wall synthesis [203]. Within the class of cell wall synthesis inhibitors assayed here, vancomycin is quite different from the other antibiotics, which are all β-lactams, inhibiting the DD-transpeptidase enzyme. On the other hand, ciprofloxacin inhibits DNA gyrase and topoisomerase, thereby preventing bacterial

DNA from unwinding and duplicating [16]. The confusion of only ciprofloxacin with the cell wall synthesis inhibitors is remarkable, as misclassification of moxifloxacin, another member of the quinolone antibiotics [16], does not occur.

The class NUC is less distinct from the class PRT (33 spectra from PRT misclassified as NUC, mainly spectra from cells treated with trimethoprim), but is also not distinct from class CWL (20 spectra from NUC misclassified as CWL). The strong class imbalance biased towards PRT, which comprises 31% of the data, has a negative impact on the precision of the class PRT. The precision of the class PRT is only 0.70. This relatively low precision is caused by the fact that 94 spectra are assigned to the class PRT, while they actually belong to a different class.

Out of those 94 falsely identified spectra, 31 spectra belong to the class CWL, 33 belong to the class NUC, and 30 belong to the class OTH. Although the recall value of the class PRT is relatively high at 0.83, in absolute numbers the false negative misclassifications involving the class PRT is substantial, with 48 spectra misclassified, Out of these 48 spectra, 20 are falsely assigned to the class CWL, 13 to the class NUC, 8 to PRT, and 7 to the class UNT. As was recommended for the *E. coli* data set, the bias of the MoA model could be reduced by decreasing the relative size of the class PRT compared to the other classes.

4.2.2.3 Model external validation

After internal validation of both the binary and the MoA model trained with the *S. aureus* data, the models were externally validated with the blind set of drugs. The classification results of the external validation are listed in Table 16.

Table 16. Classification details of the binary and mechanism of action (MoA) quadratic support vector machine classification model using the respective aggregated feature sets for external validation on the blind data set. Drugs, listed in the first column, were screened at fixed concentration of 10 µM. The second column (True class binary/MoA) indicates the actual class of the drug, therefore the expected result of the classifier. The third column indicates minimal inhibitor concentration (MIC) values from literature as reference. Binary and MoA model classification details are given in the fourth column, incorrect classifications are stated in brackets. Abbreviations are as follows: CWL: cell wall synthesis inhibitor; NUC: nucleic acid synthesis inhibitor; PRT: protein synthesis inhibitor; OTH: other MoA. Where mass spectral quality was insufficient it states (inadequate signal). Model performance was evaluated using the overall accuracy, indicated at the bottom in bold.

			Model classification	
Drug	**True class binary/MoA**	**Literature MIC (µM)**	**Binary**	**MoA**
Brucine	Untreated		Untreated	Untreated
Ephedrine	Untreated		Untreated	Untreated
Ergotamine	Untreated		Untreated	Untreated
Fenbendazole	Untreated		Untreated	Untreated
Loperamide	Untreated		Untreated	Untreated
Metoprolol	Untreated		Untreated	Untreated
Paroxetine	Untreated		Untreated	Untreated
Sumatriptan	Untreated		Untreated	Untreated
Thalidomide	Untreated		Untreated	Untreated
Umifenovir	Untreated		Untreated	Untreated
Ampicillin	Treated/CWL	92 [157]	Treated	CWL
Azithromycin	Treated/PRT	2.7 [157]	(inadequate signal)	
Cefuroxime	Treated/CWL	2.4 (this thesis)	(inadequate signal)	
Chlortetracycline[b]	Treated/PRT	2.1	(inadequate signal)	
Fusidic acid	Treated/PRT	1.0 [157]	(inadequate signal)	
Nalidixic acid[a]	Untreated	-	Untreated	Untreated
Novobiocin	Treated/NUC	0.2 [204]	(inadequate signal)	
Paromomycin	Treated/PRT	3.2 [205]	(Untreated)	(Untreated)
Tiamulin	Treated/PRT	4.1 [157]	(inadequate signal)	
Trimethoprim	Treated/NUC	27.6 (this thesis)	Treated	NUC
Overall accuracy			**0.93**	**0.93**

a) Inactive on Gram-positives such as *S. aureus*
b) MIC assumed identical to tetracycline

As can be seen in Table 16, of all antibiotic drugs that are expected to affect *S. aureus*, only ampicillin and trimethoprim were assigned to the correct class by both the binary and MoA

model. For six of the expected active drugs (azithromycin, cefuroxime, chlortetracycline, fusidic acid, novobiocin, and tiamulin), the mass spectral signal was of insufficient quality. This means the obtained mass spectra did not pass the outlier detection criteria, and therefore, no classification could be performed. Excluding these unclassified six drugs, the binary model has an overall accuracy of 0.93. This result is in agreement with the values obtained for internal validation (overall accuracy 0.97), confirming a good generalization of the model. The MoA model also has an overall accuracy of 0.93, which is better than was expected from the internal validation (accuracy of 0.76). This is thought to be a result of excluding the six antibiotics from the external data set. Only the drug paromomycin is misclassified by both models as an inactive drug. This is unexpected, as its literature MIC of 3.2 µM is well below the screening concentration of 10 µM, and there are similar aminoglycoside antibiotics like paromomycin in the training data set (neomycin and gentamycin). The misclassification may be a result of the relative high concentration of paromomycin in the screening, approximately 3×MIC, which may have causes a significantly different proteomic response compared to the mass spectra in the training set, which only consisted of 1-$^1/_{32}$×MIC data. Therefore the supposedly strong proteomic changes at 3×MIC might not have been captured by the model.

All spectra from *S. aureus* cells treated with non-antibiotic drugs present in the blind data set were correctly identified as inactive by both the binary and the MoA model. Importantly, spectra from cells treated with the antibiotic nalidixic acid were also correctly identified as inactive by both models, as this antibiotic is inactive on Gram-positive strains such as *S. aureus*. This shows a true positive rate for the class untreated of 1.00 for both models. This result is in agreement with the internal validation of the binary and MoA model, having a recall 0.96 and 0.93 for the class untreated, respectively, thereby also indicating that both models generalize well.

Mass spectra of insufficient quality all originated from cells treated with antibiotic drugs for which the MIC was relatively low (<<10 µM) compared to the screening concentration (see Table 16). Due to the relatively low MIC of these antibiotics, the cells were subjected to such large amounts of antibiotics (up to 50×MIC for novobiocin) that there were simply not enough cells to yield a high quality mass spectrum. For these drugs, the process of model training and validation was repeated, except that these drugs were screened at a concentration of 1 µM instead of 10 µM. The results will be discussed in the next section.

4.2.3 Second model evaluation and 1 µM validation screen

4.2.3.1 Feature set evaluation for 1 µM screen

The new data set to train the model was reduced in size and complexity (only 13 antibiotics, with fewer sub-MIC concentration fractions, for details see Experimental chapter 3.14 and 3.15). The data was subjected to feature selection and yielded an aggregated feature set for a new binary model and MoA model. Feature selection details are in Appendix Figure 4 and Appendix Figure 5 for the binary and MoA classification problem, respectively. The aggregated feature set of *S. aureus* contained 6 peaks for the binary model and 14 peaks for the multiclass MoA model. Details of the aggregated feature set for the binary and MoA classification problem are listed in Table 17.

Table 17. Aggregated feature set of peaks selected from *S. aureus* spectra for the binary and the mechanism of action model (MoA). Listed is the observed m/z value and the theoretical m/z value of the protein, if tentatively identified. For identified proteins is indicated the relative absolute mass error in ppm, UniProt accession number, theoretical isoelectric point (pI), and the corresponding name and notes of the protein, next to post-translational modifications (PTMs), if applicable. Details of peaks marked with asterisk (*) are depicted in Figure 14.

Model	Observed m/z	Theoretical m/z	Error (ppm)	UniProt	pI	Name; notes, PTMs
Binary	4476.1	-	-	-	-	-
	7008.3	-	-	-	-	-
	7018.8	7019.7	128	Q2FZY9	5.2	UPF0337 protein SAOUHSC_00845; belongs to the CsbD protein family, a bacterial stress response protein.
	9627.6	9627.0	92	Q5HFV0	9.5	DNA-binding protein HU
	9653.6	-	-	-	-	-
	10104.1	10104.7	59	Q2FZ45	9.9	30S ribosomal protein S16; methionine removed
MoA	4476.1	-	-	-	-	-
	4779.0	-	-	-	-	-
	4999.4	-	-	-	-	-
	5872.6	5873.7	191	Q2FY22	9.7	50S ribosomal protein L33 2
	6014.7	-	-	-	-	-
	6352.7	-	-	-	-	-
	6616.4	-	-	-	-	-
	6888.3*	6888.5	33	Q2FZY9	5.2	UPF0337 protein SAOUHSC_00845; belongs to the CsbD protein family, a bacterial stress response protein; initiator methionine removed
	7008.3*	-	-	-	-	
	7018.8*	7019.7	128	Q2FZY9	5.2	UPF0337 protein SAOUHSC_00845; CsbD stress response family, bacterial stress response protein
	7351.8	-	-	-	-	-
	9072.3	-	-	-	-	-
	9558.6	-	-	-	-	-
	9653.6	9653.3	31	Q2FZT0	4.0	FeS_assembly_P domain-containing protein

The aggregated feature set selected for this smaller data set shows some overlap with the features selected for the previously screened *S. aureus* data set. Like the previous data set, as again both protein UPF0337 protein SAOUHSC_0084 and DNA binding protein HU are

selected for the binary model. In addition to these two identified proteins, third protein in this data set was tentatively identified as 30S ribosomal protein S16.

For the MoA model, the peak identified as 50S ribosomal protein L33 2 was selected again. This protein was also selected for the MoA model of the larger *S. aureus* data set, accentuating its responsiveness to the stress elicited by the antibiotics. Another peak which was selected for this MoA model was the unidentified peak at m/z 6616.4. This peak was also observed in the previous screen at m/z 6614.8. This minor mass discrepancy of 242 ppm is due to small mass alignment errors, but still within the recommended error margin of 300 ppm. For this MoA model, one additional peak in the aggregated feature could be identified. This peak, observed at m/z 9653.6, was identified as FeS_assembly_P domain-containing protein. This protein is highly similar to Fe-S protein maturation auxiliary factor SufT. This is in agreement with the annotated function of iron-sulfur proteins, as they are reported to be involved in antibiotic stress responses in *S. aureus* [206]. Also selected for the MoA model was the UPF0337 protein SAOUHSC_00845. However, it appears two isoforms of this protein were selected. The full length protein, observed at m/z 7018.8, and the protein with its initiator methionine removed, observed at m/z 6888.3. Details of these peaks are provided in Figure 14.
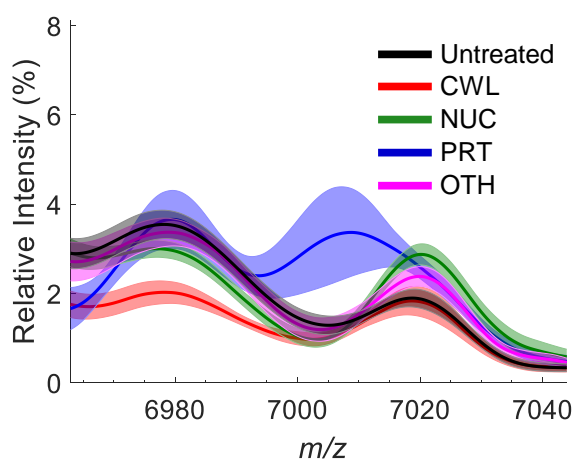
Figure 14. Detail of peaks observed at m/z 6888.3, m/z 7008.3, and m/z 7018.8. Depicted are exemplary mass spectra treated with the antibiotics grouped by their mechanism of action at ¼×MIC. Spectra were colored as follows: untreated cells (black); cell wall synthesis inhibitors (CWL, red); class nucleic acid synthesis and processing inhibitors (NUC, green) and antibiotics with another mechanism of action (OTH). Shades indicate ±½× mean absolute deviation (MAD) from the average mass spectra.

The three peaks shown in Figure 14 originate from UPF0337 protein SAOUHSC_00845 with its initiator methionine removed (m/z 6888.3) and with its initiator methionine still attached (m/z 7018.8), and an unidentified peak in between (observed at m/z, 7008.3). Each of the

peaks shows a unique responsiveness upon cell treatment with antibiotics with a different mechanism of action. For example, the peak at m/z 6888.3 has a lower relative intensity (2.0% ± 0.4 percent point) upon treatment with cell wall synthesis inhibitors (CWL, red) compared to all other classes depicted (on average intensity 3.3% ± 0.7 percent point). Next to that, the striking presence of a peak at m/z 7008.3 (average relative intensity 3.4% ± 2.0 percent point) upon treatment with protein synthesis inhibitors (PRT, blue), which is absent in all other classes depicted (on average 1.3% ± 0.3 percent point). The peak at m/z 7018.8 shows mainly a response towards treatment with the class NUC and OTH, but not to PRT and the class CWL. Possibly, the perceived posttranslational removal of the initiator methionine observed on UPF0337 protein SAOUHSC_00845 has a regulatory effect, in this case involved with stress responses provoked by specific antibiotics. In general, removal of the initiator methionine residue has been shown to have regulatory effects on bacterial processes [207]. The repeated selection of UPF0337 protein SAOUHSC_00845 and 50S ribosomal protein L33 for multiple models of *S. aureus*, regardless of the underlying data set and classification problem, indicates that they may play a more general role in *S. aureus* stress response mechanisms.

4.2.3.2 Binary and MoA model internal validation: 1 µM screen

The binary and MoA models were trained with their respective aggregated feature sets and internally validated using 10-fold cross-validation. Table 18 shows the confusion matrix results of the internal validation of the binary model.

Table 18. Confusion matrix of the 10-fold cross-validation of binary quadratic support vector machine model with the aggregated feature set of *S. aureus*, encompassing 684 mass spectra of the smaller, more balanced *S. aureus* data set. Indicated is the total number of spectra per class and the corresponding recall and precision value per class, and the overall accuracy in the bottom right in bold.

	Class labels	Treated	Untreated	Total	Recall
		Model classification			
True class	Treated	335	19	354	0.95
	Untreated	17	313	330	0.95
	Total	352	332	684	
	Precision	0.95	0.94		**0.95**

The accuracy of 0.95 is comparable to the model performance shown for the binary model of the previous *S. aureus* data set obtained for the 10 µM screening validation (overall accuracy of 0.97) and *E. coli* data set (overall accuracy of 0.92). However, in this new, smaller data set, the class imbalance of the binary model was largely removed, with now 354 spectra obtained for treated *S. aureus* cells, and 330 spectra obtained from untreated *S.*

aureus cells. Consequently, the effects of a balanced dataset on the internal validation, in particular the precision and recall of each class, could be evaluated. For the imbalanced data sets of *E. coli* and *S. aureus*, there was a consistent low accuracy of the minority class 'untreated' (<20% of the overall data set), as the model was unable to identify correct observations from that class. In the case of *E. coli*, the recall was 0.76 and the precision 0.79, considerably lower than for the class 'treated' (0.96 and 0.95 respectively). For the previous *S. aureus* data set, the recall of the class 'untreated' was 0.96 and 0.90, also considerably lower than for the class 'treated' (0.98 and 0.99 respectively). Now, in the case of a balanced data set for the binary classification problem of *S. aureus*, both the recall and the precision of both classes are comparable (0.94-0.95 for each instance). This result illustrates the advantages of having a balanced data set, as the overall number of false positives and false negatives is not biased by the class imbalance of the underlying data, thereby skewing classification results.

The smaller data set of *S. aureus* was also used to train a MoA-based model with its corresponding aggregated feature set. The confusion matrix results for the MoA model is shown in Table 19.

Table 19. Confusion matrix of the 10-fold cross-validation of mechanism of action (MoA) quadratic support vector machine model of *S. aureus*, encompassing 684 mass spectra of *S. aureus* for external validation 1 µM. Antibiotics were grouped according to their MoA: cell wall synthesis inhibitors (CWL), protein synthesis inhibitors (PRT), nucleic acid synthesis and repair inhibitors (NUC), inhibitors of other type (OTH) and untreated (UNT). Indicated is the total number of spectra per class and the corresponding recall and precision value per class, and the overall accuracy in the bottom right in bold.

	Class labels	CWL	NUC	OTH	PRT	UNT	Total	Recall
				Model classification				
True class	CWL	107	0	1	0	2	110	0.97
	NUC	2	50	1	0	4	57	0.88
	OTH	0	0	19	0	3	22	0.86
	PRT	0	2	0	156	7	165	0.95
	UNT	1	1	1	4	323	330	0.98
	Total	110	53	22	160	339	684	
	Precision	0.97	0.94	0.86	0.98	0.95		**0.96**

The overall model accuracy for the MoA model (0.96) is higher compared to the binary model (0.95) based on the same data set. Model accuracy for the previous MoA models was 0.67 (*E. coli*) and 0.76 (*S. aureus* at 10 µM), which are all significantly lower than the 0.96 listed here in Table 19. Two factors are main contributors to this effect: (1) the smaller set of antibiotics used for training in this particular MoA model, and (2) the inclusion of fewer low-fraction MICs, as only concentrations of the antibiotics were used from 1×MIC down to ⅛×MIC, instead of down to $^1/_{32}$×MIC. This indicates that the misclassification rates seen in

previously discussed models (*E. coli* and *S. aureus* data set obtained with 10 µM) was at least partially adversely influenced by the low training set concentrations of $^1/_{16}$ and $^1/_{32}$×MIC . Although a correct classification of the mass spectra is possible down to $^1/_{32}$×MIC, it seems that including solely 1×, ½×, ¼×, and ⅛×MIC is advantageous for the precision and recall values of individual classes. This is a valuable observation in the context of employing the assay in a screening setting, as this will decrease the number of false negatives and false positives, as shown in Table 19.

In this data set, there is still a class imbalance for the MoA model despite the inclusion of fewer antibiotics and concentrations. Comparable to the previously discussed data set and associated models models, the class distribution here is still skewed towards PRT (24% of the data set), but now also skewed towards untreated spectra (48% of the data set). Most of the observed misclassifications seem to be a result of the imbalance towards the class untreated, with 16 spectra (on a total of 330 untreated spectra) classified as untreated while in fact they were treated with one of the 4 other classes. However, the percentage misclassified as 'untreated' (5%) is much lower compared to the previous model obtained at 10 µM, where 28 out of 167 spectra (17%) were misclassified as untreated. It appears that excluding the lowest concentrations of antibiotic treatment ($^1/_{16}$× and $^1/_{32}$×MIC) is the main contributor to the high classification accuracies. Meanwhile, the class OTH has in this data set still has a relatively low prevalence (3%), like the class NUC (8% of the data). The class CWL makes up the remaining 16%. However, the classification accuracy of the class OTH is now strikingly high (recall of 0.86), which was very poor (0.35) in the MoA model trained for the 10 µM validation data set. This is because the class OTH is now only composed of spectra from rifampicin, while previously, the class OTH also contained spectra from cells treated with nitrofurantoin. Nitrofurantoin has a very different MoA than rifampicin, which previously caused in a wide intra-class variation. In the previous MoA model, cells treated with rifampicin were confused with spectra from class PRT. It was thought that this was due to the resemblance of the overall net result of rifampicin and the antibiotics in the class PRT, namely protein synthesis inhibition. It is interesting to observe that for a less diverse OTH class (i.e., only rifampicin), the classification of rifampicin is not confused with the class PRT, despite the net result, protein synthesis inhibition, is the same. Therefore, it seems that the model can, in this case, distinguish very well between protein synthesis inhibited by rifampicin (inhibiting DNA dependent RNA polymerase [208]) and the antibiotics in the class PRT, which are macrolides, aminoglycosides, or tetracyclines. All these antibiotics directly interact with either the 30S or 50S subunit of the ribosome, and not through mRNA inhibition like rifampicin.

Overall, the shift in the class imbalance from the class PRT (in the first *S. aureus* data set) towards 'untreated' in this smaller training set, has shifted the false positive rate from the class PRT to the class 'untreated'. However, despite the described imbalance, the overall number of misclassified spectra is only 29 on a total of 684.

4.2.3.3 Binary and MoA external validation: 1 µM screen

The binary and MoA models obtained for the 1 µM screening data were both externally validated. Details of the classification results are listed in Table 20.

Table 20. Classification details of the binary and mechanism of action (MoA) quadratic support vector machine classification model using the aggregated feature sets for external validation on the blind data set of *S. aureus* data. Drugs, listed in the first column, were screened at fixed concentration of 1 µM. The second column (True class) indicates the actual class of the drug for the binary and MoA model, the expected result of the classifier. The third column, labeled Literature MIC (µM), lists the literature minimal inhibitory concentration (MIC) values of the antibiotic in question as reference. Model classification details are given in the fourth column, incorrect classifications are stated in brackets. Abbreviations are as follows: CWL: cell wall synthesis inhibitor; NUC: nucleic acid synthesis inhibitor; PRT: protein synthesis inhibitor; OTH: other MoA. Overall performance of the model was evaluated using the overall accuracy, indicated at the bottom in bold.

Drug	True class (binary/MoA)	Literature MIC (µM)	Binary	MoA
Ampicillin	Treated/CWL	92 [157]	(Untreated)	(Untreated)
Azithromycin	Treated/PRT	2.7 [157]	Treated	PRT
Cefuroxime	Treated/CWL	9.4 [157]	Treated	CWL
Chlortetracycline	Treated/PRT[b]	2.1	Treated	PRT
Fusidic acid	Treated/PRT	1.0	Treated	PRT
Novobiocin	Treated/NUC	0.2 [204]	Treated	(PRT)
Paromomycin	Treated/PRT	3.2 [205]	Treated	PRT
Tiamulin	Treated/PRT	4.1 [157]	Treated	PRT
Trimethoprim	Treated/NUC	6.9 (this work)	(Untreated)	(Untreated)
Overall accuracy			**0.77**	**0.66**

All cells treated with drugs which previously had yielded low quality spectra now all generated spectra of sufficient quality that could be classified by the model. Trimethoprim and ampicillin, which were correctly identified using the previous data set, when screened at 10 µM, were now both misclassified as inactive by both the binary and MoA model. In the case of ampicillin, this is due to its relatively high MIC of 92 µM. Upon treating *S. aureus* cells with ampicillin at 1 µM, almost a factor 100 below its MIC, it is not surprising that the model classifies the spectra it as inactive. Contributing to this may be that the model was trained with concentrations going down to only $^1/_8 \times$MIC, instead of down to $^1/_{32} \times$MIC, as in the previous model. For trimethoprim, the misclassification comes unexpected, as 1 µM corresponds to approximately $^1/_7{}^{th}$ of the determined MIC, which should be within the capabilities of the model. However, the literature MIC of trimethoprim listed by the EUCAST authority is higher (27.6 µM, 8.0 mg/L) than the MIC determined in this thesis (6.7 µM, 2.0 mg/L). If the actual MIC is in reality closer to the literature value of 27.6 µM, that would explain why treating *S. aureus* cells with 1 µM, almost $^1/_{30} \times$MIC, results in mass spectra that the model classified as inactive.

The binary model assigned all of the spectra obtained with treated cells to the correct class of 'treated'. Even for paromomycin, which was previously classified as an inactive drug, was now classified as an active drug. This suggests that its previous misclassification by the other binary model was most likely due to the class imbalance present in the model.

Regarding the MoA model, the correct class was assigned to all antibiotics in the test set, except for novobiocin. Novobiocin, an aminocoumarin a competitive inhibitor of DNA gyrase [209], was misclassified as a protein synthesis inhibitor (PRT). Internal validation had shown no significant confusion between these two classes. Therefore, it seems most likely that the misclassification is due to novobiocin's relatively low MIC (0.2 μM), a factor 5× lower than the 1 μM screening concentration. It might be that the proteomic response in the mass spectra was too deviating at 5×MIC from what the model was trained on ($1-^1/_8$×MIC) and therefore it was misclassified. Another reason for the misclassification could be that the training set contained only one other gyrase inhibiting antibiotic, the quinolone moxifloxacin, but not a drug of the class aminocoumarins. The exact mechanism of aminocoumarins is slightly different from quinolones, as aminocoumarins bind to the GyrB-subunit of DNA gyrase preventing access to ATPase active site [210]. On the other hand, quinolones mainly inhibit the ligase activity of topoisomerase IV [211]. Therefore, the lack of an aminocoumarin in the training set might explain the misclassification in this case.

An important point to emphasize regarding the external validation (Table 20) is that the predictive power of the models extends beyond the recognition of target sites in the training set. The external validation set included fusidic acid, an antibiotic that interferes with protein synthesis by binding to elongation factor G, preventing its dissociation from the ribosome. None of the protein synthesis inhibitors in the training set had this specific target, but nevertheless the MoA of fusidic acid was correctly predicted by the classification model. The ability to recognize mass spectral effects of antibiotics that were not used in the training set is advantageous, as it potentially allows for identification of drugs with novel target sites within a known mechanism of action class.

4.2.4 Summary

The experiments performed using *S. aureus* show that the assay developed with *E. coli* is readily transferable to another bacterium. Similar to *E. coli* mass spectra, the data-dependent feature selection workflow selected relevant, stress associated peaks, which allowed for the generation of robust and reliable quadratic support vector machine classification models. Similar model accuracies were obtained for *S. aureus* as for *E. coli*.

The external validation of the model showcased a potential shortcoming of the assay. If a drug is too effective at a fixed concentration (10 μM in this case), the cells will not grow. Consequently, there are not enough cells to obtain spectra with sufficient quality. This

occurred for multiple antibiotics in the validation set when screened at 10 µM on *S. aureus*. Therefore, it was required to repeat the screening experiment, employing a 1 µM screening concentration. The second training data set had a more balanced class composition, as it contained fewer antibiotics and relatively more untreated mass spectra. Additionally, this data set did not include the lower concentrations of $^1/_{16}$ and $^1/_{32}$×MIC. The effect of a more balanced class composition was visible in the binary model, where both accuracy and precision for the two classes were equally high (all around 0.95), instead of skewed towards the majority class. For the MoA model, the effect of the different class composition was also very profound, yielding a high overall accuracy of 0.96. Additionally, the now well-defined (although small) class of OTH, which consisted of solely the antibiotic rifampicin, also showed good classification accuracies. Previously, when the class OTH consisted of widely different antibiotics (nitrofurantoin and rifampicin), recall and precision of the class OTH were poor. Now, with the class OTH only defined by rifampicin, classification accuracy was approximately as good as for the other classes.

The elimination of the lowest two concentrations from the training data set ($^1/_{16}$× and $^1/_{32}$×MIC) also contributed to the MoA overall accuracy. In the larger data sets, most spectra which were misclassified by the model as 'untreated' (or misclassified to the majority class PRT) originated from cells that were treated with the lowest concentrations of antibiotics. By excluding the two lowest MIC fractions, fewer spectra were misclassified to the class 'untreated' (although now the majority class), which greatly improved MoA model accuracy. Although the exclusion of the low MIC-data in the training of the model contributed to the increase in model accuracy, there is a trade-off in the sensitivity of the screening assay. In this case, the lowest detectable antibiotic effect lies in the range of $^1/_8$×MIC instead of $^1/_{32}$×MIC for the larger data set. This can be considered sufficiently sensitive, as the model would still be able to pick up potential antibiotic drugs in a screening, which have only 12.5% of the activity of an actual antibiotic drug.

The ability of the *S. aureus* models to classify fusidic acid to the correct class underlines one of the main powers of the assay, namely it can detect (weak) activity within the relatively broadly defined MoAs, although that specific target was not present in the training data. This illustrates that the mass spectral effects that can be detected are specific enough to distinguish different types of MoAs, but is still diverse enough to capture effects that are slightly off-target for what the model was trained on.

4.3 Fungi

In the two previous chapters, the drug screening assay developed in this thesis was elaborately discussed for its applicability on the prokaryotes *E. coli* and *S. aureus* with regard to antibiotics. In this chapter, the applicability of the method was investigated for eukaryote yeasts subjected to antifungal drugs. For this, the developed drug screening method was first applied to detect and classify the proteomic effects of sub-lethal concentrations of several antifungal drugs on *Saccharomyces cerevisiae*. Subsequently, the applicability on the clinically relevant *Candida albicans* was explored.

4.3.1 Saccharomyces cerevisiae

The fungal model organism *Saccharomyces cerevisiae* (strain BY4742) was employed and treated with a small, yet diverse panel of antifungal drugs. First, the MIC values of the antifungal drugs were determined. Subsequently, fungal cells were treated with the set of antifungals at MIC and sub-MIC concentrations (1×, ½×, and ¼×MIC). Following incubation of the yeast in presence and absence of the drugs, mass spectra were recorded. After spectral processing, features were selected using RF, SFS, and SBS to yield an aggregated feature set for both the binary and the MoA classification problem. With the aggregated feature sets, Q-SVM classification models were trained. As described for the experiments concerning bacteria, a binary classification model and a MoA model were internally validated using 10-fold cross-validation and externally validated with a blind set of drugs. In this instance, the blind set of drugs consisted of antifungal and non-antifungal drugs.

4.3.1.1 MIC determination and spectral processing

The drugs used to treat *S. cerevisiae* were amphotericin-B, amorolfine, 5-fluocytosine, caspofungin, and fluconazole, according to EUCAST guidelines for antifungal susceptibility testing. The MIC values and MoA class used for modeling of the respective drugs are listed in Table 21.

Table 21. List of antifungals used for *S. cerevisiae* experiments. Listed are drugs and their corresponding drug class and main target, next to the mechanism of action (MoA) classification abbreviation used for model training, and the antifungals' determined minimal inhibitory concentration (MIC) values (mg/L).

Name	Drug class, target	Class (abbreviation)	MIC (mg/L)
Amphotericin-B	Polyene antifungal, binds ergosterol, thereby disrupting membrane integrity	Membrane disruptor (MEM)	0.25
Amorolfine	Morpholine drug, inhibiting Δ14-sterol reductase and cholestenol Δ-isomerase, depleting ergosterol	Sterol biosynthesis inhibitor (STB)	0.25
5-Flucytosine	Pyrimidine pro-drug, converted intracellularly to fluorouracil, inhibits RNA and DNA synthesis	Nucleic acid synthesis inhibitor (NUC)	16.00
Caspofungin	Echinocandin drug, inhibits β(1,3)-D-glucan-synthase, involved in cell wall synthesis	Cell wall synthesis inhibitor (CWL)	0.008
Fluconazole	Azole drug, inhibits lanosterol 14α-demethylase	Sterol biosynthesis inhibitor (STB)	8.00

The drugs were classified for modeling according to their general MoA as either membrane disruptors (MEM; amphotericin-B), sterol biosynthesis inhibitors (STB; amorolfine and fluconazole), nucleic acid synthesis inhibitors (NUC; 5-flucytosine), and cell wall synthesis inhibitors (CWL; caspofungin). No EUCAST reference MIC values exist for *S. cerevisiae*, but all MICs found are within reasonable range as reported in literature [57, 212-215]. The obtained mass spectra were aligned towards six tentatively identified alignment peaks, which are listed in Table 22.

Table 22. Reference peaks used for spectra alignment during spectral processing of *S. cerevisiae* data set. Listed is the respective protein name, second column lists corresponding UniProtKB accession number; third column lists the theoretical m/z value, followed by the observed m/z value in the fourth column. Fifth column lists absolute mass error in ppm. Last column shows theoretically calculated isoelectric point (pI). Inset on the right shows average mass spectrum of *S. cerevisiae* with asterisk (*) indicating reference peaks.

Protein name	UniprotKB	Theoretical m/z	Observed m/z	Error (ppm)	pI
60S ribosomal protein L41-B	P0CX87	3338.2	3342.1	1186	13.0
Uncharacterized protein YOL038C-A	Q3E7Z9	3622.3	3625.9	991	11.8
Plasma membrane ATPase proteolipid 2 (position 6-43)	P40975	4285.3	4282.4	673	11.6
Uncharacterized protein YGR204C-A	Q8TGT7	4539.3	4538.5	192	10.0
gag-4 (position 98-438)	P0C2J2	4611.9	4614.7	589	4.6
40S ribosomal protein S29-A	P41057	6597.5	6602.1	688	10.3
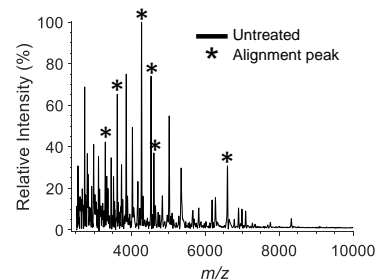
Similar to *E. coli* and *S. aureus*, some of the identified proteins for *S. cerevisiae* are known ribosomal associated proteins (60S ribosomal protein L41-B and 40S ribosomal protein S29-A), and most proteins having a relatively high pI (>10.0). Contrary to the assayed bacteria, almost no mass spectral peaks were observed beyond m/z 8000 (see exemplary mass spectrum *S. cerevisiae* provided in Table 22). Therefore, the mass range was adjusted to m/z 2000-10000. The mass error of the reference peaks was relatively high, with errors above 300 ppm for most peaks. The error was higher than was observed previously for *E. coli* and *S. aureus* (below 300 ppm for all peaks). The exact origin of this error is not known. It can only be speculated that the mass spectrometer required further calibration, or that the alignment peaks were insufficient to remove the mass drift in the spectra. The relatively larger error was not considered an obstacle, as the feature selection process uses the centroid peak values of the detected peaks after alignment. Therefore, the relative error in the centroid peak value is a systematic error. Hence, feature selection can still use the apparent m/z values. Detailed information of the feature selection results for the binary model and MoA model can be found in Appendix Figure 8 and Appendix Figure 9, respectively. Peaks selected in the aggregated feature set are shown in Appendix Table 3. For the binary classification problem, six peaks were selected and for the MoA classification problem five peaks were selected. None of the selected peaks in either of the aggregated feature sets have been identified, even after extending the database search range from ± 300 ppm to ± 1000 ppm to compensate for the present mass error in centroid peak values.

4.3.1.2 Binary model

Although none of the selected peaks of *S. cerevisiae* were identified, illustrative details of three selected peaks for the binary model are provided in Figure 15 to highlight their discrimanitory power between the two classes.
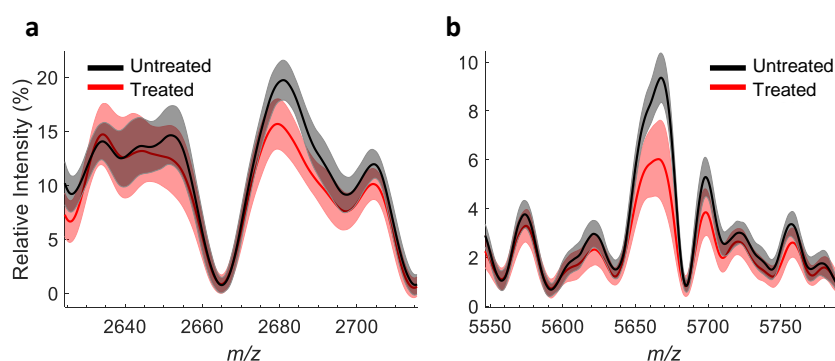

Figure 15. Mass spectral details of *S. cerevisiae*. (a) Details of peak 2679.8, selected for binary model. Average mass spectra of untreated cells (59 spectra, black) and treated cells (122 spectra, red), ± mean absolute deviation (MAD) indicated with shades. Depicted in (b) details of m/z 5659.8, and m/z 5965.7, selected for the binary model. Colors are as described for (a).

The peak at m/z 2679.8 shown in Figure 15a illustrates the separation between untreated and treated *S. cerevisiae* cells. This peak was selected for the binary model, presumably because the relative intensity increased significantly from 15.7% ± 2.3 for untreated cells to 19.5% ± 1.8 for treated cells. Other peaks in this region, between m/z 2630 and m/z 2660, do not allow for this distinction and were consequently not selected. Depicted in Figure 15b, the two selected peaks at m/z 5659.8 and m/z 5665.7 are shown. Both peaks show a relative intensity decrease of almost a factor 2 upon treatment with antibiotics. The intensity of the peak at m/z 5659.8 decreases from 8.2% ± 0.8 to 5.8% ± 1.4 upon treatment with antifungals. The peak at m/z 5665.7 decreases from 9.2% ± 1.0 to 6.0% ± 1.6 percent point relative intensity upon treatment with antifungals. The peaks selected in the aggregated feature set for the binary classification problem were subsequently used to train the corresponding Q-SVM model. The internal validation results of the trained model are shown as a confusion matrix in Table 23.

Table 23. Confusion matrix of the 10-fold cross-validation of binary quadratic support vector machine model with the aggregated feature set of *S. cerevisiae*, encompassing 181 mass spectra (all antifungals at all assayed concentrations). Indicated is the total number of spectra per class and the corresponding recall and precision value per class, and the overall accuracy in the bottom right in bold.

		Model classification			
	Class labels	Treated	Untreated	Total	Recall
	Treated	113	9	122	0.93
	Untreated	6	53	59	0.90
	Total	119	62	181	
	Precision	0.95	0.85		0.92

(True class)

In total, the dataset of *S. cerevisiae* consisted of 181 spectra, of which 122 were obtained from cells treated with antifungal drugs and 59 spectra from untreated cells. This class imbalance, with 67% of the data originating from treated cells, is comparable with the class imbalance the bacterial data sets. Similar to those models, a lower precision and recall for the untreated class is observed (0.85 and 0.90, respectively) compared to the treated class (0.95 and 0.93, respectively). The overall mean accuracy of the binary model for *S. cerevisiae* is 0.92, which is similar to the overall mean accuracy obtained for assayed bacteria (*E. coli*: 0.92, *S. aureus*: 0.95-0.97). The trained model was externally validated using a blind dataset to determine its generalization towards unseen data. The external validation results are shown in Table 24.

Table 24. Classification details of binary classification model for *S. cerevisiae* for external validation on the blind data set. The second column (True class) indicates the expected result of the classifier. Details of correct classifications are listed, and incorrect classifications are stated in brackets. Overall performance is reported at the bottom.

Drug	True class	Model classification
Loperamide[b]	Untreated	(Treated)
Cefuroxime[d]	Untreated	Untreated
Ribavirin[a]	Untreated	Untreated
Clotrimazole	Treated	Treated
Voriconazole	Treated	Treated
Fenpropimorph	Treated	Treated
Nystatin	Treated	Treated
Tavaborole[c]	Treated	Treated
Overall accuracy		**0.88**

[a] Antiviral   [c] Mechanism of action not present in training data
[b] Opioid   [d] Antibacterial

The blind set of drugs was composed of several antifungal drugs: clotrimazole, voriconazole (two azoles, similar to the azole in the training set), fenpropimorph (similar to amorolfine in the training set), nystatin (similar to amphotericin-B in the training set), and tavaborole (which did not have a respective drug in the training class). In addition to these antifungal drugs, three other drugs with no antifungal activity were assayed: cefuroxime (antibacterial), loperamide (an opioid), ribavirin (an antiviral drug).

External validation resulted in an accuracy of 0.88, which indicates a reasonably good performance, and is in line with the internal validation accuracy of 0.92. However, the binary model misclassified cells as 'Treated' with loperamide (an opioid receptor agonist). This misclassification might be due to the relatively low precision of the class 'untreated' of the binary model (0.85). However, literature reports exist which implicate tramadol, another opioid receptor agonist similar to loperamide, as having in vitro antifungal activity against *Candida* yeasts [216]. Thus, there may be a (nonlethal) proteomic response when exposed to loperamide which shows variations closer to mass spectra obtained with treated cells rather than untreated cells. Nevertheless, in this work the classification of loperamide as being an active antifungal is considered incorrect. Further experiments should clarify whether loperamide results truly in an antifungal proteomic response in *S. cerevisiae*. Cefuroxime, an antibacterial β-lactam drug, was correctly identified as inactive drug. Ribavirin, an antiviral pyrimidine analog, was correctly identified as inactive on *S. cerevisiae*. Although ribavirin has been implicated as having mild antifungal activity against *C. albicans* [217], it was not classified by the model as such for *S. cerevisiae* in this experiment.

The mass spectra from cells treated with the two azole drugs in the blind set, clotrimazole and voriconazole, were correctly identified as antifungal drugs. Fenpropimorph and

nystatin, both having an analogous drug in the training set of the model (amorolfine and amphotericin B, respectively), were correctly identified as antifungal drugs.

Among the blind set there was one drug, tavaborole, with a mechanism of action that was not part of the training set. Tavaborole is an antifungal protein synthesis inhibitor, as it inhibits leucyl-tRNA synthetase [55]. Despite the fact that the model was not trained on this (or a similar) type of antifungal, the binary model correctly classified the mass spectra from *S. cerevisiae* exposed to tavaborole as being treated with an antifungal. This indicates that the binary model is able to pick up general stress response signatures in the fungal mass spectra, even beyond to what it was trained for. This is advantageous screening characteristic, as it indicates that the assay might have the ability to detect drugs with novel mechanisms of action.

4.3.1.3 MoA model

Before the performance of the MoA model will be presented and evaluated, exemplary peaks selected for the MoA will be discussed. Depicted in Figure 16 are two peaks which were selected in the region of m/z 3600-4100 and two selected peaks in the region of m/z 5600 - 5750.
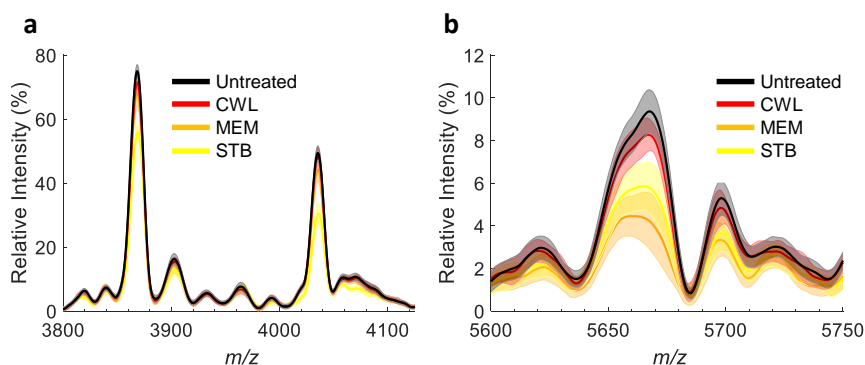

Figure 16. (a) Details of peaks observed at m/z 3868.6 and 4035.5, selected for the mechanism of action (MoA) model. Colors are as follows: average spectra from untreated cells (black); cells treated with cell wall synthesis inhibitors (CWL, red), the class membrane disruptors (MEM, orange), sterol synthesis inhibitors (STB, yellow). Shades indicate ± mean absolute deviation. (b) Details of peaks observed at m/z 5659.8 at 5665.7, both selected for MoA model. Colors are as described for (a).

Figure 16a shows the average intensity of the peak at m/z 3868.6, which was selected for the MoA model. Although this peak allows for the distinction of the classes MEM (relative intensity 68.3% ± 4.1) and STB (55.9% ± 2.1), the peak is less suitable for the distinction between CWL (71.5% ± 2.1) and untreated cells (74.9% ± 2.0). The peak at m/z 4035.5 was

selected for the MoA model as well, which shows similar discriminatory properties, with a strong influence on the peaks' intensity depending on antifungal treatment. Intensity of this peak is highest for untreated cells (49.4% ± 2.2), but not significantly different from cells treated with antifungals of the class CWL (48.3% ± 2.8). However, its relative intensity drops significantly upon treatment with the class MEM (44.2% ± 3.7) and even more upon treatment with antifungal of the class STB (30.3% ±3.3). Figure 16b shows details of peaks observed at m/z 5659.8 and m/z 5665.7, which were also selected for the binary model (Figure 15b). Similar to the peak at m/z 3868.6 in Figure 16a, the spectra of cells treated with CWL and untreated cells show a comparable relative intensity the selected peak at m/z 5659.8 (7.6% ± 0.8 and 8.2% ± 0.8, respectively), but are still significantly higher than for the class MEM and STB (4.4% ± 0.9 and 5.7% ± 1.1, respectively). Analogous information is obtained from the peak at m/z 5665.7, where similar relative intensities were obtained for the classes CWL and untreated (8.2% ± 0.8 and 9.2% ± 1.0, respectively) and significantly lower intensities for the classes STB and MEM (5.8% ± 1.1 and 4.3% ± 1.2, respectively). The MoA model was trained with five selected peaks in total. The results of internal validation of the MoA model based on the selected peaks are shown in Table 25.

Table 25. Confusion matrix of the 10-fold cross-validation of mechanism of action quadratic support vector machine model of *S. cerevisiae* using the aggregated feature set. Antifungals were grouped according to their mechanism of actions: cell wall synthesis inhibitors (CWL), sterol biosynthesis inhibitors (STB), nucleic membrane disruptors (MEM), and untreated (UNT). Indicated is the total number of spectra per class and the corresponding recall and precision value per class, and the overall accuracy in the bottom right in bold.

		Model classification					
	Class labels	CWL	MEM	STB	UNT	Total	Recall
True class	CWL	22	0	0	7	29	0.76
	MEM	2	27	1	1	31	0.87
	STB	1	0	61	0	62	0.98
	UNT	6	0	0	53	59	0.90
	Total	31	27	62	61	181	
	Precision	0.71	1.00	0.98	0.87		**0.90**

The overall mean accuracy is 0.90, reflecting a good model performance. The limited complexity due to the relative low number of antifungal drugs and sub-lethal concentrations might have contributed to the relatively good performance. The model suffers from a small class imbalance, which translates to relatively low recall for the underrepresented classes CWL and MEM (29 and 31 spectra and a recall of 0.76 and 0.87, respectively) compared to the class of STB and UNT (62 and 59 spectra and a recall of 0.98 and 0.90, respectively). The precision of the class CWL is also relatively low, which is mainly attributed to confusion with the class 'untreated'. This confusion involves the spectra from cells from the class CWL

treated with the lowest concentrations (¼×MIC, details not shown). The observed confusion of the model is in line with the observations discussed for the exemplary peaks in Figure 15, where the mass spectral peaks obtained with untreated cells frequently overlapped with the spectral peaks from the class CWL. A good performance is seen for the class MEM, with a precision of 1.00. This indicates that the MoA model was able to correctly classify all spectra for that class during internal validation. However, the recall of the class MEM is slightly lower at 0.87, which indicates a relatively high number of false negatives for this class. Overall, the peaks in the aggregated feature set seem to contain sufficient discriminatory information to distinguish the different MoA classes. This was further evaluated by means of external validation of the model, as was described for the binary model. The results of the external validation are listed in Table 26.

Table 26. Classification details of mechanism of action (MoA) model for *S. cerevisiae* during external validation on the blind data set. The second column (True class) indicates the expected result of the classifier: cell wall synthesis inhibitors (CWL), sterol biosynthesis inhibitors (STB), nucleic membrane disruptors (MEM), or untreated. Third column indicates the classifications by the model. Incorrect classifications are stated in brackets. Overall performance is indicated at the bottom.

Drug	True class	Model classification
Loperamide[b]	Untreated	Untreated
Cefuroxime[d]	Untreated	Untreated
Ribavirin[a]	Untreated	Untreated
Clotrimazole	STB	STB
Voriconazole	STB	STB
Fenpropimorph	STB	STB
Tavaborole[c]	PRT	(MEM)
Nystatin	MEM	(STB)
Overall accuracy		**0.75**

[a] Antiviral drug   [c] MoA not present in training data
[b] Opioid   [d] Antibacterial

Among the drugs in the external validation set are the two commonly used triazole drugs, clotrimazole and voriconazole. Both these drugs are very similar to fluconazole, the sterol biosynthesis inhibitor (STB) in the training set of the MoA model. Both antifungals were correctly classified as such, which is in line with the high accuracy of that class seen in the internal validation of the MoA model. The MoA model was also able to correctly identify compounds that do not have an antifungal action, as is the case for the antiviral ribavirin, the opioid loperamide, and the antibiotic cefuroxime. In comparison with the binary model, the performance is better in this regard, where loperamide was incorrectly identified as treated.

The varying outcome between the binary and the MoA model is attributed to the class-dependent peak selection. The data-dependent feature selection resulted in some overlap of the aggregated feature sets of the binary and MoA classification problem. In total, 4 peaks were selected for both classification problems, but each classification problem also had specific peaks selected uniquely for its respective classification problem (see Appendix Table 3). The peaks selected for the binary model may have shown higher similarity between the response of loperamide and the treated spectra, while for the MoA model a higher similarity in peak values was found for untreated spectra.

Two misclassifications were found for the MoA model, where tavaborole and nystatin were misclassified as MEM and STB, respectively. For tavaborole, it is understandable that the model was unable to assign the class correctly, as its class (protein synthesis inhibitor) was not part of the classification model training set of *S. cerevisiae*. Taking into account that tavaborole is not classified as 'untreated', it can be considered the best outcome under the circumstances, as it could be considered worse if tavaborole would have been classified as an inactive drug.

The misclassification of cells treated with nystatin was not expected based on the internal validation results, as the class precision of MEM was 1.00. It is thought that nystatin (class MEM) was misclassified to the class STB, as these two mechanisms of action have the same overall net result. As both the class MEM and STB disrupt membrane integrity, the cells proteomic response may therefore be relatively similar to each other. Only one MEM compound (amphotericin-B) was included in the training set, while two compounds were included for the class STB (amorolfine and fluconazole). As a consequence, it may be that the intra-class variation of STB captures more overlap with the proteomic response of nystatin than solely the intra-class variation caused by solely amphotericin-B, as all three antifungals overall disrupt membrane stability through a degree of interference with ergosterol. This brings the used class division of the training set itself into the discussion. Amphotericin-B directly binds to ergosterol [218], and amorolfine [219] and fluconazole [220] disrupt the biosynthesis of ergosterol by inhibiting specific enzymes in the sterol biosynthesis route. Nevertheless, one could consider them all a member of the more broadly defined class of inhibitors that disrupt membrane stability through interference with ergosterol. To improve class definition, one could first perform exploratory data analysis using, for example, unsupervised clustering approaches to assist in determining class boundaries and class-inclusion criteria. To properly asses the performance of each class in the training set, the validation set should in that case preferably contain one (or multiple) members of that respective class to capture the variation of intra-class proteomic effects.

This misclassification observed for the MoA models of *S. cerevisiae* reveals a possible resolution limit of the developed screening assay. If the overall net result of the classes

involved is similar, the model cannot properly distinguish them when training models with multiple different mechanisms of action classes, as was seen for the classes MEM and STB. To further validate the model, it would be advised to include one or multiple echinocandins (inhibiting cell wall synthesis) and pyrimidine analogues (inhibiting nucleic acid synthesis) in the blind test set, to also evaluate the distinction of the model between those classes.

4.3.2 Candida albicans

After demonstrating the assay's applicability for *S. cerevisiae*, results obtained with the developed assay applied to the clinically relevant eukaryote yeast *C. albicans* will be discussed in this subchapter. The MIC values of *C. albicans* (ATCC 90028) were determined for a set of antifungal drugs, and subsequently the cells were treated with sub-MIC concentrations (1×MIC, ½×MIC, and ¼×MIC) of those drugs. Mass spectra of the cells were recorded, and feature selection using RF, SFS, and SBS was performed to yield aggregated feature sets for both the binary and the MoA models. The constructed Q-SVM classification models were evaluated solely by internal 10-fold cross-validation. This was done to obtain a preliminary indication of the model performance when trained with *C. albicans* data, but the models' generalization towards unknown data cannot be discussed.

4.3.2.1 MIC determination and spectral processing

The MIC values were determined for a small set of antifungals according to EUCAST guidelines for antifungal testing. Drugs were classified as sterol biosynthesis inhibitors (STB; fluconazole and miconazole), nucleic acid inhibitor (NUC; 5-flucytosine), and cell wall synthesis inhibitors (CWL; caspofungin). The MIC values are listed in Table 27.

Table 27. List of antifungals used for *C. albicans* experiments. Listed are drugs and their corresponding drug class and main target, next to the mechanism of action (MoA) classification abbreviation used for model training, and the antifungals' determined minimal inhibitory concentration (MIC) values (mg/L).
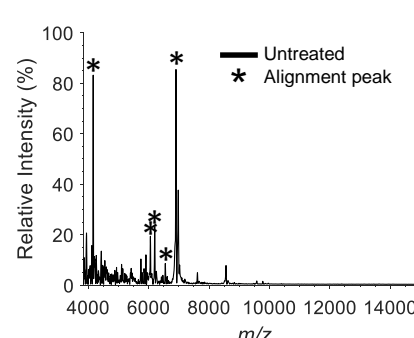
Name	Drug class, target	Class (abbreviation)	MIC (mg/L)
5-Flucytosine	Pyrimidine pro-drug, converted intracellularly to fluorouracil, inhibits RNA and DNA synthesis	Nucleic acid synthesis inhibitor (NUC)	0.5
Caspofungin	Echinocandin drug, inhibits β(1,3)-D-glucan-synthase, involved in cell wall synthesis	Cell wall synthesis inhibitor (CWL)	0.125
Fluconazole	Azole drug, lanosterol 14α-demethylase Inhibitor	Sterol biosynthesis inhibitor (STB)	0.25
Miconazole	Azole drug, Lanosterol 14α-demethylase Inhibitor	Sterol biosynthesis inhibitor (STB)	32

Out of the set of assayed antifungals, the EUCAST authority only provides a reference value for fluconazole of ≤ 2 mg/L [159], which is within reasonable accuracy as the MIC reported here of 0.25 mg/L. The CLSI provides a reference value for caspofungin ≤ 0.25 mg/L [221], also in line with the value reported in this thesis (0.125 mg/L). The obtained MIC values for the other antifungals are also within range of reported literature values determined under similar circumstances [222, 223]. Only for miconazole, the obtained MIC of 32 mg/L was relatively high compared to literature values (0.25 mg/L [224]), which may partially due to the subjectivity involved in determining the MIC visually [225].

After the *C. albicans* cultures were exposed to the antifungals, mass spectra were recorded and subsequently aligned to abundant identified reference peaks. Listed in Table 28 are several tentatively identified protein peaks used for mass spectra alignment.

Table 28. Reference peaks used for spectra alignment during spectral processing of *C. albicans* data set. Listed is the respective protein name, where RL corresponds to Ribosomal Large subunit (50S) and RS to Ribosomal Small subunit (30S), followed by the respective protein unit number. Second column lists corresponding UniProtKB accession number; third column indicates whether the initiator methionine (M) is removed. Fourth column lists the theoretical m/z value, followed by the observed m/z value in the fifth column. Sixth column lists absolute mass error in ppm. Last column shows theoretically calculated isoelectric point (pI). Inset on the right shows average mass spectrum of *C. albicans* with asterisk (*) indicating reference peaks.

Name	UniprotKB	Initiator M removed	Theoretical m/z	Observed m/z	Error (ppm)	pI
Mfa1p	A0A1D8PI68	Yes	4163.6	4166.0	580	9.4
RL40	C4YHX3	No	6062.3	6058.3	661	10.3
RL39	Q96W55	Yes	6199.3	6201.2	302	12.3
RS29A	C4YMQ1	Yes	6470.3	6468.3	322	9.8
RL29	C4YCU6	Yes	6982.1	6980.8	177	11.0

These alignment peaks were mainly basic (pI >9.4) ribosomal associated proteins, except for Mfa1p, which has mating pheromone activity [226]. As was observed for *S. cerevisiae*, almost no peaks were observed beyond m/z 8000. The mass error is higher (above 300 ppm for 4 out of 5 peaks) than was observed for *E. coli* and *S. aureus* (below 300 ppm), but comparable to *S. cerevisiae*. As for *S. cerevisiae*, the exact origin of the relatively large error is unknown, but not considered a major issue. After spectral alignment, feature selection was performed as described previously. Details of feature selection using RF, SFS, and SBS are provided in Appendix Figure 6 and Appendix Figure 7. All peaks selected in the aggregated feature set for Q-SVM model construction are listed in Appendix Table 2. None of the selected peaks could be identified, even by extending the database mass search to ± 700 ppm, based on the largest error (661 ppm) observed for RL40 in this data set.

4.3.2.2 Binary model

Similar to the chapters of the other organisms, the binary model results will be presented and discussed first. Despite the unknown identity of the selected peaks, the information contents of several peaks that were employed to train the binary model are shown in Figure 17.
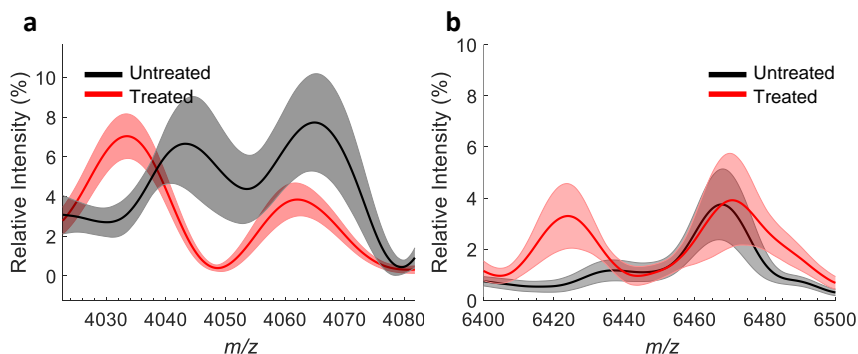

Figure 17. (a) Mass spectral details of *C. albicans*. In (a) details of selected peak at m/z details of peak 4033.5. Average mass spectra of untreated cells (black) and treated cells (red), mean absolute deviation is indicated with shades. Depicted in (b) details of selected peak observed at m/z 6424.0. Colors are as described for (a).

Figure 17a depicts one of the peaks selected for the binary model, observed at m/z 4033.5. Mass spectra from cells treated with antifungals (red) show a peak with an average relative intensity of 7.0% ± 1.1, while mass spectra from untreated cells (black) lack this peak almost completely (intensity 3.1% ± 0.9). The separation between untreated and treated cell spectra can also be found for the adjacent peaks at m/z 4043.3 and m/z 4063.0, although these were not selected for the binary model. This may be due to the relatively large MAD for untreated cells observed for these peaks. For example, at the peak at m/z 4043.3 the MAD is over one-third of the signal, at 6.6% ± 2.3. The relatively larger MAD in the data from untreated cells might originate from the fact that the cells were not synchronized, but an additional comparative study would be required to confirm this. However, the MAD of the spectra from cells that were untreated is relatively small in some other areas, such as the selected peak at m/z 6424.0, shown in Figure 17b. Here, the intensity of treated cells was relatively high, 3.3% ± 1.3, compared to spectra from untreated cells at 0.7% ± 0.3. The Q-SVM models using the aggregated feature set were constructed with the selected peaks and the resulting confusion matrix of the internal validation using 10-fold cross-validation of the binary model is shown in Table 29.

Table 29. Confusion matrix of the 10-fold cross-validation of binary quadratic support vector machine model with the aggregated feature set of *C. albicans*, encompassing 185 mass spectra (all antifungals at all assayed concentrations). Indicated is the total number of spectra per class and the corresponding recall and precision value per class, and the overall accuracy in the bottom right in bold.

		Model classification			
	Class labels	Treated	Untreated	Total	Recall
True class	Treated	126	1	127	0.99
	Untreated	8	50	58	0.86
	Total	134	51	185	
	Precision	0.94	0.98		**0.95**

Comparable to the other binary models discussed in this thesis, the class imbalance of the data set results in a relatively low recall value for the minority class untreated (0.86) compared to the class treated (0.99). Nevertheless, a high overall mean accuracy of 0.95 was obtained during internal validation of the binary model obtained with *C. albicans* data. The fact that the model has a relatively low recall for the class untreated (compared to the other organisms) may be explained by looking at details of some peaks that were selected for this model. The relatively large MAD, present in several of the selected peaks of the class untreated, may have contributed to this effect. External validation was not performed for *C. albicans*. However, based on its similar model performance during internal validation compared to *S. cerevisiae* (and the assayed bacteria), it indicates promising results if external validation was to be conducted.

4.3.2.3 MoA model

The MoA model was constructed with five unidentified peaks (listed in Appendix Table 3). Exemplary peaks selected for the MoA model of *C. albicans* are shown in Figure 18.
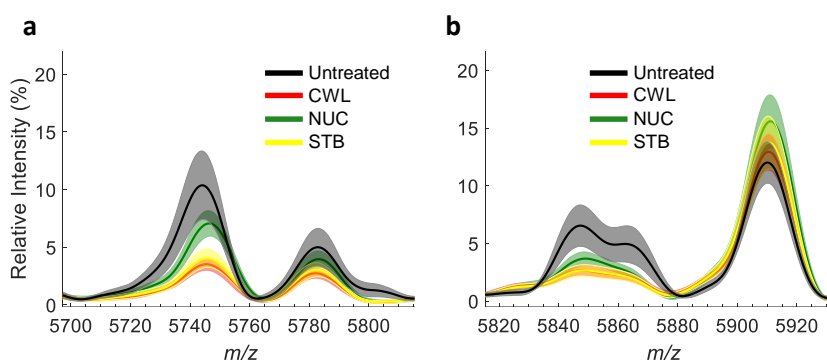

Figure 18. Details of peaks selected for the mechanism of action (MoA) model. In (a) details of peak at m/z 5745.3 Spectra are averages of the whole data set colored as follows: untreated cells (black); cell wall synthesis inhibitors (CWL, red); class nucleic acid synthesis and processing inhibitors (NUC, green) and antifungals inhibiting sterol biosynthesis (STB, yellow). Shades indicate ± mean absolute deviation. (b) Details of peak at m/z 5848.1 and 5910.7. Colors are as described for (a).

Figure 18a shows details of the peak at m/z 5745.3. At this peak, the distinction between untreated cells spectra (10.3% ± 2.9) and spectra from cells treated with 5-fluocytosine (NUC; 7.0% ± 1.1) is significant, as is the distinction with the spectra from cells treated with antifungals of the classes CWLs (3.5% ± 0.5) and STBs (4.1% ± 0.8). Nevertheless, the spectra of CWL and STB do overlap slightly. A similar observation on the overlap of the classes CWL and STB can be made from the peak at m/z 5848.1 in Figure 18b. The relative intensity for the untreated spectra is 6.5% ± 1.8, while for the cells treated with antifungals of the class NUC the intensity is significantly lower at 3.7% ± 0.6. For both CWL (2.7% ± 0.4) and STB (2.7% ± 0.5), the intensity is even lower than for NUC, but those two classes are indistinguishable from each other. Similarly, the selected peak at m/z 5910.7 (Figure 18b) shows relatively high intensity for spectra obtained with cells treated with NUC (15.6% ± 2.3), which is different from untreated cells (12.0% ± 1.8). However, the distinction between CWL (12.9% ± 1.6) and STB (13.7% ± 2.3) and untreated is, once again, not observed for this peak. As was seen for peaks selected for the binary model, the peak at m/z 5745.3 shows a relatively large MAD in its relative intensity (10.3% ± 2.9) for the untreated cells compared to the spectra from cells treated with the antifungals. For the peak at m/z 5848.1, the MAD is roughly a factor 3 larger (at 1.8 percent point MAD) for the untreated cells' spectra compared to the treated cells' spectra (0.4-0.6 percent point MAD). The internal validation results of the MoA model are shown as a confusion matrix in Table 30.

Table 30. Confusion matrix of the 10-fold cross-validation of mechanism of action quadratic support vector machine mechanism of action (MoA) model of *C. albicans*, encompassing 185 mass spectra. Antifungals were grouped according to their mechanism of actions: cell wall synthesis inhibitors (CWL), sterol biosynthesis inhibitors (STB), nucleic acid synthesis and repair inhibitors (NUC), and untreated (UNT). Indicated is the total number of spectra per class and the corresponding recall and precision value per class, and the overall accuracy in the bottom right in bold.

	Class labels	Model classification				Total	Recall
		CWL	NUC	STB	UNT		
True class	CWL	21	0	10	0	31	0.68
	NUC	0	29	1	2	32	0.91
	STB	9	1	53	1	64	0.83
	UNT	0	3	0	55	58	0.95
	Total	30	33	64	58	185	
	Precision	0.70	0.88	0.83	0.95		**0.85**

The performance during internal validation was reasonably well, with an overall accuracy of 0.85. This performance is slightly worse than the performance of the MoA model reported for *S. cerevisiae* (0.90). The confusion matrix shows that the lowest accuracies occur for the classes CWL and STB, as the MoA model is unable to make a proper distinction between spectra from cells treated these two antifungal classes. This particular confusion resulted in a total of 19 misclassifications, indicating that the selected peaks do not contain enough discriminatory power for these two classes. This is in line with the observation of the exemplary peaks in Figure 18a, where the distinction between the classes CWL and STB is less pronounced than between the classes untreated and NUC. Another reason might be that, despite the fact that the sterol biosynthesis inhibitors (inhibiting lanosterol 14α-demethylase [46]) and the cell wall synthesis inhibitors (inhibiting β(1,3)-D-glucan-synthase [53]) have a different target, their biological net result is similar, namely an increase in cell permeability which eventually causes cell lysis. This may result in a highly similar proteomic response, or at least the differences between the azole drugs and echinocandins cannot be resolved under current assay conditions in *C. albicans*. In addition, the MoA model also suffers from a minor class imbalance, as the classes CWL (consisting only of mass spectra only from caspofungin) and NUC (comprising only the antifungal 5-fluocytosine) each accounting for 17% of the data. On the other hand, the classes of untreated spectra and STB are relatively large, with 31% and 35% of the data, respectively. Though this does not seem to have any obvious effect on the overall classification accuracy of each of the classes, it does contribute to the lower recall and precision of the classes CWL and STB. For the class CWL, a relatively large fraction of the spectra (10/31) is misclassified as STB. Conversely for the class STB, 9 out of the 64 spectra were misclassified as CWL. This confusion mainly had its impact on the relatively small class of CWL, resulting in a relatively low precision and recall of 0.70 and 0.68 respectively. For the class STB, the confusion with the class CWL has

less of an effect on the precision and the recall (both 0.83) due to its relative larger sample size of 64 spectra. The classes NUC and 'untreated' are well distinguishable from each other, and the other classes. This is reflected in a high precision and recall score for both the class NUC (0.88 and 0.91 respectively) and the class 'untreated' (both 0.95).

Although the proof-of-concept study demonstrates that the workflow can be applied to *C. albicans*, it also shows that the currently employed class definitions could be further optimized, as was suggested for *S. cerevisiae* data set. It appears that the used classes of CWL and STB, with which it was attempted to resolve the effects of azole and echinocandin drugs, do in fact show similar cellular effects as measured in the MALDI-TOF assay. This indicates that the resolution of the method is limited, though further experiments including different feature selection methods or modeling approaches may increase the resolution. For future work, it is advised to also use additional echinocandins and azole drugs in the model training and test set confirm the (dis)similarity between those classes. Additionally, other drugs that could be categorized in the class of sterol biosynthesis inhibitors, such as allylamines (inhibiting squalene monooxygenase) [52], morpholine antifungal drugs [227], and drugs directly interacting with ergosterol, such as the polyene antifungals (such as amphotericin-B and nystatin [228] could be investigated to see how well the current assay resolves these stresses.

4.3.3   Summary

To summarize, the applicability of the developed assay has been shown for the eukaryote yeasts *S. cerevisiae* and *C. albicans*. The performed studies reflect that the assay is readily transferable to eukaryote cells to detect the effects of antifungal drugs. The data-dependent workflow selected relevant peaks, which, although unidentified, allowed for the generation of robust and reliable quadratic support vector machine classification models.

It would be of interest to perform external validation for *C. albicans*, in order to advance and further understand the application of the developed method. The external validation of the *S. cerevisiae* MoA model pointed out an inherent shortcoming of the developed method, where a MoA will inherently be assigned to the incorrect MoA if that particular MoA was not present in the training set. Nevertheless, the binary model was able to correctly identify mass spectra from cells treated with an unknown MoA as 'treated' (tavaborole, a protein synthesis inhibitor).

The MoA model of both *S. cerevisiae* and *C. albicans* indicated that the employed class definition is suboptimal to correctly identify antifungal drugs, if their overall effect in terms of cellular stress is similar. For *S. cerevisiae*, this manifested itself in confusion between the class of STB and MEM, as both classes of antifungals disrupt the membrane through interference with ergosterol. For *C. albicans*, the model had trouble distinguishing the class

STB from CWL, as these antifungal classes all result in fungal cell membrane or cell wall instability. Further analysis of larger data sets would be required to show how well the distinction can be made between these highly similar classes. It would be of value to investigate additional feature selection approaches, or different class definitions for modeling. This could assist in determining whether or not there are specific peaks in the mass spectrum that allow for a better distinction between the classes which currently show a high similarity.

4.4 HeLa

After demonstrating the transferability of the MALDI-TOF MS assay from prokaryotes to eukaryote fungal species to detect sub-lethal effects of specific drugs, an exploratory analysis of the method applied to human HeLa cells was undertaken. Two experiments have been performed for this purpose, which employed different kinds of stress. Firstly, the effect of a diverse set of drugs on the proteome of HeLa was investigated. Secondly, the proteomic effect on HeLa cells subjected to physical stresses was explored. In those experiments, HeLa cells treated with drugs were compared to cells incubated at an elevated temperature of 43 °C and HeLa cells that were exposed to UV-light.

4.4.1 Drug stress

4.4.1.1 Toxicity determination and spectral processing

The CC_{50} concentrations of the drugs investigated were determined using the commercially available CellTiter-Blue® viability assay kit. The drugs were selected to cover a diverse range of pharmacological classes, from anticancer drugs, such as tubulin polymerization inhibitors, to different types of hormones, such as corticosteroids, tamoxifen, and thyroid hormone. The drugs investigated, and their respective CC_{50} concentrations, are listed in Table 31.

Table 31. List of drugs used in HeLa experiments, their drug class and main target, mechanism of action (MoA) class abbreviation used for modeling, and their respective 50% cytotoxicity values (CC_{50}, in mM).

Name	Drug class, target	MoA class	CC_{50} (mM)
Combretastatin	Dihydrostilbenoid drug, tubulin polymerization inhibitor	TUB	0.234
Paclitaxel	Taxane drug, tubulin depolymerization inhibitor	TUB	0.062
Vinblastine	Vinca alkaloid, tubulin polymerization inhibitor	TUB	0.066
Colchicine	alkaloid, tubulin polymerization inhibitor	TUB	0.381
Dexamethasone-21-phosphate	Corticoid steroid hormone, binds glucocorticoid receptor	CORT	0.150
Prednisolone	Corticoid steroid hormone, binds glucocorticoid receptor	CORT	0.240
L-Tyroxine	Thyroid hormone T4 substitute; thyroid nuclear receptors	THR	0.127
Tamoxifen	Selective estrogen receptor modulator (prodrug), estrogen receptors	SERM	0.020
Ciclosporine	Immunosuppressant, cyclophillin binder	IMM	0.021
Tretinoin	retinoic acid, binds retinoic acid receptor and Pin1 ligand	TRE	0.127
Pravastatin	Statin, HMG-CoA reductase inhibitor	STAT	0.425
Loperamide	Opioid, binds opioid-receptor agonist	OPID	0.026
Ergotamine	neurotransmitter analog, binds 5-hydroxytryptamine receptors type 1-8	NTA	0.055

The determined CC_{50} concentrations were all in the low mM range. Relatively large classes were obtained upon classification according to the global MoA of the employed drugs, such as the tubulin (de)polymerization inhibitors (class TUB; composed of combretastatin, paclitaxel, vinblastine, and colchicine) compared to other classes that consisted of only one drug (loperamide, class OPID). This was due to the exploratory design of the study, which initially did not take into account the relative size of the drug classes. The main aim of this

study was to include a diverse selection of drugs to explore and evaluate the overall assay performance. After exposing HeLa cells overnight to the drugs at the determined CC_{50}, mass spectra were recorded. Following mass spectral acquisition, peaks were aligned to five tentatively identified consistently observed reference peaks, listed in Table 32.

Table 32. Reference peaks used for spectra alignment during spectral processing of HeLa data set. Listed is the respective protein name, second column lists corresponding UniProtKB accession number; third column lists the theoretical m/z value, followed by the observed m/z value in the fourth column. Fifth column lists absolute mass error in ppm. Last column shows theoretically calculated isoelectric point (pI). Inset on the right shows average mass spectrum of untreated HeLa cells with asterisk (*) indicating reference peaks.

Name, notes	UniprotKB	Theoretical m/z	Observed m/z	Error (ppm)	pI
Minor histocompatibility protein HB-1[a]	O97980	4939.5	4939.0	100	4.8
Minor histocompatibility protein HB-1	O97980	4965.5	4966.2	128	5.0
metallothionein-2[b]	P02795	6085.2	6085.6	66	8.2
Ribosomal 40S S30	P62861	6648.9	6650.1	193	12.3
Ubiquitin[c]	P0CG47	8565.9	8565.2	76	6.5

[a] suspected natural variant (Y→H) or PTM of O97980
[b] acetylated
[c] maturated monomer, position 77-152
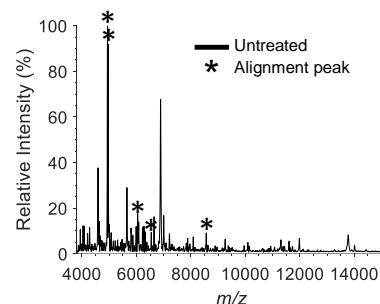
Unlike the other assayed organisms, not all major peaks were identified as ribosomal associated proteins with a relatively high pI. Two of the most abundant peaks were observed just below m/z 5000, at m/z 4939.0 and m/z 4966.2. The observation of the major peak at m/z 4966.2 is in agreement with observations by other researchers investigating human cells, although the peak at m/z 4939.0 was not reported in their papers [137, 229, 230]. These peaks were tentatively identified as minor histocompatibility protein HB-1, and a corresponding isoform. In addition to the minor histocompatibility proteins, a metallothionein protein, a ribosomal protein, and ubiquitin were used for alignment of the mass spectra. Only the one ribosomal associated protein in this alignment set does have a relatively high pI of 12.3, consistent with observed ribosomal peaks from the other assayed organisms. The metallothionein protein also has a relatively high pI of 8.2, but this was not the case for the major peaks belonging to histocompatibility proteins HB-1, with a pI of 4.8-5.0. The absolute mass error of the peaks after spectral alignment was considered good, being below 300 ppm.

After spectral alignment, the aggregated feature sets for the binary and MoA classification problem were determined using the feature selection algorithms. Details of the feature selection by RF, SFS, and SBS are provided in Appendix Figure 10 and Appendix Figure 11 for the binary and MoA classification problem, respectively.

4.4.1.2 Binary model

The aggregated feature selection based on the binary classification results in a feature set containing only two peaks, fewer peaks than in the aggregated feature sets of other for any of the other assayed organisms. The selection of only two peaks is presumably due the highly unbalanced data set, as only 9 out of the 155 spectra (5.8%) originated from untreated cells. Especially the RF algorithm suffers from the extreme bias in such cases, as the a priori chances of correctly assigning the class 'treated' is already 94.2%. In this case, it resulted in only 4 peaks above the feature importance threshold value by the RF (see Appendix Figure 10). Likewise, the forward feature selection algorithm suffered from the imbalance and selected few peaks. Details of the two peaks selected for the binary model are depicted in Figure 19.
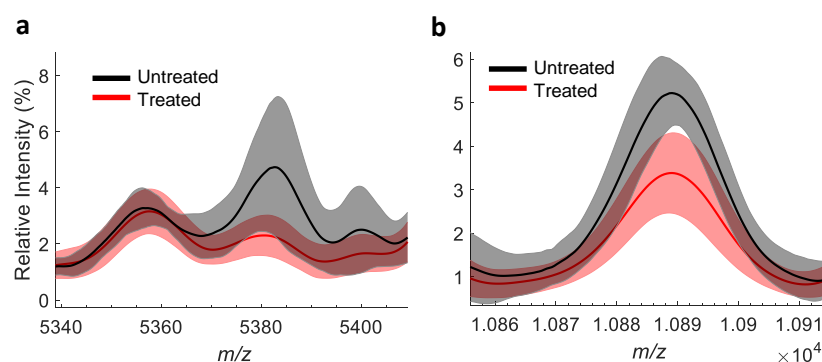

Figure 19. Mass spectral details from HeLa cells. (a) Details of peak at m/z 5382.8. Depicted are average mass spectra of untreated cells (black) and treated cells (red), mean absolute deviation (MAD) is indicated with shades. (b) Shows details of peak at m/z 10888.9, colored as described for (a).

The unidentified peak selected for the binary model observed at m/z 5382.8 shown in Figure 19a was selected by all three feature selection algorithms. The peak allowed for a good distinction between the two classes, as the intensity decreased from 4.7% ± 2.5 for untreated cells to 2.2% ± 0.7 relative intensity upon treatment with drugs. In addition to this peak, the peak at m/z 10888.9 was selected, shown in Figure 19b. The peak was tentatively identified as protein NCBP2AS2 (Q69YL0; theoretical m/z 11985.0, relative mass error 69 ppm, theoretical pI 12.0). This protein, also known as hypoxia-induced angiogenesis regulator (HIAR), was previously reported by a proteomic study of cancer-associated fibroblasts [231]. There it was found that this protein was induced as a response to hypoxic stress. Interestingly, Figure 19b shows a decrease in abundance of NCBP2AS2 for spectra obtained with treated (stressed) cells, whereas it was shown in literature that the protein NCBP2AS2 was upregulated by hypoxic stress. The peak at m/z 10888.9 decreased almost a factor two in intensity, from 5.2% ± 0.8 relative intensity to 3.4% ± 0.9 upon treatment with

drugs. The selection of this protein as a response to drug-induces stresses suggests that the protein may be involved in more than just hypoxic stress, and is possibly a more general stress-associated protein.

Using the two selected peaks in the aggregated feature, a Q-SVM model was trained and evaluated. The extreme class imbalance of the binary problem makes the relevant application and interpretation of the constructed binary model limited. Nevertheless, the results of the internal validation performed in this work serve to illustrate that the developed MS-based screening assay can be –in principle– applied to HeLa cells. The results of the binary model are shown in Table 33.

Table 33. Confusion matrix of the 10-fold cross-validation of binary quadratic support vector machine model of HeLa encompassing 155 mass spectra using the two peaks in the aggregated feature set. Indicated is the total number of spectra per class and the corresponding recall and precision value per class, and the overall accuracy in the bottom right in bold.

	Class labels	Treated	Untreated	Total	Recall
		Model classification			
True class	Treated	144	2	146	0.99
	Untreated	6	3	9	0.33
	Total	150	5	155	
	Precision	0.96	0.60		**0.95**

Table 33 shows an overall mean accuracy of 0.95 for the binary model, which is comparable to the binary models of other assayed organisms. However, the indicated performance is largely an effect of the large class imbalance towards the class of treated cells. Arbitrarily classifying all spectra to the class treated would yield an overall accuracy of 0.94, almost equal to the current classifier performance. Due to the class imbalance, the binary model is properly trained to recognize treated sample mass spectra, but can hardly detect untreated cells' spectra. This is illustrated by the high recall and precision of the model for identifying treated HeLa cell spectra, regardless of the drug compound (recall 0.99 and precision 0.96). Contrarily, the precision and recall for the class untreated is low (0.60 and 0.33 respectively). Due to the class imbalance and lack of external validation of the model, the practical implications of this model should be improved by balanced experimental design. Nevertheless, the results illustrate the concept of the MALDI-TOF MS method for HeLa cells.

4.4.1.3   MoA model

For the MoA classification problem, features were evaluated using RF, SFS, and SBS (see Appendix Figure 11), to create the aggregated feature set. In total, seven peaks were included in the aggregated feature set. Five of these seven peaks were tentatively identified. Details of the peaks are listed in Table 34.

Table 34. Aggregated feature set of peaks selected from HeLa spectra for the MoA model. Listed is the observed m/z value and the theoretical m/z value of the protein, if identified. For identified proteins is indicated the absolute relative mass error in ppm, UniProt accession number, theoretical isoelectric point (pI), and the corresponding name and notes of the protein, next to post-translational modifications (PTMs).

Observed m/z	Theoretical m/z	Error (ppm)	UniProtKB	pI	Name; notes, PTMs
4283.5	-	-	-	-	-
4966.2	4965.5	128	O97980	5.0	Minor histocompatibility protein HB-1
6048.5	6049.1	92	P80297	8.3	Metallothionein-1X, oxidized
6085.6	6085.2	66	P02795	8.2	Metallothionein-2, acetylated
10638.8	-	-	-	-	-
10888.9	10891.6	252	Q69YL0	12.0	Protein NCBP2AS2, hypoxia induced cancer associated protein
11984.2	11985.0	69	Q13278	8.4	Putative protein RIG, molecular marker for tumor progression

Multiple peaks selected for the MoA model have an annotated function as being involved in stress-associated processes, among which metallothionein proteins and protein NCBP2AS2. The protein NCBP2AS2 was also selected for the binary classification problem, emphasizing its responsiveness to the drug-induces stresses. Additionally, the peak at m/z 11984.2 was identified as putative protein RIG. This protein is known to be involved in malignant progression of glioblastomas [232]. The identification of the peak at m/z 11984.2 as protein RIG (a known glioblastoma biomarker) is ambiguous, as its expression has so far only been shown in brain, heart, and lung tissue [232]. It might of course be that the observed peak at m/z 11984.2 belongs to a different protein, which is not necessarily annotated in the UniProt database. The three feature selection methods found the peaks with the most predictive power were the metallothioneins, found at m/z 6048.5 and 6085.6. The metallothioneins are a type of small, cysteine rich, stress responsive proteins [233]. Details of these peaks are shown in Figure 20.
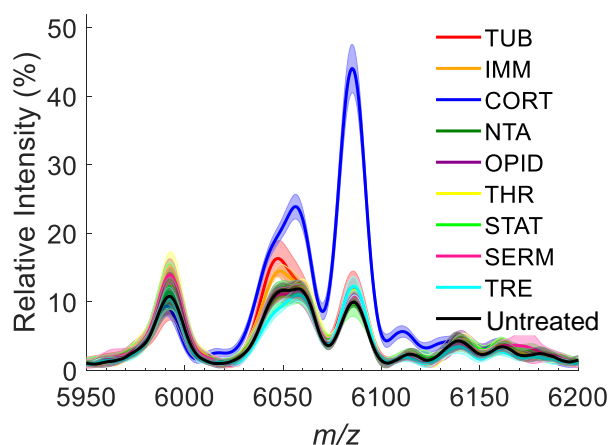
Figure 20. Mass spectral details of HeLa cells. Shown are details of peaks selected at m/z 6048.5 and m/z 6085.6. Depicted are average spectra (solid line) ± the MAD (shaded area). Spectra are colored according to drug class treatment as follows. Red: tubulin (de)-polymerization inhibitors (TUB); orange: Immunosuppressant (IMM); blue: corticosteroids (CORT); green: neurotransmitter analog (NTA); dark magenta: opioid receptor agonist (OPID); yellow: thyroid hormone (THR); lime: statins (STAT); pink: selective estrogen receptor modulator (SERM); cyan: tretinoin (TRE); black: untreated cells.

Metallothioneins are cysteine-rich, low-molecular weight proteins, known to interact with, as well as being transcriptionally regulated by, heavy metals (first described in 1957 [234]) and corticosteroids [233]. The increase of the relative abundance of metallothioneins in HeLa cells upon treatment with the corticosteroid dexamethasone had already been described in 1979 by Karin and Herschman [235]. Later it was established that the (up)regulation of metallothioneins is a more general response towards corticosteroids, and other types of stress, and is involved in apoptotic pathways [233, 236, 237]. This strong regulatory effect of corticosteroids on metallothioneins is in agreement with a 4-fold increase in abundance for peak observed at m/z 6085.6 (see Figure 20) upon treatment with the class CORT (composed of prednisolone and dexamethasone 21-phosphate). The intensity of the peak increases significantly to 44.0% ± 3.5 upon treatment with the corticosteroid drugs compared to the other drug treatments (on average 11.1% ± 1.2) and untreated cells (intensity 10% ± 0.6).

One might expect that the peak observed at m/z 6057.2 in Figure 20 (another suspected metallothionein) would also be selected for modelling, as it is also quite responsive to the steroid drugs, like the peaks at m/z 6048.5 and m/z 6085.6. The reason why this peak at m/z 6057.2 was not selected for the aggregated feature set may lie in the fact that it cannot provide additional information to the distinction of the corticosteroids captured in the peak at m/z 6085.6. The peak at m/z 6048.5 (identified as metallothionein-1X), does provide additional information. Not only did this peak respond significantly to the corticosteroid treatment (CORT; 20.3% ± 1.3), but it also responded to tubulin (de-)polymerization

109

inhibitors (TUB; 16.2% ±2.7) and immunosuppressing drugs (IMM; 14.5% ± 0.9 percent point) compared to the other drug treatments (on average 10.8% ± 1.2) and untreated cells (10.0% ± 0.6). This specific metallothionein is reportedly involved in apoptotic signaling in response to cisplatin, an anticancer drug which causes DNA damage [238].

The detection of multiple, stress-associated proteins shows that the aggregated feature selection method applied to HeLa mass spectra is able to detect relevant proteins in response to various drug treatment. Using the aggregated feature set, a MoA classification model was trained. The classification results of the MoA model are shown in Table 35 as a confusion matrix.

Table 35. Confusion matrix of the 10-fold cross-validation of MoA quadratic support vector machine model using the aggregated feature set of HeLa exposed to drugs. Class abbreviations are as follows: CORT: corticosteroids, IMM: immunosuppressant; NTA: neurotransmitter agonist, OPID: opioid, SERM: selective estrogen-receptor modulator, STAT: statin, THR: thyroid hormone, TRE: tretinoin, TUB: tubulin (de)polymerization inhibitor, UNT: untreated. Indicated is the total number of spectra per class, the corresponding recall and precision value per class, and the overall accuracy in the bottom right in bold.

					Model classification							
Class labels	CORT	IMM	NTA	OPID	SERM	STAT	THR	TRE	TUB	UNT	Total	Recall
CORT	22	0	0	0	0	0	0	0	1	0	23	0.96
IMM	0	9	2	0	0	1	0	0	0	0	12	0.75
NTA	0	1	5	3	1	0	1	0	0	1	12	0.42
OPID	0	0	2	3	4	3	0	0	0	0	12	0.25
SERM	0	0	3	2	5	0	2	0	0	0	12	0.42
STAT	0	0	0	5	1	3	2	0	0	0	11	0.27
THR	0	0	1	2	4	0	5	0	0	0	12	0.42
TRE	0	0	1	0	0	0	0	5	0	3	9	0.56
TUB	0	0	1	0	0	0	0	0	42	0	43	0.98
UNT	0	0	3	1	0	0	0	1	0	4	9	0.44
Total	22	10	18	16	15	7	10	6	43	8	155	
Precision	1.00	0.90	0.28	0.19	0.33	0.43	0.50	0.83	0.98	0.50		0.66

(True class on vertical axis)

Table 35 shows relatively high recall and precision values for several classes, as is the case for the corticosteroids (CORT; dexamethasone and prednisolone), the group of tubulin ligands (TUB; paclitaxel, combretastatin, colchicine and vinblastine), and, to lesser extent, the class immunosuppresses (IMM; cyclosporine) and tretinoin (TRE). Some of the other assayed drug classes, particularly L-thyroxine (THR), loperamide (OPID), tamoxifen (SERM), pravastatin (STAT), and ergotamine (NTA) show fewer distinct alterations in their respective mass spectra. From this first group of drugs (CORT, TUB, IMM and TRE), it is expected that they have a strong effect on the HeLa cells, as the classes of TUB and TRE are composed of specific anti-cancer drugs, intended to cause cell death. Additionally, the class IMM, composed of cyclosporine, is known to cause specific drug-induced superoxide mediated

cell damage in HeLa cells [239]. For the class of CORT it was expected that they would be classified correctly, as the spectra of HeLa cells treated with the corticosteroid drugs had shown to provoke such a specific and strong response in several selected peaks belonging to metallothioneins (see Figure 20). The other drugs (THR, OPID, SERM, STAT, and NTA), are not particularly known to be anticancer drugs and cause specific, intentional damage, except the class SERM (used as anti-cancer medicine [240]). The drugs of the class THR, OPID, STAT, and NTA do all have reported regulatory functions [241-244]. A partial reason for the non-distinctive proteomic response in this second group of drugs lies in the expression level of their respective target receptor. The lack of a specific response for the class SERM (composed of tamoxifen) can be explained by the fact that HeLa cells are naturally estrogen-receptor negative [245]. In a similar way, the spectra from cells treated with loperamide may not yield a distinct reaction, as the expression levels of its respective target receptor protein, the opioid receptor, is low to even absent in HeLa cells (originally an epithelial adenocarcinoma) [246]. The same is true for cells treated with ergotamine. Ergotamine mainly binds to the 5-HT receptors, which are mostly located in parts of the brain and vascular smooth muscles [247]. Therefore, a specific effect from HeLa cells was not expected. As a consequence, a correct classification is limited for those non-specific stressors and they are confused with each other by the model. However, the lack of respective target receptor is not an issue for some of the other drugs with poor classification performance (among which L-thyroxine, pravastatin). For these drugs, the respective target receptors are present in HeLa cells, thus their poor performance is likely due to a non-distinctive proteomic response. Consequently, these drugs are confused by the MoA model. However, since all drugs were all dosed at their relative CC_{50}, there should be a (partially lethal) response. The response signatures of the HeLa cells to these non-specific stressors are still distinct enough to separate them to some degree from the untreated cells.

4.4.2   Physical and chemical stress

In addition to the exploratory analysis of the assay on HeLa cells treated with a variety of drugs, the effects of different environmental stresses has been surveyed. This was done to investigate whether the proteomic changes that would be visible in MALDI-TOF mass spectra would be sufficient to distinguish cells based on the type of physical and physiochemical stress. Cells were treated with two drugs at their CC_{50} which have a different MoA, namely ergotamine (neurotransmitter analog; class NTA) and cyclosporine (Immunosuppressant, class IMM). These drugs were selected as they had shown to be reasonably distinguishable from untreated HeLa cells in the previous experiment. In addition, cells were treated with physical stressors that in this context have been labelled as two different MoAs: UV light exposure for several minutes and thermal stress for one hour

at 43 °C. After exposure to these stressors, mass spectra were recorded as described in the Experimental chapter.

Mass spectra were aligned to the same set of reference peaks as described in the previous subchapter (details are provided in Appendix Table 4). Peak error remained within 300 ppm for all reference alignment peaks. Subsequently, peaks were evaluated using RF, SFS, and SBS for both the binary and MoA classification problem, of which details are provided in Appendix Figure 12 and Appendix Figure 13. Details of the aggregated feature sets and internal validation of both the binary and the MoA model will be discussed in the following sections.

4.4.2.1 Binary model

With the relatively well-balanced data set that was obtained by investigating physical and physicochemical stressors, more than 2 peaks were selected compared to the previously discussed binary feature set. Neither of the two peaks that were selected for the previous binary model, were selected for the current binary model. This is presumably an effect of the more balanced data set and the different types of stresses to which the cells were subjected. The peaks selected in the aggregated feature sets for the binary model are listed in Table 36.

Table 36. Aggregated feature set of peaks selected in HeLa mass spectra for the binary model stressed with chemical and physical stressors. Listed is the observed m/z value and the theoretical m/z value of the protein, if identified. For identified proteins is indicated the absolute relative mass error in ppm, UniProt accession number, theoretical isoelectric point (pI), and the corresponding name and notes of the protein, next to post-translational modifications (PTMs), if applicable. Details of peaks marked with asterisk (*) are provided in Figure 21.

Observed m/z	Theoretical m/z	Error (ppm)	ProtKB Accession	pI	Name, notes
4986.1	4983.9	439	A1L3X4	8.4	Putative metallothionein MT1DP
5804.4*	-	-	-	-	-
6058.3*	6057.2	189	P04732	8.4	Metallothionein-1E
6085.6*	6085.2	63	P02795	8.2	Metallothionin-2, acetylated
9956.1	-	-	-	-	-
11604.7	11602.5	193	K7EIQ3	9.0	Uncharacterized protein ZNF561-AS1

Although some of the stresses to which the cells were subjected in this experiment were of a different nature than the drugs discussed in the previous section, multiple metallothioneins were selected here again (m/z 4986.1, m/z 6085.5, and m/z 6085.6). The selection of metallothioneins is in line with literature, stating metallothioneins are involved in general stress responses, regardless of the exact underlying mechanism [236]. The

identification of metallothionein MT1DP (m/z 4986.1) is ambiguous, as its mass accuracy is beyond the acceptable error of 300 ppm. However, its function description (responsiveness to stress) and the absence of other proteins in the database within reasonable error around m/z 4986.1 make it a likely identification. Details of several peaks for selected the binary model are depicted in Figure 21.
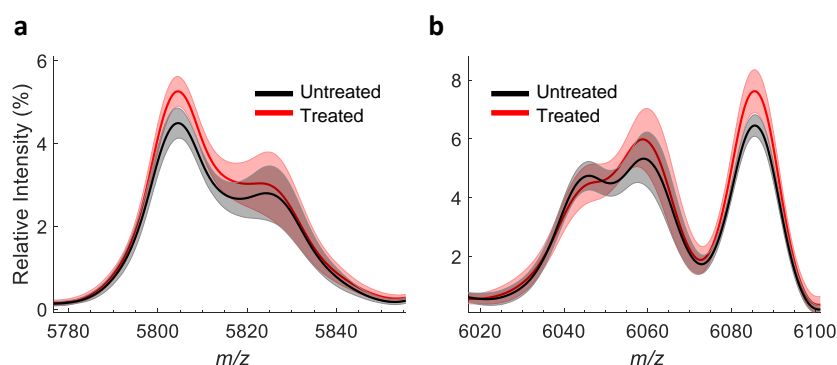

Figure 21. Mass spectral details from HeLa cells. (a) Details of peak at m/z 5804.4. In black is depicted the average intensity ± mean absolute deviation (MAD) in the shaded area of untreated cells' mass spectra. In red is depicted average intensity ± MAD of treated cells. (b) Details of peak at m/z 6058.6 and m/z 6085.6. Spectra colored as described for (a).

In Figure 21a, details of the unidentified peak at m/z 5804.4 are depicted, whose relative intensity increases from 4.5% ± 0.4 to 5.3% ± 0.4 upon being subjected to the stressors. The intensity of the metallothionein peaks depicted in Figure 21b at m/z 6058.3 and m/z 6085.6 both increased upon stressing the HeLa cells. The peak at m/z 6058.6 increases slightly from 5.3% ± 0.8 to 6.0% ± 0.9 when stressing the cells, while the peak at m/z 6085.6 increases significantly from 6.5% ± 0.4 to 7.6% ± 0.7 upon stressing the cells. Using the aggregated feature set, the binary Q-SVM model was trained. The internal validation results of the binary model are shown in the confusion matrix in Table 37.

Table 37. Confusion matrix of the 10-fold cross-validation of binary Quadratic support vector machine model with the aggregated feature set of HeLa cells, treated with a variety of stressors. Indicated is the total number of spectra per class and the corresponding recall and precision value per class, and the overall accuracy in the bottom right in bold.

		Model classification			
	Class labels	Treated	Untreated	Total	Recall
True class	Treated	147	4	151	0.97
	Untreated	3	39	42	0.93
	Total	150	43	193	
	Precision	0.98	0.91		**0.96**

The binary model trained with the aggregated feature set has a high overall performance of 0.96, classifying 186 out of the 193 spectra to the correct class. Although this data set also suffers from class imbalance, overall the recall and precision scores are in line with what was observed for the binary models of the assayed bacteria and yeasts. The class imbalance on the binary model still has its effects on the underrepresented class 'untreated', reflected in a lower recall and precision values of 0.93 and 0.91, respectively, when compared to the 'treated' class (0.97 and 0.98, respectively). Compared to the previously discussed organisms, the performance of the 'untreated' class is among the best, considering the spectra only make up 22% of the data.

4.4.2.2 MoA model

For the MoA model, seven peaks were included in the aggregated feature set. These peaks are listed in Table 38.

Table 38. Aggregated feature set of peaks selected in HeLa mass spectra for the mechanism of action (MoA) model stressed with chemical and physical stressors. Indicated is the observed and theoretical mass and respective absolute error in ppm of identified proteins. Protein accession number is listed in the fourth column, next to the theoretically calculated isoelectric point (pI). Last column lists protein name, and if applicable post translational modifications (PTMs) and notes. Details of peaks marked with asterisk (*) are provided in Figure 22.

Observed m/z	Theoretical m/z	Error (ppm)	UniProtKB	pI	Name, PTMs, notes
4284.7	4285.0	56	P0DPQ6	11.4	DT3UO_HUMAN DDIT3 upstream open reading frame protein; involved in apoptotic and autophagy regulation
4966.3	4965.5	150	O97980	5	Minor histocompatibility protein HB-1
6046.2*	6049.1	-477	P02795	8.2	Metallothionein-1X, oxidized, May be involved in FAM168A anti-apoptotic signaling
8565.6*	8565.9	27	P0CG47	6.5	Ubiquitin, position 77-152
9956.1	-	-	-	-	-
10795.5*	10793.4	197	O00453	8.4	Leukocyte-specific transcript 1 protein
11984.1	11985.0	69	Q13278	8.4	Putative protein RIG, molecular marker for tumor progression

In this particular feature set, 6 out of the 7 peaks were tentatively identified. The protein observed at m/z 4284.7 was identified as DDIT3 upstream open reading frame protein. The selection of this protein is in line with its functional annotation, as this protein is known to be involved in apoptotic signaling [248]. Additionally, this protein shows high similarity to DNA-damage-inducible transcript 3 protein (P35638, also known as CHOP), a multifunctional transcription factor which has an essential role in responses to a wide variety of cell stresses [249], underlining its stress-associated function. Two alignment peaks were selected for the aggregated feature set, namely the peak at m/z 4966.3, tentatively identified as minor

histocompatibility protein HB-1, and the alignment peak tentatively assigned to ubiquitin, observed at m/z 8565.6. Ubiquitin is a small protein which is involved in many cellular regulatory processes, among which responses to external and internal cellular stresses [250] and apoptotic signaling [251], emphasizing the ability of the feature selection algorithms to detect relevant stress-associated proteins. As was seen for the MoA model concerning solely drug response, the metallothionein 1X was selected here again. In this case, its centroid peak value was observed m/z 6046.2, although it was previously observed at m/z 6048.5. This small mass discrepancy is due to inherently limited mass resolution of the machine. Additionally, the peak at m/z 10795.5 was identified as leukocyte-specific transcript 1 protein. Contrary to what its name implies, this protein is widely expressed in a variety of tissues and not only limited to leukocyte cells [252], and has a possible role in modulating immune responses [253]. It is speculated that this peak was selected as its expression level is possibly influenced by cyclosporine, the immunomodulation drug in this data set. Details of metallothionein-1X, ubiquitin, and leukocyte-specific transcript 1 protein are provided in Figure 22.
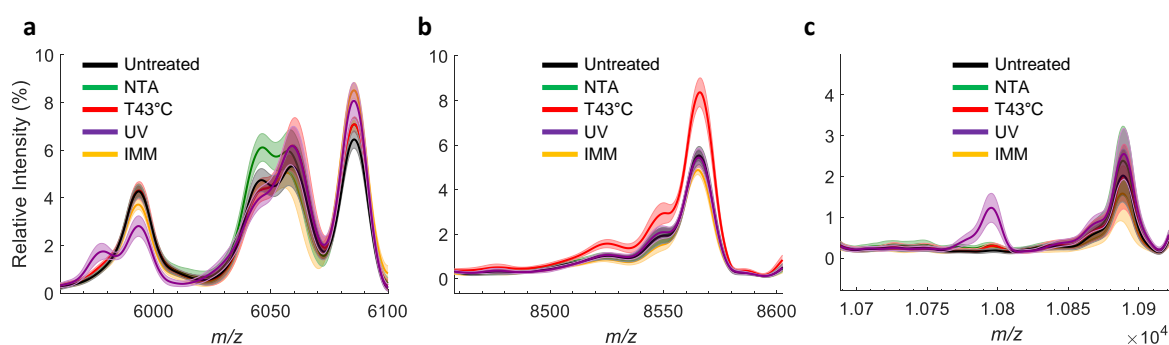

Figure 22. Details of peaks from HeLa, selected for the MoA model. Depicted in (a) is the peak at m/z 6046.2. Depicted are average mass spectra ± MAD colored as follows: black: untreated; green: treated with neurotransmitter analog (NTA) ergotamine; red: incubated at elevated temperature (T43°C); purple: treated with ultraviolet light (UV); and orange: treated with immunosuppressant (IMM) cyclosporine. In (b) selected peak observed at m/z 8565.6. Spectra are colored as described for (a). Depicted in (c) selected peak at m/z 10795.5 (Leukocyte-specific transcript 1 protein). Spectra are colored as described for (a).

The data in Figure 22 illustrate why these peaks were selected, as each of the depicted peaks gives a specific and clear separation from the other classes. The peak in Figure 22a at m/z 6046.2, which was tentatively identified as a metallothionein, is elevated to 6.1% ± 0.6 only when treated with ergotamine (the class NTA) compared to 4.4% ± 0.4 for the other classes, on average. This effect of the class NTA on this particular peak was not seen in the previous experiment which only involved drugs. There, the peak had not responded significantly to ergotamine (11.9% ± 1.1) compared to untreated cells (11.6% ± 1.1). This also illustrates the considerable day-to-day variation in the mass spectra, as the untreated

cells in this experiment have a relative intensity more than half (4.7% ± 0.5) of what they had in the previous experiment (11.6% ± 1.1). This also emphasizes the essential requirement of data-dependent feature selection for classification modeling, as relative peak intensity can change considerably between experiments.

The peak shown in Figure 22b (m/z 8565.6, tentatively identified as ubiquitin) strongly responds to the incubation at elevated temperature (intensity 8.4% ± 0.6), but is unaffected by treatment of the other classes (intensity 5.3% ± 0.3). This is in line with literature, which also describe the involvement of ubiquitin in heat-shock like stresses [254].

The peak in Figure 22c at m/z 10795.1, identified as leukocyte-specific transcript 1 protein, uniquely responds to UV treatment (intensity 1.2% ±0.2), but is practically absent in the other cases (intensity on average 0.3% ±0.1). This observation is contrary to what was expected, as the leukocyte-specific transcript 1 protein is known for its immunomodulatory involvement, but does not respond here to the immunomodulatory drug cyclosporine (class IMM).

Interestingly, in Figure 22a at m/z 5978.4, another peak which is uniquely present after incubation under UV light (purple) which is absent for all other treatments. However, this peak was not selected for the final aggregated feature set. Presumably, the peak would be redundant, as it would contain no additional information considering the peak at m/z 10795.1 in Figure 22c. Using the aggregated feature set, a multiclass quadratic support vector machine model was generated. Internal validation results per stressor are shown in Table 39.

Table 39. Confusion matrix of the 10-fold cross-validation of quadratic support vector machine model of the different stressors with the aggregated feature set of HeLa cells. Class abbreviations are as follows: IMM: immunosuppressant; NTA: neurotransmitter agonist; T43: incubation at 43° Celsius; UNT: untreated; UV: incubated under ultraviolet light. Indicated is the total number of spectra per class, the corresponding recall and precision value per class, and the overall accuracy in the bottom right in bold.

		Model classification						
	Class labels	IMM	NTA	T43	UNT	UV	Total	Recall
True class	IMM	18	0	0	1	0	19	0.95
	NTA	0	20	0	0	0	20	1.00
	T43	0	0	58	0	0	58	1.00
	UNT	0	0	1	41	0	42	0.98
	UV	0	0	0	0	54	54	1.00
	Total	18	20	59	42	54	193	
	Precision	1.00	1.00	0.98	0.98	1.00		**0.99**

The confusion matrix shows an overall accuracy of 0.99, which is higher than for the binary model constructed with the same data set, and even the highest overall accuracy described in this work. The performance is attributed to the different type of stressors (physiochemical and physical), which have unique effects on certain mass spectral peaks (see Figure 22). This causes the inter-class variation to be relatively wide, making it easier for the model to distinguish the respective proteomic responses. This supports a previously raised discussion point, where comparable inter-class variation was suggested as possible source of poor classification performance. The extensive inter-class variation and the resulting model performance during internal validation are also reflected by the relatively high recall and precision values, which are above 0.98 for all classes (except recall for the class IMM, which was still high at 0.95).

4.4.3   Summary

This last chapter of this thesis showed that the developed MALDI-TOF MS-based drug screening assay was also transferable to HeLa cell cultures subjected to a variety of stressors. The internal validation of models trained on mass spectra obtained with cell treated with several drugs shows promise, but requires further optimization to explore its full potential by generating a more balanced data set. In addition, the misclassification of non-distinctive stressors indicates that such drugs may not serve as the optimal training set for drug screening purposes.

The last part of this study showed how UV and temperature stress provoked specific proteomic alterations captured by specific peaks in the aggregated feature set, measured by MALDI-TOF MS. This highlights the method's versatile and adaptable nature. This study also illustrated the beneficial effects of high inter-class differences on the model accuracy. With the current results of this exploratory study, it was shown that not only drug-induced, but also physical stress could be distinguished from one another. This may serve as a starting point where more clinically relevant proteomic responses can be classified, such as the identification between different apoptotic pathways and necrosis.

5 Conclusion

Current literature reports suggest that target-based screening methods applied for antibiotic drug discovery has yielded a relatively low output. As a result, attention has shifted towards phenotypic screening approaches to fulfill the urgent unmet medical need for new antibiotic drugs. However, available phenotypic screening approaches such as macromolecular synthesis assays, cytological profiling, and microarrays use complex reagents and equipment, may require engineered bacterial strains, and use relative high screening concentration to detect a cellular drug responses. To bridge the gap between the current unmet medical need in antibiotic drug discovery and the limitations of available phenotypic screenings assays, it was aimed to develop a novel proteomics-based phenotypic screening approach. In this thesis is described a high-throughput, label-free, phenotypic cell-based assay using MALDI-TOF MS coupled to advanced machine learning strategies, which is able to detect sub-lethal stress in bacterial cell cultures induced by antibiotic drugs. The employed machine learning strategies also allow for phenotypic information extraction on the mechanism of action of the assayed compounds, one of the mayor limitations mentioned for target-based screening approaches. As the advantages of phenotypic drug-discovery are being more widely realized, the developed method was also investigated for eukaryote yeasts and human HeLa cells in response to drugs.

Several objectives were realized to establish this method. One of the objectives was to establish a high-throughput experimental workflow and to reduce experimental variation that is commonly present in mass spectral data. A standardized workflow was established by performing liquid handling procedures in 96-well and 384-well format by means of semi-automatic robotics. Experimental variation was minimized by synchronizing the bacterial cell division cycles, which resulted in reduced peak intensity fluctuations. Computational measures to minimize the influence of inherent MALDI-TOF MS experimental variations included the development of a custom computational workflow in the MATLAB programming environment. This computational workflow handled the import of the raw MALDI-TOF MS data and performed required pre-processing steps of the mass spectral data. These steps involved raw data import, baseline correction, normalization, smoothing, peak alignment, and peak detection.

A data analytical objective was to establish a data-dependent computational pipeline that would minimize user interference and could be operated independently of the assayed organism or drug type(s) investigated. Extraction of relevant mass spectral features was done by means of data-dependent feature selection, facilitated by defining selection thresholds based on the corresponding training data set and classification problem. To ensure robustness of the computational pipeline, different peak selection algorithms were applied to yield four different feature sets, which were coupled to nine different classification models for an *E. coli* data set. These combinations of feature sets and models

were subsequently trained for two different classification problems (binary and mechanism of action). The resulting 72 different models were evaluated based on internal and external validation accuracy. Model evaluation was performed using a data set of *E. coli* comprising over 900 MALDI-TOF MS mass spectra, from cells exposed to 17 different antibiotics with four different mechanisms of actions, at sub-lethal concentrations ranging $1\times$-$^1/_{32}\times$MIC. The evaluation of 72 models showed that an aggregated feature set, composed of features that were selected by a random forest of decision trees, and sequential forward and backward feature selection, in combination with a quadratic support vector machine model resulted in the best performance. Classifying mass spectra as treated or untreated resulted in an overall accuracy of 0.92 for internal validation and 0.95 for external validation. Classification based on the respective mechanism of action of the antibiotics resulted in a classification accuracy of 0.67 for internal validation and 0.80 for external validation. In-depth evaluation of the data-dependent feature selection method showed that the selected peaks in *E. coli* mass spectra included multiple known stress associated peaks. This underlined the ability of the computational pipeline to identify relevant features in the data set without prior knowledge.

A sub-aim of this work was to explore the assay's applicability beyond antibiotic drug screening. Therefore, after establishing the standardized experimental workflow in combination with the data-dependent computational pipeline for *E. coli*, the applicability and versatility of the screening method was demonstrated on data sets obtained from the Gram-positive bacterium *S. aureus*, the eukaryotic yeasts *S. cerevisiae* and *C. albicans*, and mammalian HeLa cells. A training set for each organism, exposed to a variety of drugs, was used to select features in a respective aggregated feature set, with which Q-SVM models were trained. As was seen for *E. coli*, the feature selection algorithms continued to select relevant peaks, some of which were identified as stress associated proteins. These peaks allowed the Q-SVM models to distinguish between treated and untreated mass spectra, as well as the distinction mass spectra treated with drugs with different mechanisms of action, all at sub-lethal concentrations of the employed drug. Internal validation for all organisms showed comparable performance to *E. coli*, with overall accuracies between 0.92 and 0.99 for the binary models and accuracies between 0.76 and 0.96 for MoA models. This showed that the developed MALDI-TOF MS assay and computational pipeline were readily transferable to a diverse range of organisms and responses to stressors.

A similarity between the data sets of the assayed organisms was the imbalance of the training data set, which resulted in recurring lower precision and recall values for minority classes. Careful experimental design in future projects should focus on eliminating class imbalance to further improve the classification performance of the assay. Nevertheless, the application of the developed method for organisms tested subsequent to *E. coli,* each showed several strengths of the classification models, and potential areas of improvement. For example, external validation of models trained for *S. aureus* showed that the screening

concentration is an experimental variable which needs to be carefully selected, as a high screening concentration may result in insufficient cell growth when cells are treated with potent drugs. This, in its turn, leads to unsatisfactory mass spectral signals that cannot be processed for analysis. Nevertheless, this observation underlines the assay's capability to detect proteomic responses at sub-minimal inhibitory concentrations, to identify weakly active drugs.

The data set for *S. aureus* that was subsequently produced with exclusion of the lowest screening concentrations ($^1/_{16}\times$ and $^1/_{32}\times$MIC) showed that removing class imbalance and inter- and intra-class variability can significantly improve model accuracy. Another important assay characteristic which was highlighted by the *S. aureus* data was the identification of a drug compound with a target protein that was not included in the training set. Here, the classification model was able to correctly classify fusidic acid, a steroid antibiotic inhibiting elongation factor G, as a protein synthesis inhibiting antibiotic. This is noteworthy, as the model was not trained with inhibitors specifically targeting elongation factor G. This demonstrates that the developed assay is capable of returning drug hits with similar mechanisms of action, even though the model was not specifically trained to recognize the exact response of that target site.

The transfer of the assay to the yeast *S. cerevisiae* showed the applicability of the method stretches beyond the prokaryotic domain. An important finding of the external validation of the binary model trained with *S. cerevisiae* data was the detection of antifungal activity of a drug with a mechanism of action which was completely absent from the training data set. This is a result of utmost importance, as it indicates that the developed methodology is able to find drugs with novel mechanisms of action when employing the binary class definition.

Even though external validation was not undertaken, experiments performed using *C. albicans* confirmed that the training set composition can significantly influence classification performance, as including only 1×, ½×, and ¼×MIC spectra in the training set led to internal validation accuracies of 0.95 for both the binary and the MoA model. This was in line with observations made based on the *S. cerevisiae* data set. The results for both yeast data sets showed that some drugs, although having dissimilar mechanisms of action, resulted in an overall similar proteomic response. In those instances, the model could not classify these drugs with high accuracy. This was specifically observed for the sterol biosynthesis inhibitors, which were mainly confused with cell wall synthesis inhibitors in the case of *C. albicans*. This raised the discussion on the importance of class division of drug compounds to train classification models. This topic could be covered in future work, where classification models might benefit from additional (un)supervised machine learning approaches for different class divisions, depending on which drugs are used in the training sets.

Lastly, the screening performed with HeLa cells confirmed the transferability of the developed assay to mammalian cells. In this proof-of-concept study, the screened drugs did not only include specific anti-cancer drugs but also hormones and immunomodulation drugs, among others. It was shown that several types of drugs cause specific proteomic MALDI-TOF MS signatures in HeLa cells (such as corticosteroids and tubulin polymerization inhibitors), while others did not (statins, neurotransmitter antagonists, opioids). This suggests that rational consideration should be taken when investigating certain types of drugs using the MALDI-TOF MS assay, as their distinction from untreated cells and each other can be limiting. In addition, the detection of the proteomic response of HeLa cells as a result of UV and thermal stress showed promising results of the assay's applicability beyond drug screening capabilities, such as the distinction between apoptosis and necrosis. Additional studies should be performed to explore the full potential of the developed assay for such specific applications.

As a response to the urgent need for a phenotypic screening assay that aids the search for new antibiotic drugs, this thesis has provided a high-throughput compatible, label free, cell-based screening assay that is capable of measuring sub-lethal drug effects in a pharmacological relevant setting. The assay's versatile, adaptable, and data-dependent characteristics make it suitable for whole-cell screening of potential drug compounds libraries for a variety of cells and drug types. Moreover, the ability to detect existing, but also new mechanisms of action of screened drugs is a highly sought-after characteristic, as this information can be used as a starting point for further target elucidation or to prioritize hits based on the detected MoA. The adaptability to multiple organisms and different types of cellular stress opens up a new chapter for the applications of proteomic profiling using MALDI-TOF MS.

6 Outlook

In this thesis, a framework is described which can analyze MALDI-TOF mass spectral data of cell cultures to identify (drug) stress responsive peaks in the proteome. Classification models were trained with the responsive mass spectral peaks to identify unknown (drug) stress responses based on a similar proteomic profiles.

For the purpose of drug screening, it was shown that binary models were able to accurately classify mass spectra to the class of either treated or untreated, and multiclass mechanism of action models were able to classify mass spectra to defined (drug) stress classes. To exploit the classification models even further, it would be interesting for future work to consider a two-step classification sequence. First, the binary model would identify active drugs, and subsequently, a mechanism of action model would identify the mechanism of action. This makes the mechanism of action classification problem inherently less complex, as one class (the class of untreated) could be removed from this classification problem. Such a two-step classification approach would most likely increase the overall accuracy of the method, as well as the precision and recall values for individual classes. It would also be interesting to investigate whether one could add a third level in this proposed classification sequence. In this step, one can attempt the identification of antibiotic differences within a MoA class, such as the difference between 50S and 30S ribosomal binding antibiotics within the class of protein synthesis inhibitors.

The work described in this thesis evaluated approximately 100 to 200 peaks for modeling purposes, depending on assayed organism, experimental settings, and applied stressors. Typically, in the order of only 10 peaks were selected and then used for the classification models. Both peak and model evaluation showed that these selected peaks contain relevant information that is significantly distinct to discriminate between several different proteomic responses. However, the overall information content of the mass spectra could be extended in future research for further improvement of the model's discriminatory power. A relatively simple way to expand the feature set under with the current experimental workflow is to widen the measured m/z range, especially in the lower (m/z <4000 range). Although mass spectra get progressively noisier in the lower m/z region under current settings and with the employed matrix, it could be of interest to investigate which peaks are selected below m/z 4000 and whether these benefit the overall classification performance. A second experimental modification that could be undertaken to expand the feature set, could lie the choice of matrix. For example, one could use 2,5-dihydroxyacetophenone or sinapinc acid as matrix, as both these matrices are known to produce ions of larger proteins in the range of 8-100 kDa. Another relatively straightforward experimental adjustment that could be made to obtain additional features from the same samples is to measure the whole-cell samples not only in positive-ion mode, but also in negative-ion mode. Changing the charge mode of the mass spectrometer cause will cause a different (degree of) ionization of the desorbed

proteins. As described in this work, with the current settings most highly ionizable proteins in positive-ion mode are ribosomal proteins with an isoelectric point above 9.0. In negative mode, (other) proteins would be ionized to a different degree, potentially complementing the set of peaks measured in positive mode.

Implementing only one of these alterations to the assay may already significantly increase the number of features available for subsequent feature evaluation procedures. Although gathering additional peaks for feature evaluation would intuitively yield a better classification performance, the features do not necessarily add complementary discriminatory information. Upon implementation of additional features, the feature selection methods and data-dependent selection criteria and thresholds should also be closely re-evaluated in order to prevent overfitting and poor generalization of the models.

Future work could also explore different feature selection criteria, or different feature selection and evaluation approaches. For example, the current algorithm for the construction of the random forest could be optimized to deal with the recurring class imbalance and can be tuned for potentially larger feature sets. It may also be considered to use a different feature selection algorithm than sequential feature selection, as it was found to be relatively computationally intensive. An interesting alternative would be LASSO (least absolute shrinkage and selection operator) or elastic net regularization to select features, for which several MATLAB functions and infrastructures are readily available. These algorithms are of specific interest as it has been applied for the purpose of classification of proteomic and genomic data in the past.

As discussed throughout this thesis, data set composition is a crucial point for both feature selection algorithms and modelling. The class imbalances observed in the employed data sets have shown to adversely influence the minority classes. Future work should carefully consider the drug stressor screening space to include proteomic responses from each class, while also producing a sufficient amount of untreated cell samples to balance the data set. The amount of untreated samples is of particular interest when a binary model is trained. In addition, one should carefully consider the members of each class, in order to avoid diffuse and diverse classes such as the class 'other', as was the case for the assayed bacteria in this thesis. As mentioned for the experiments performed on the yeast strains, one could also investigate the class division and composition of a data set before model training by means of unsupervised learning techniques. Such an approach may prevent a class division which yields highly similar classes, as was seen for the membrane and cell wall interfering antifungal drugs.

Several peaks selected for modelling were tentatively identified as stress associated peaks using the TagIdent tool. Although this protein identification tool provided valuable information, the results should be further validated. This could be done by screening mutant or deletion strains of each of identified peaks, to confirm their involvement in the cellular

drug response. To reduce the amount of possible database matches based on the observed m/z alone, information on the isoelectric point could be incorporated. This can be done using techniques such as liquid-phase isoelectric focusing or 2D gel electrophoresis. Alternatively, one could implement multiplexed LC-MS/MS experiments and database matching on tryptic digested protein fractions to shed more light on the identity of the observed proteins.

The ability to detect a variety of specific phenotypic stress responses on a cellular level is not only interesting in the field of drug discovery but also for the neighboring field of drug repurposing. For drug repurposing studies, the use of a phenotypic assay has the potential for fast drug development, as the exact target protein involved can remain unknown for a drug that is already FDA approved. Similarly, repurposing screenings with the developed assay might assist the identification of novel targets. Identified lead compounds may then be used for further target elucidation.

The experiments on HeLa cells using UV and temperature as stresses illustrated how the method may reach even further beyond the field of drug discovery, and indicate that the method may also be applicable to monitor the general state of cell systems. This aligns well with the continuing implementation of mass spectrometry as a standard analytical technique in multiple fields. For example, the combination of whole-cell proteomic responses and machine learning could be applied for in-line process analytical technology setups. In such a setup, one can monitor the cells' state in industrial fermentation processes such as the production of foodstuffs or the (fed-)batch production of recombinant biotechnological and pharmaceutical products using microorganisms.

Acknowledgements

First, and foremost, I would like to thank Prof. Dr. Klein for the space to conduct my Ph.D. research.

I would also like to thank Heiko Rudy for assisting me with MALDI-TOF experiments, and I would like to thank Richa Garg and Severin Kämmerer for their assistance in performing experiments of which data is shown in this thesis.

Last, but certainly not least, I would like to thank Marieke Klijn for all the discussions and careful editing of my thesis.
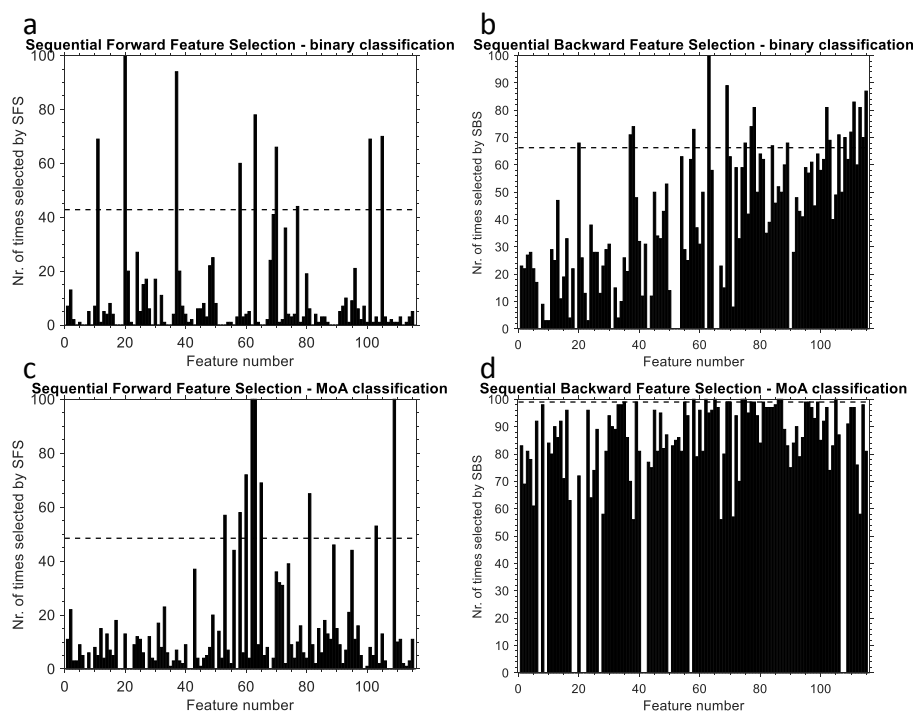
7 Appendices

7.1 Appendix Figures
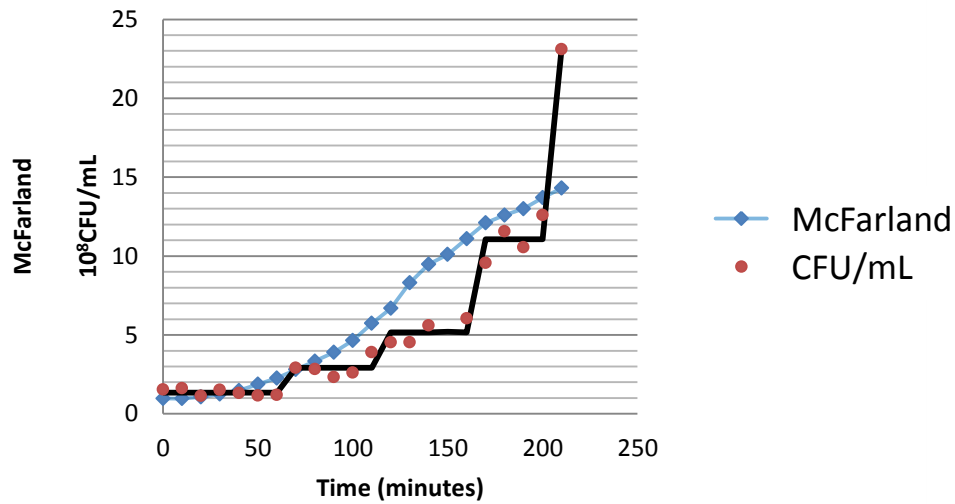
Appendix Figure 1. Synchronization of *E. coli* cell division. After starvation in nutrient limiting phosphate buffered saline solution and diluted to a McFarland standard of 1.0 while being resupplied with fresh Mueller-Hinton medium, after which they undergo synchronized division cycles. This synchronization is indicated by the doubling of the colony forming units per milliliter (CFU/mL, in red). This effect of synchronization is directly apparent by measuring only the cell turbidity using McFarland standards (blue).
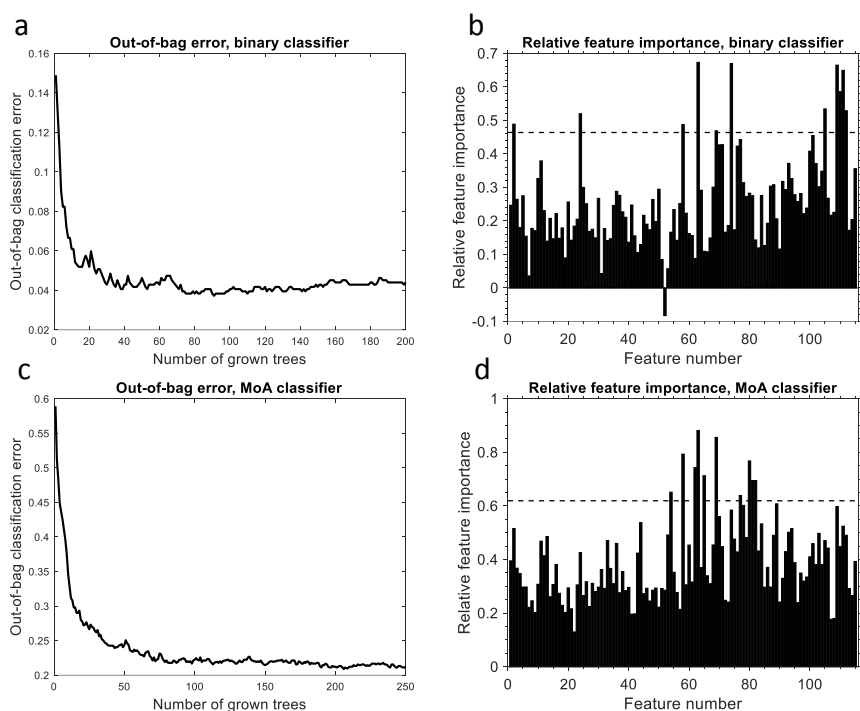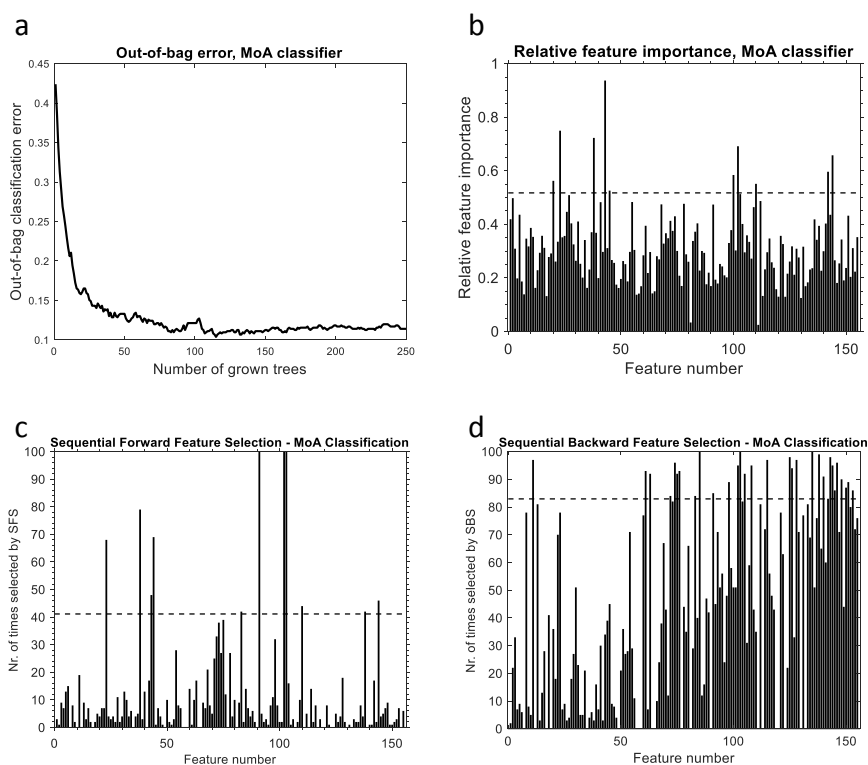
Appendix Figure 2. Feature selection using Random Forest (RF) on *S. aureus* data (dataset validated screen at 10 μM). Exemplary data showing (a) the elbow plot of the out-of-bag error for 200 decision trees for the binary classifying trees. Depicted in (b) is the relative feature importance of each of the 175 peaks in the mass spectrum of *S. aureus* for the binary classification problem using 200 decision trees. Horizontal dotted line shows the feature selection threshold (mean feature importance + 1.5 × feature importance standard deviation). Depicted in (c) is the elbow plot of the out-of-bag error for 250 decision trees for the mechanism of action (MoA) classifying trees. Shown in (d) is the relative feature importance of each of the 175 peaks in the mass spectrum of *S. aureus* for the MoA classifying trees using 250 decision trees.
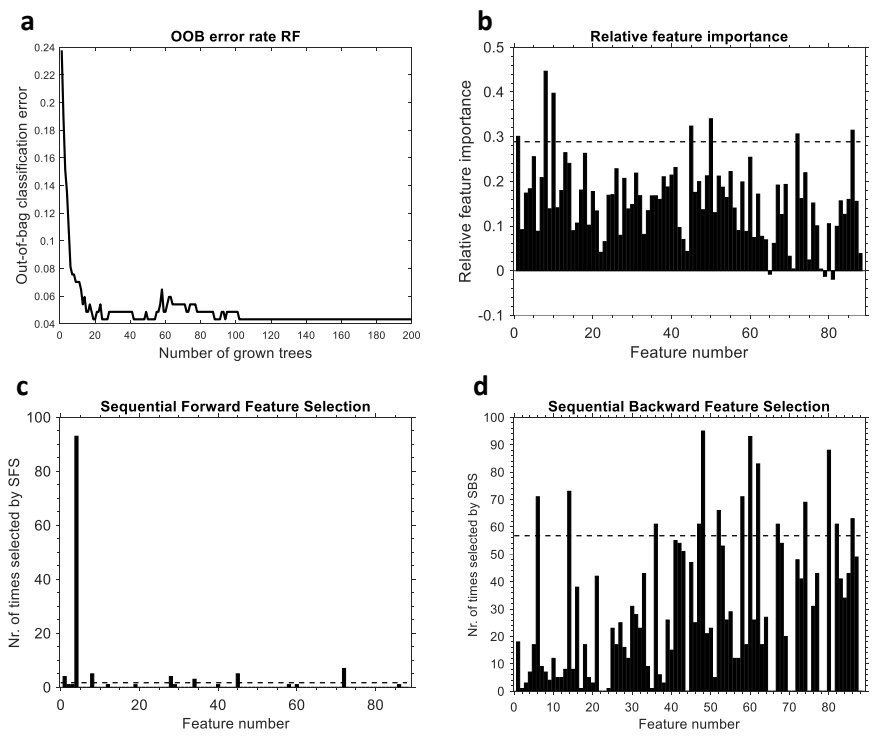
Appendix Figure 3. Feature selection using sequential forward and backward selection (SFS and SBS) of *S. aureus* data (screen at 10 µM). Exemplary data showing (a) how frequently peaks were selected by SFS for the binary classification problem on *S. aureus* data. Horizontal dotted line shows selection threshold. (b) Shows how frequently peaks were selected by SBS for the binary classification problem. Horizontal dotted line shows selection threshold. (c) Shows often peaks were selected by SFS for the multiclass mechanism of action (MoA) classification problem. Horizontal dotted line shows selection threshold. (d) Shows how often peaks were selected by SBS for the multiclass MoA classification problem. Horizontal dotted line shows selection threshold.
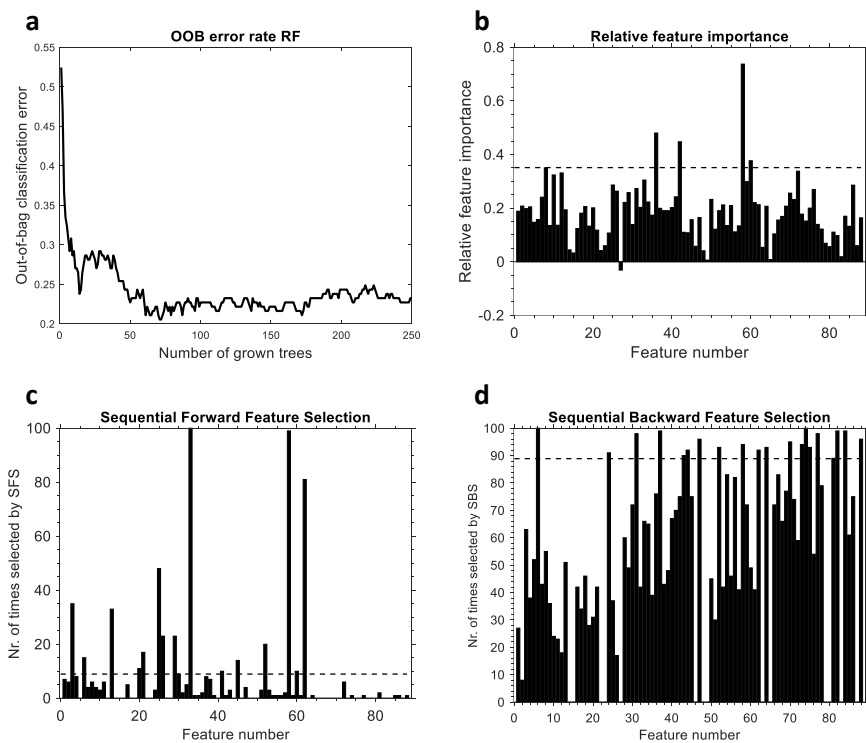
131
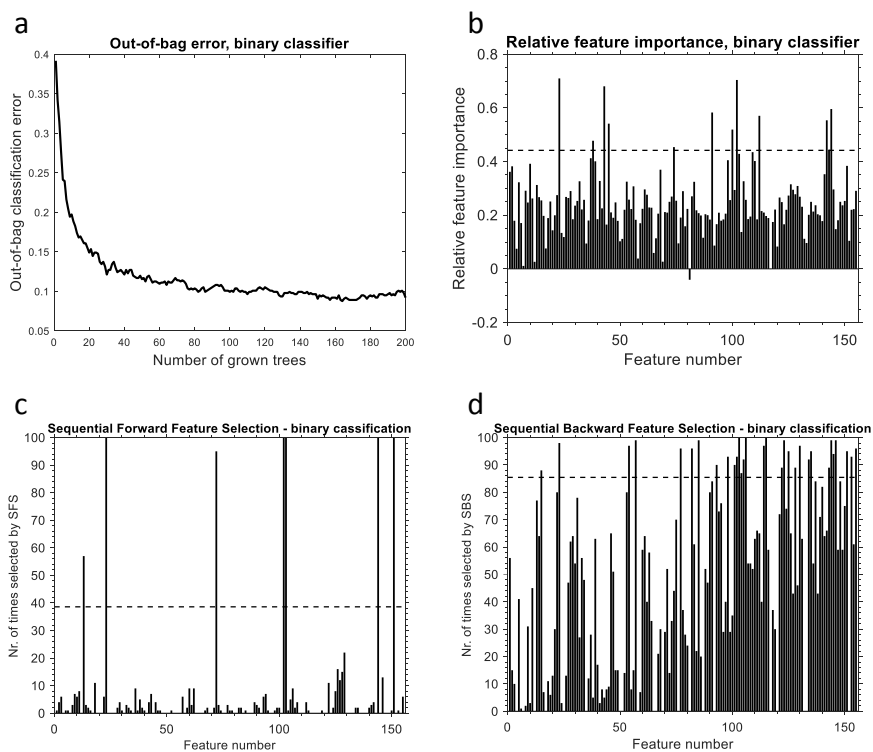
Appendix Figure 4. Feature selection for binary classification problem of *S. aureus* data (screen at 1 μM) using random forest, sequential forward and backward selection (SFS and SBS). Depicted in (a) the elbow plot of the out-of-bag error for 200 decision trees for the binary classifying trees. Depicted in (b) is the relative feature importance of each of the peaks in the mass spectrum of *S. aureus* for the binary classification problem using 200 decision trees. Horizontal dotted line shows the feature selection threshold (mean feature importance + 1.5 × feature importance standard deviation). Depicted in (c) how frequently peaks were selected by SFS for the binary classification problem and (d) shows how frequently peaks were selected by SBS for the binary classification problem. Horizontal dotted lines indicates selection threshold.

Appendix Figure 5. Feature selection for mechanism of action (MoA) classification problem of *S. aureus* data (screen at 1 μM) using random forest (RF), sequential forward and backward selection (SFS and SBS). Depicted in (a) the elbow plot of the out-of-bag error for 250 decision trees for the MoA classifying trees. Depicted in (b) is the relative feature importance of each of the peaks in the mass spectrum of *S. aureus* for the MoA classification problem using 250 decision trees. Horizontal dotted line shows the feature selection threshold (mean feature importance + 1.5 × feature importance standard deviation). Depicted in (c) how frequently peaks were selected by SFS for the MoA classification problem and (d) shows how frequently peaks were selected by SBS for the MoA classification problem. Horizontal dotted lines indicates selection threshold.
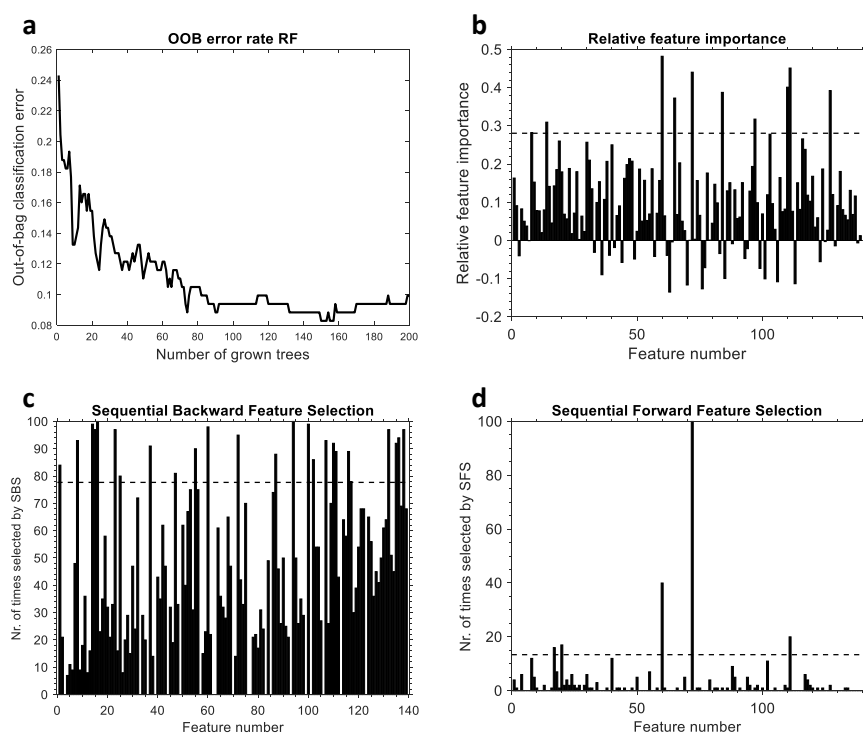
Appendix Figure 6. Feature selection for binary classification problem of *C. albicans* data using random forest (RF), sequential forward and backward selection (SFS and SBS). Depicted in (a) the elbow plot of the out-of-bag (OOB) error for 200 decision trees for the binary classifying trees. Depicted in (b) is the relative feature importance of each of the peaks in the mass spectrum of *C. albicans* for the binary classification problem using 200 decision trees. Horizontal dotted line shows the feature selection threshold (mean feature importance + 1.5 × feature importance standard deviation). Depicted in (c) how frequently peaks were selected by SFS for the *C. albicans* classification problem and (d) shows how frequently peaks were selected by SBS for the *C. albicans* classification problem. Horizontal dotted lines indicates selection threshold.

134

Appendix Figure 7. Feature selection for mechanism of action (MoA) classification problem of *C. albicans* data using random forest (RF), sequential forward and backward selection (SFS and SBS). Depicted in (a) the elbow plot of the out-of-bag (OOB) error for 250 decision trees for the MoA classifying trees. Depicted in (b) is the relative feature importance of each of the peaks in the mass spectrum of *C. albicans* for the MoA classification problem using 250 decision trees. Horizontal dotted line shows the feature selection threshold (mean feature importance + 1.5 × feature importance standard deviation). Depicted in (c) how frequently peaks were selected by SFS for the *C. albicans* MoA classification problem and (d) shows how frequently peaks were selected by SBS for the *C. albicans* MoA classification problem. Horizontal dotted lines indicates selection threshold.

135

a OOB error rate RF

b Relative feature importance

c Sequential Backward Feature Selection
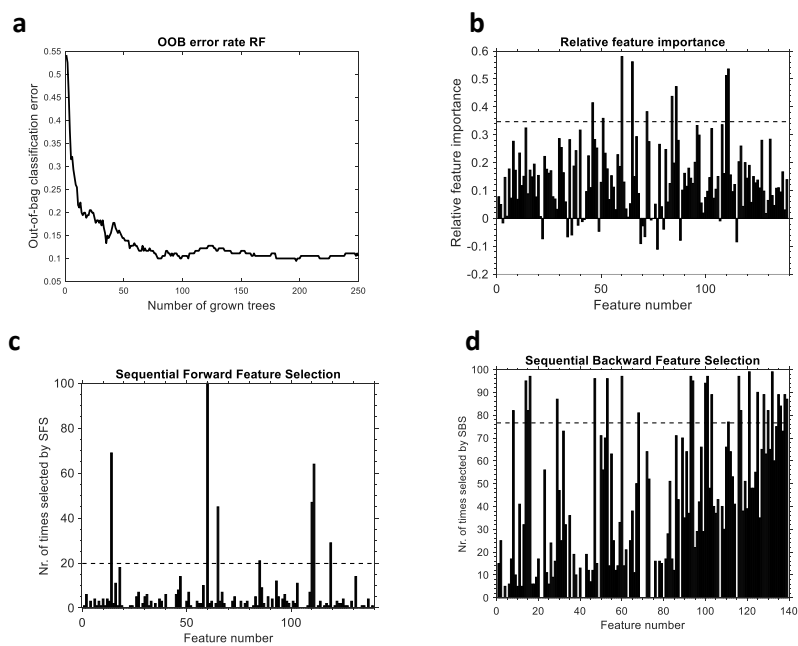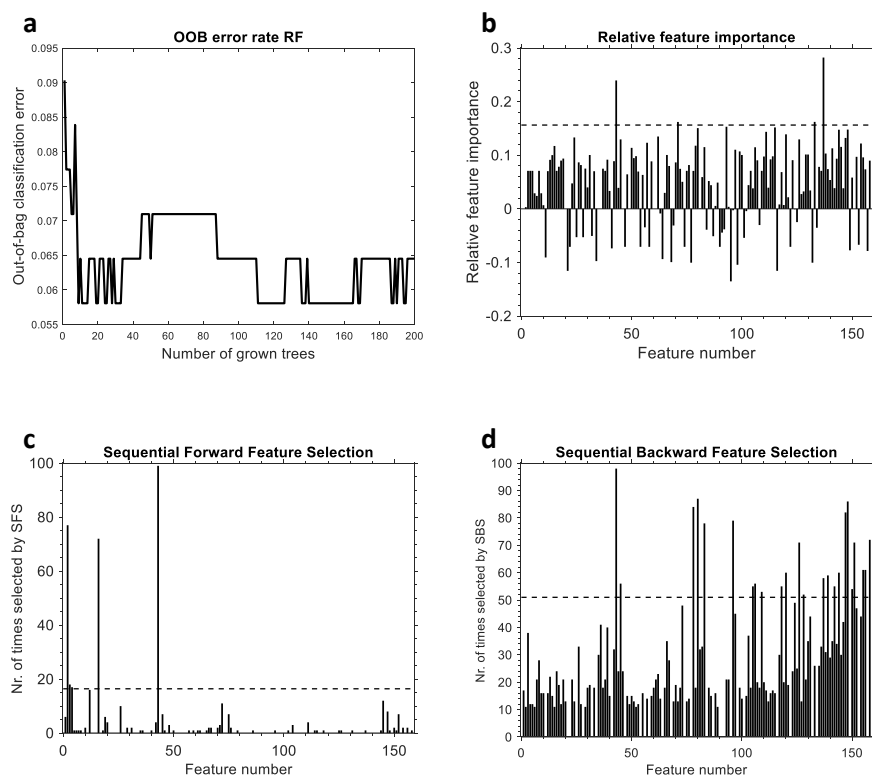
d Sequential Forward Feature Selection

Appendix Figure 8. Feature selection for binary classification problem of *S. cerevisiae* data using random forest (RF), sequential forward and backward selection (SFS and SBS). Depicted in (a) the elbow plot of the out-of-bag (OOB) error for 200 decision trees for the binary classifying trees. Depicted in (b) is the relative feature importance of each of the peaks in the mass spectrum of *S. cerevisiae* for the binary classification problem using 200 decision trees. Horizontal dotted line shows the feature selection threshold (mean feature importance + 1.5 × feature importance standard deviation). Depicted in (c) how frequently peaks were selected by SFS for the *S. cerevisiae* classification problem and (d) shows how frequently peaks were selected by SBS for the *S. cerevisiae* classification problem. Horizontal dotted lines indicates selection threshold.
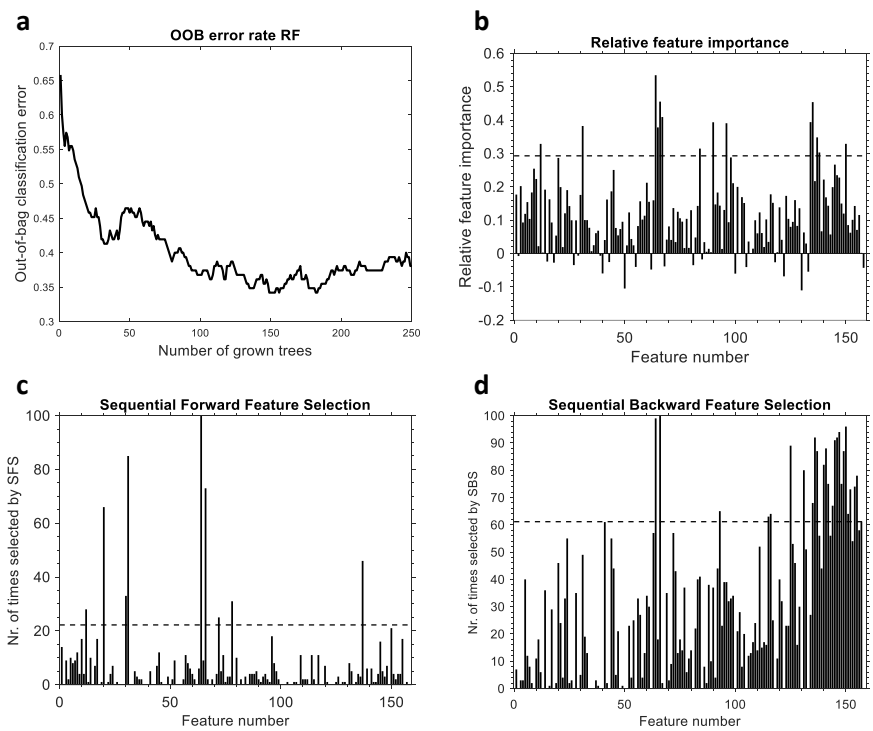
136

Appendix Figure 9. Feature selection for mechanism of action (MoA) classification problem of *S. cerevisiae* data using random forest (RF), sequential forward and backward selection (SFS and SBS). Depicted in (a) the elbow plot of the out-of-bag (OOB) error for 250 decision trees for the MoA classifying trees. Depicted in (b) is the relative feature importance of each of the peaks in the mass spectrum of *S. cerevisiae* for the MoA classification problem using 250 decision trees. Horizontal dotted line shows the feature selection threshold (mean feature importance + 1.5 × feature importance standard deviation). Depicted in (c) how frequently peaks were selected by SFS for the *S. cerevisiae* MoA classification problem and (d) shows how frequently peaks were selected by SBS for the *S. cerevisiae* MoA classification problem. Horizontal dotted lines indicates selection threshold.

Appendix Figure 10. Feature selection for binary classification problem of HeLa data (cells treated with drugs) using random forest (RF), sequential forward and backward selection (SFS and SBS). Depicted in (a) the elbow plot of the out-of-bag (OOB) error for 200 decision trees for the binary classifying trees. Depicted in (b) is the relative feature importance of each of the peaks in the mass spectrum of HeLa for the binary classification problem using 200 decision trees. Horizontal dotted line shows the feature selection threshold (mean feature importance + 1.5 × feature importance standard deviation). Depicted in (c) how frequently peaks were selected by SFS for the HeLa binary classification problem and (d) shows how frequently peaks were selected by SBS for the HeLa classification problem. Horizontal dotted lines indicates selection threshold.
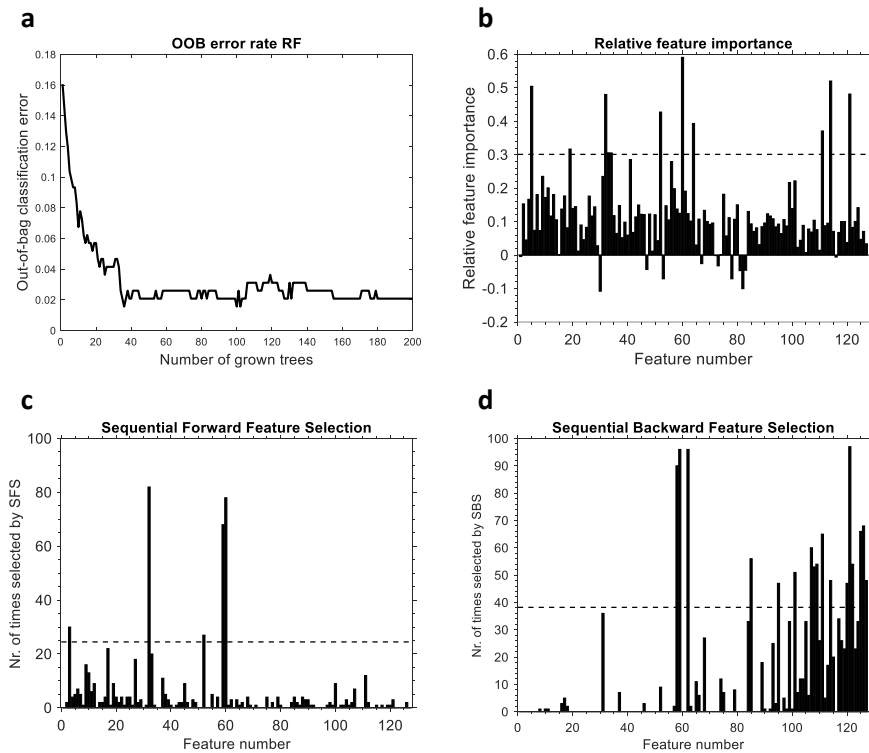
Appendix Figure 11. Feature selection for mechanism of action (MoA) classification problem of HeLa data (cells treated with drugs) using random forest (RF), sequential forward and backward selection (SFS and SBS). Depicted in (a) the elbow plot of the out-of-bag (OOB) error for 250 decision trees for the MoA classifying trees. Depicted in (b) is the relative feature importance of each of the peaks in the mass spectrum of HeLa for the MoA classification problem using 250 decision trees. Horizontal dotted line shows the feature selection threshold (mean feature importance + 1.5 × feature importance standard deviation). Depicted in (c) how frequently peaks were selected by SFS for the HeLa MoA classification problem and (d) shows how frequently peaks were selected by SBS for the HeLa MoA classification problem. Horizontal dotted lines indicates selection threshold.

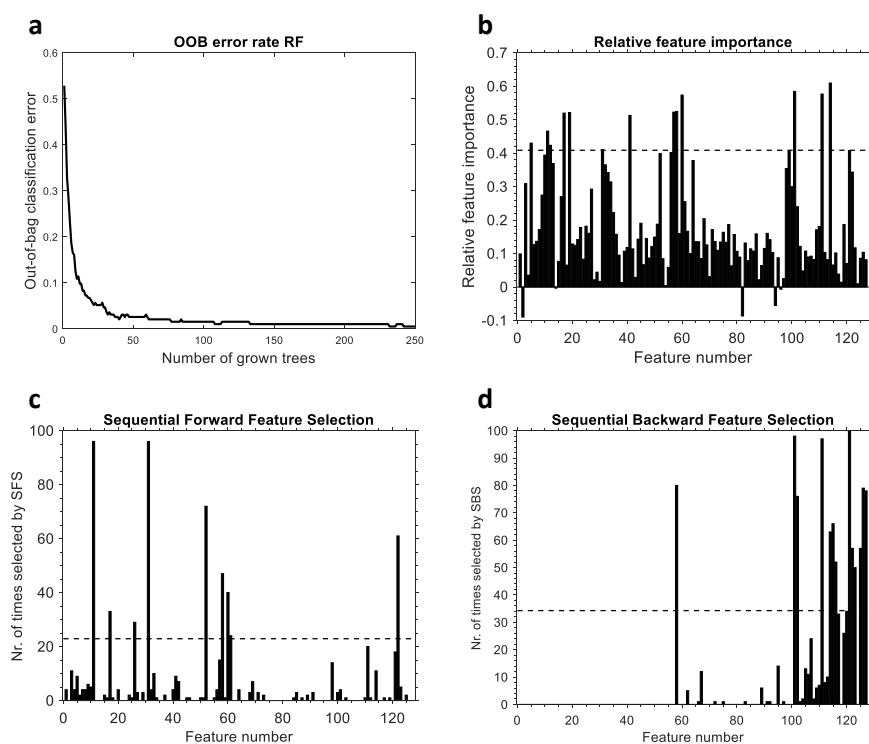Appendix Figure 12. Feature selection for binary classification problem of HeLa data (cells treated with physical and chemical stressors) using random forest (RF), sequential forward and backward selection (SFS and SBS). Depicted in (a) the elbow plot of the out-of-bag (OOB) error for 200 decision trees for the binary classifying trees. Depicted in (b) is the relative feature importance of each of the peaks in the mass spectrum of HeLa for the binary classification problem using 200 decision trees. Horizontal dotted line shows the feature selection threshold (mean feature importance + 1.5 × feature importance standard deviation). Depicted in (c) how frequently peaks were selected by SFS for the HeLa binary classification problem and (d) shows how frequently peaks were selected by SBS for the HeLa classification problem. Horizontal dotted lines indicates selection threshold.

Appendix Figure 13. Feature selection for mechanism of action (MoA) classification problem of HeLa data (cells treated with physical and chemical stressors) using random forest (RF), sequential forward and backward selection (SFS and SBS). Depicted in (a) the elbow plot of the out-of-bag (OOB) error for 250 decision trees for the MoA classifying trees. Depicted in (b) is the relative feature importance of each of the peaks in the mass spectrum of HeLa for the MoA classification problem using 250 decision trees. Horizontal dotted line shows the feature selection threshold (mean feature importance + 1.5 × feature importance standard deviation). Depicted in (c) how frequently peaks were selected by SFS for the HeLa MoA classification problem and (d) shows how frequently peaks were selected by SBS for the HeLa MoA classification problem. Horizontal dotted lines indicates selection threshold.

7.2 Appendix Tables

Appendix Table 1. Prediction details of external validation data set of *E. coli* using aggregated feature set. The number 1 (green) indicates a correct prediction, a zero (red) indicating an incorrect prediction by that model (indicated in top row) for each of the drugs (first column).

Drug	Linear Discriminant	Quadratic Discriminant	Naïve Bayes	Linear SVM	Quadratic SVM	Cubic SVM	Medium Gaussian SVM	Cosine KNN	Tree
Azithromycin dihydrate	1	1	1	1	1	1	1	1	1
Thalidomide	1	1	1	1	1	1	1	1	1
Fusidic acid	1	1	1	1	1	1	1	1	1
Trimethoprim	1	1	1	1	1	1	1	1	1
Nalidixic acid	1	1	1	1	1	1	1	1	1
Metoprolol-tartrate	0	1	1	1	1	1	1	1	1
Ampicillin-Na	1	1	0	1	1	1	1	1	1
Sumatriptan	0	1	0	0	1	1	1	1	0
Fenbendazole	1	1	1	1	1	1	1	1	1
Paromomycin sulphate	1	1	1	1	1	1	1	0	1
Novobiocin-Na	1	1	1	1	1	1	1	1	1
Brucine tetrahydrate	1	1	1	1	1	1	1	1	1
Umifenovir HCl	1	1	1	1	1	1	1	1	1
Tiamulin fumarate	0	0	0	0	0	0	0	0	0
Ergotamine tartrate	1	1	1	1	1	1	1	1	1
Ephedrine-HCl	1	1	1	1	1	1	1	1	1
Loperamide-HCl	1	1	1	1	1	1	1	1	1
Paroxetine HCl hemihydrate	1	1	1	1	1	1	1	1	1
Cefuroxime-Na	1	1	1	1	1	1	1	1	1
Chlortetracycline-HCl	1	1	1	1	1	1	1	1	1

Appendix Table 2. Peaks selected for binary and mechanism of action (MoA) model for *C. albicans*. Peaks indicated with asterisk (*) are depicted in Figure 17 and Figure 18.

Binary model	MoA model
m/z	*m/z*
3883.0	3987.1
4033.5*	5397.4
5104.9	5745.3*
6424.0	5848.1*
7615.3	5910.7*

Appendix Table 3. Peaks selected for *S. cerevisiae* for binary and mechanism of action (MoA) classification models. Details of peaks indicated with an asterisk (*) are depicted in Figure 15.

Binary model	MoA model
m/z	*m/z*
2679.8*	2817.5
2817.5	3868.6*
3868.6	4035.5*
4183.1	5659.8*
5659.8*	5665.7*
5665.7*	

Appendix Table 4. Reference peaks used for spectra alignment during spectral processing of Hela data set. Listed is the respective protein name in the first column, second column lists corresponding UniProtKB accession number. Third column lists the theoretical m/z value, followed by the observed m/z value in the fourth column. Fifth column lists absolute mass error in ppm. Last column shows theoretically calculated isoelectric point (pI).

Name, notes	UniprotKB	Theoretical m/z	Observed m/z	Error (ppm)	pI
Minor histocompatibility protein HB-1, suspected natural variant (Y→H) or PTM of O97980	O97980	4939.5	4939.1	88	4.8
Minor histocompatibility protein HB-1	O97980	4965.5	4966.3	150	5.0
metallothionin-2, acetylated	P02795	6085.2	6085.6	63	8.2
Ribosomal 40S S30	P62861	6648.9	6650.0	172	12.3
Ubiquitin, position 77-152	P0CG47	8565.9	8565.6	27	6.5

Bibliography

1.   O'Neill, *Securing new drugs for future generations: the pipeline of antibiotics.* 2015.

2.   Levy, S.B., *Factors impacting on the problem of antibiotic resistance.* J Antimicrob Chemother, 2002. **49**(1): p. 25-30.

3.   Silver, L.L., *Challenges of antibacterial discovery.* Clin Microbiol Rev, 2011. **24**(1): p. 71-109.

4.   Ventola, C.L., *The antibiotic resistance crisis: part 1: causes and threats.* P&T, 2015. **40**(4): p. 277-283.

5.   O'Neill, *Antimicrobial Resistance: Tackling a crisis for the health and wealth of nations* 2014.

6.   CDC, *Centres for Disease Control, U.S Department of Health and Human Services. Antibiotic resistance threats in the United States.* 2013.

7.   Roemer, T. and D.J. Krysan, *Antifungal drug development: challenges, unmet clinical needs, and new approaches.* Cold Spring Harb Perspect Med, 2014. **4**(5): p. a019703.

8.   WHO, *No Time to Wait: Securing the future from drug-resistant infections.* April 2019.

9.   Coates, A., et al., *The future challenges facing the development of new antimicrobial drugs.* Nat Rev Drug Discov, 2002. **1**(11): p. 895-910.

10.   Fleming, A., *On the Antibacterial Action of Cultures of a Penicillium, with Special Reference to their Use in the Isolation of B. influenzæ.* Br J Exp Pathol, 1929. **10**(3): p. 226-236.

11.   Tipper, D.J., *Mode of action of beta-lactam antibiotics.* Pharmacol Ther, 1985. **27**(1): p. 1-35.

12.   Skold, O., *Sulfonamides and trimethoprim.* Expert Rev Anti Infect Ther, 2010. **8**(1): p. 1-6.

13.   Gleckman, R., N. Blagg, and D.W. Joubert, *Trimethoprim: mechanisms of action, antimicrobial activity, bacterial resistance, pharmacokinetics, adverse reactions, and therapeutic indications.* Pharmacotherapy, 1981. **1**(1): p. 14-20.

14.   Smith, C.L. and K.R. Powell, *Review of the sulfonamides and trimethoprim.* Pediatr Rev, 2000. **21**(11): p. 368-71.

15.   Gutierrez, A., J.M. Stokes, and I. Matic, *Our Evolving Understanding of the Mechanism of Quinolones.* Antibiotics (Basel), 2018. **7**(2): p. 32.

16.   Aldred, K.J., R.J. Kerns, and N. Osheroff, *Mechanism of quinolone action and resistance.* Biochemistry, 2014. **53**(10): p. 1565-74.

17.   Calvori, C., et al., *Effect of rifamycin on protein synthesis.* Nature, 1965. **207**(995): p. 417-8.

18.   Lin, J., et al., *Ribosome-Targeting Antibiotics: Modes of Action, Mechanisms of Resistance, and Implications for Drug Design.* Annu Rev Biochem, 2018. **87**: p. 451-478.

19.   Kannan, K. and A.S. Mankin, *Macrolide antibiotics in the ribosome exit tunnel: species-specific binding and action.* Ann N Y Acad Sci, 2011. **1241**(1): p. 33-47.

20.   Vázquez, D., *Protein Synthesis and Translation Inhibitors*, in *Inhibitors of Protein Biosynthesis. Molecular Biology Biochemistry and Biophysics, vol 30*. 1979, Springer, Berlin, Heidelberg. p. 1-14.

21.   Mingeot-Leclercq, M.P., Y. Glupczynski, and P.M. Tulkens, *Aminoglycosides: activity and resistance.* Antimicrob Agents Chemother, 1999. **43**(4): p. 727-37.

22.   Duggar, B.M., *Aureomycin; a product of the continuing search for new antibiotics.* Ann N Y Acad Sci, 1948. **51**(Art. 2): p. 177-81.

23.   Griffin, M.O., et al., *Tetracyclines: a pleitropic family of compounds with promising therapeutic properties. Review of the literature.* Am J Physiol Cell Physiol, 2010. **299**(3): p. C539-48.

24.   Davies, J., *Where have All the Antibiotics Gone?* Can J Infect Dis Med Microbiol, 2006. **17**(5): p. 287-90.

25.   Gould, K., *Antibiotics: from prehistory to the present day.* J Antimicrob Chemother, 2016. **71**(3): p. 572-5.

26.   von Bubnoff, A., *Seeking new antibiotics in nature's backyard.* Cell, 2006. **127**(5): p. 867-9.

27.   Melnyk, A.H., A. Wong, and R. Kassen, *The fitness costs of antibiotic resistance mutations.* Evol Appl, 2015. **8**(3): p. 273-83.

28.   Rosenblatt-Farrell, N., *The landscape of antibiotic resistance.* Environ Health Perspect, 2009. **117**(6): p. A244-50.

29.   Brown, E.D. and G.D. Wright, *Antibacterial drug discovery in the resistance era.* Nature, 2016. **529**(7586): p. 336-43.

30.   Blair, J.M., et al., *Molecular mechanisms of antibiotic resistance.* Nat Rev Microbiol, 2015. **13**(1): p. 42-51.

31.   Walsh, C., *Molecular mechanisms that confer antibacterial drug resistance.* Nature, 2000. **406**(6797): p. 775-81.

32.   Lange, R.P., et al., *The targets of currently used antibacterial agents: lessons for drug discovery.* Curr Pharm Des, 2007. **13**(30): p. 3140-54.

33.   Payne, D.J., et al., *Drugs for bad bugs: confronting the challenges of antibacterial discovery.* Nat Rev Drug Discov, 2007. **6**(1): p. 29-40.

34.   Silver, L.L., *Appropriate Targets for Antibacterial Drugs.* Cold Spring Harb Perspect Med, 2016. **6**(12): p. a030239.

35.   Lewis, K., *Platforms for antibiotic discovery.* Nat Rev Drug Discov, 2013. **12**(5): p. 371-87.

36.   Worthington, R.J. and C. Melander, *Combination approaches to combat multidrug-resistant bacteria.* Trends Biotechnol, 2013. **31**(3): p. 177-84.

37.   Ball, P., *The clinical development and launch of amoxicillin/clavulanate for the treatment of a range of community-acquired infections.* Int J Antimicrob Agents, 2007. **30 Suppl 2**: p. S113-7.

38.   WHO, *Antibacterial agents in clinical development: an analysis of the antibacterial clinical development pipeline. Geneva: World Health Organization; 2019. Licence: CC BY-NC-SA 3.0 IGO.* 2019.

39.   Sader, H.S., et al., *Antimicrobial activity of POL7306 tested against clinical isolates of Gram-negative bacteria collected worldwide.* J Antimicrob Chemother, 2020. **dkaa020**(ahead of print).

40.   Stokes, J.M., et al., *A Deep Learning Approach to Antibiotic Discovery.* Cell, 2020. **180**(4): p. 688-702 e13.

41. Livermore, D.M., *Discovery research: the scientific challenge of finding new antibiotics.* J Antimicrob Chemother, 2011. **66**(9): p. 1941-4.

42. Sanglard, D., A. Coste, and S. Ferrari, *Antifungal drug resistance mechanisms in fungal pathogens from the perspective of transcriptional gene regulation.* FEMS Yeast Res, 2009. **9**(7): p. 1029-50.

43. Thompson, G.R., 3rd, J. Cadena, and T.F. Patterson, *Overview of antifungal agents.* Clin Chest Med, 2009. **30**(2): p. 203-15.

44. Chandrasekar, P., *Management of invasive fungal infections: a role for polyenes.* J Antimicrob Chemother, 2011. **66**(3): p. 457-65.

45. Sanglard, D., *Finding the needle in a haystack: Mapping antifungal drug resistance in fungal pathogen by genomic approaches.* PLoS Pathog, 2019. **15**(1): p. e1007478.

46. Barrett-Bee, K. and G. Dixon, *Ergosterol biosynthesis inhibition: a target for antifungal agents.* Acta Biochim Pol, 1995. **42**(4): p. 465-79.

47. Donovick, R., et al., *Amphotericins A and B, antifungal antibiotics produced by a streptomycete. I. In vitro studies.* Antibiot Annu, 1955. **3**: p. 579-86.

48. Gallis, H.A., R.H. Drew, and W.W. Pickard, *Amphotericin B: 30 years of clinical experience.* Rev Infect Dis, 1990. **12**(2): p. 308-29.

49. Terrell, C.L., *Antifungal agents. Part II. The azoles.* Mayo Clin Proc, 1999. **74**(1): p. 78-100.

50. Lamb, D., D. Kelly, and S. Kelly, *Molecular aspects of azole antifungal action and resistance.* Drug Resist Updat, 1999. **2**(6): p. 390-402.

51. Ghannoum, M.A. and L.B. Rice, *Antifungal agents: Mode of action, mechanisms of resistance, and correlation of these mechanisms with bacterial resistance.* Clin Microbiol Rev, 1999. **12**(4): p. 501-17.

52. Birnbaum, J.E., *Pharmacology of the allylamines.* J Am Acad Dermatol, 1990. **23**(4 Pt 2): p. 782-5.

53. Denning, D.W., *Echinocandin antifungal drugs.* Lancet, 2003. **362**(9390): p. 1142-51.

54. Letscher-Bru, V. and R. Herbrecht, *Caspofungin: the first representative of a new antifungal class.* J Antimicrob Chemother, 2003. **51**(3): p. 513-21.

55. Elewski, B.E., et al., *Efficacy and safety of tavaborole topical solution, 5%, a novel boron-based antifungal agent, for the treatment of toenail onychomycosis: Results from 2 randomized phase-III studies.* J Am Acad Dermatol, 2015. **73**(1): p. 62-9.

56. Jinna, S. and J. Finch, *Spotlight on tavaborole for the treatment of onychomycosis.* Drug Des Devel Ther, 2015. **9**: p. 6185-90.

57. Vermes, A., H.J. Guchelaar, and J. Dankert, *Flucytosine: a review of its pharmacology, clinical indications, pharmacokinetics, toxicity and drug interactions.* J Antimicrob Chemother, 2000. **46**(2): p. 171-9.

58. Gull, K. and A.P. Trinci, *Griseofulvin inhibits fungal mitosis.* Nature, 1973. **244**(5414): p. 292-4.

59. Grover, N.D., *Echinocandins: A ray of hope in antifungal drug therapy.* Indian J Pharmacol, 2010. **42**(1): p. 9-11.

60. Chaabane, F., et al., *Review on Antifungal Resistance Mechanisms in the Emerging Pathogen Candida auris.* Front Microbiol, 2019. **10**(2788): p. 2788.

61. Cowen, L.E., et al., *Mechanisms of Antifungal Drug Resistance.* Cold Spring Harb Perspect Med, 2014. **5**(7): p. a019752.

62. Ramage, G., et al., *Fungal biofilm resistance.* Int J Microbiol, 2012. **2012**: p. 528521.

63. Perfect, J.R., *The antifungal pipeline: a reality check.* Nat Rev Drug Discov, 2017. **16**(9): p. 603-616.

64. McCarthy, M.W., et al., *Novel Agents and Drug Targets to Meet the Challenges of Resistant Fungi.* J Infect Dis, 2017. **216**(suppl_3): p. S474-S483.

65. Del Poeta, M., *Special Issue: Novel Antifungal Drug Discovery.* J Fungi (Basel), 2016. **2**(4): p. 33.

66. Schatz, A., E. Bugie, and S.A. Waksman, *Streptomycin, a substance exhibiting antibiotic activity against gram-positive and gram-negative bacteria.* Exp Biol Med (Maywood), 1944. **55**(1): p. 66-9.

67. Mills, S.D., *The role of genomics in antimicrobial discovery.* J Antimicrob Chemother, 2003. **51**(4): p. 749-52.

68. Hughes, D. and A. Karlen, *Discovery and preclinical development of new antibiotics.* Ups J Med Sci, 2014. **119**(2): p. 162-9.

69. Ribeiro da Cunha, B., L.P. Fonseca, and C.R.C. Calado, *Antibiotic Discovery: Where Have We Come from, Where Do We Go?* Antibiotics (Basel), 2019. **8**(2): p. 45.

70. Zheng, W., N. Thorne, and J.C. McKew, *Phenotypic screens as a renewed approach for drug discovery.* Drug Discov Today, 2013. **18**(21-22): p. 1067-73.

71. Swinney, D.C. and J. Anthony, *How Were New Medicines Discovered?* Nat Rev Drug Discov, 2011. **10**(7): p. 507-519.

72. Swinney, D.C., *The contribution of mechanistic understanding to phenotypic screening for first-in-class medicines.* J Biomol Screen, 2013. **18**(10): p. 1186-92.

73. Garattini, S., *Are me-too drugs justified?* J Nephrol, 1997. **10**(6): p. 283-94.

74. Wagner, B.K., *The resurgence of phenotypic screening in drug discovery and development.* Expert Opin Drug Discov, 2016. **11**(2): p. 121-5.

75. Hombach, M., R. Zbinden, and E.C. Bottger, *Standardisation of disk diffusion results for antibiotic susceptibility testing using the sirscan automated zone reader.* BMC Microbiol, 2013. **13**(1): p. 225.

76. Balouiri, M., M. Sadiki, and S.K. Ibnsouda, *Methods for in vitro evaluating antimicrobial activity: A review.* J Pharm Anal, 2016. **6**(2): p. 71-79.

77. De La Fuente, R., et al., *Small molecules with antimicrobial activity against E. coli and P. aeruginosa identified by high-throughput screening.* Br J Pharmacol, 2006. **149**(5): p. 551-9.

78. Stock, I. and B. Wiedemann, *Natural antibiotic susceptibility of Escherichia coli, Shigella, E. vulneris, and E. hermannii strains.* Diagn Microbiol Infect Dis, 1999. **33**(3): p. 187-99.

79. Chen, H., et al., *Evolutions in fragment-based drug design: the deconstruction-reconstruction approach.* Drug Discov Today, 2015. **20**(1): p. 105-13.

80.   Rees, D.C., et al., *Fragment-based lead discovery.* Nat Rev Drug Discov, 2004. **3**(8): p. 660-72.

81.   Feng, Y., et al., *Multi-parameter phenotypic profiling: using cellular effects to characterize small-molecule compounds.* Nat Rev Drug Discov, 2009. **8**(7): p. 567-78.

82.   Lamsa, A., et al., *Rapid Inhibition Profiling in Bacillus subtilis to Identify the Mechanism of Action of New Antimicrobials.* ACS Chem Biol, 2016. **11**(8): p. 2222-31.

83.   Nonejuie, P., et al., *Bacterial cytological profiling rapidly identifies the cellular pathways targeted by antibacterial molecules.* Proc Natl Acad Sci U S A, 2013. **110**(40): p. 16169-74.

84.   Young, D.W., et al., *Integrating high-content screening and ligand-target prediction to identify mechanism of action.* Nat Chem Biol, 2008. **4**(1): p. 59-68.

85.   Athamneh, A.I., et al., *Phenotypic profiling of antibiotic response signatures in Escherichia coli using Raman spectroscopy.* Antimicrob Agents Chemother, 2014. **58**(3): p. 1302-14.

86.   Liu, T.T., et al., *A high speed detection platform based on surface-enhanced Raman scattering for monitoring antibiotic-induced chemical changes in bacteria cell wall.* PLoS One, 2009. **4**(5): p. e5470.

87.   Gross, J.H., *Mass spectrometry, A textbook.* Springer International Publishing, 2017.

88.   Fenn, J.B., et al., *Electrospray ionization for mass spectrometry of large biomolecules.* Science, 1989. **246**(4926): p. 64-71.

89.   Tanaka, K., et al., *Protein and polymer analyses up to m/z 100 000 by laser ionization time-of-flight mass spectrometry.* Rapid Commun Mass Sp, 1988. **2**(8): p. 151-153.

90.   Hillenkamp, F., et al., *Matrix-assisted laser desorption/ionization mass spectrometry of biopolymers.* Anal Chem, 1991. **63**(24): p. 1193A-1203A.

91.   Patel, R., *MALDI-TOF MS for the diagnosis of infectious diseases.* Clin Chem, 2015. **61**(1): p. 100-11.

92.   Lewis, J.K., J. Wei, and G. Siuzdak, *Matrix-Assisted Laser Desorption/Ionization Mass Spectrometry in Peptide and Protein Analysis*, in *Encyclopedia of Analytical Chemistry*, R.A. Meyers and C. Schöneich, Editors. 2006 Published Online: DOI: 10.1002/9780470027318.a1621.

93.   Maier, T., et al., *Fast and reliable MALDI-TOF MS–based microorganism identification.* Nature Meth, 2006. **3**(4): p. i-ii.

94.   Karas, M., M. Gluckmann, and J. Schafer, *Ionization in matrix-assisted laser desorption/ionization: singly charged molecular ions are the lucky survivors.* J Mass Spectrom, 2000. **35**(1): p. 1-12.

95.   Jaskolla, T.W. and M. Karas, *Compelling evidence for Lucky Survivor and gas phase protonation: the unified MALDI analyte protonation mechanism.* J Am Soc Mass Spectrom, 2011. **22**(6): p. 976-88.

96.   Coombes, K.R., K.A. Baggerly, and J.S. Morris, *Pre-Processing Mass Spectrometry Data*, in *Fundamentals of Data Mining in Genomics and Proteomics*, W. Dubitzky, M. Granzow, and D. Berrar, Editors. 2007, Springer US: Boston, MA. p. 79-102.

97.   Albrethsen, J., *Reproducibility in protein profiling by MALDI-TOF mass spectrometry.* Clin Chem, 2007. **53**(5): p. 852-8.

98.   Wagner, M., D. Naik, and A. Pothen, *Protocols for disease classification from mass spectrometry data.* Proteomics, 2003. **3**(9): p. 1692-8.

99.   Stanford, T.E., C.J. Bagley, and P.J. Solomon, *Informed baseline subtraction of proteomic mass spectrometry data aided by a novel sliding window algorithm.* Proteome Sci, 2016. **14**(1): p. 19.

100.   Gibb, S. and K. Strimmer, *MALDIquant: a versatile R package for the analysis of mass spectrometry data.* Bioinformatics, 2012. **28**(17): p. 2270-1.

101.   Palarea-Albaladejo, J., et al., *MALDIrppa: quality control and robust analysis for mass spectrometry data.* Bioinformatics, 2018. **34**(3): p. 522-523.

102.   Li, X., et al., *SELDI-TOF Mass Spectrometry Protein Data*, in *Bioinformatics and Computational Biology Solutions Using R and Bioconductor*, R. Gentleman, et al., Editors. 2005, Springer New York: New York, NY. p. 91-109.

103.   Coombes, K.R., et al., *Improved peak detection and quantification of mass spectrometry data acquired from surface-enhanced laser desorption and ionization by denoising spectra with the undecimated discrete wavelet transform.* Proteomics, 2005. **5**(16): p. 4107-17.

104.   Yang, C., Z. He, and W. Yu, *Comparison of public peak detection algorithms for MALDI mass spectrometry data analysis.* BMC Bioinformatics, 2009. **10**(1): p. 4.

105.   Sauve, A.C., Speed, T. P., *Normalization, baseline correction and alignment of high-throughput mass spectrometry data.* Conference Proceedings, 2004.

106.   Alexandrov, T., et al., *Biomarker discovery in MALDI-TOF serum protein profiles using discrete wavelet transformation.* Bioinformatics, 2009. **25**(5): p. 643-9.

107.   Deininger, S.O., et al., *Normalization in MALDI-TOF imaging datasets of proteins: practical considerations.* Anal Bioanal Chem, 2011. **401**(1): p. 167-81.

108.   Borgaonkar, S.P., et al., *Comparison of normalization methods for the identification of biomarkers using MALDI-TOF and SELDI-TOF mass spectra.* OMICS, 2010. **14**(1): p. 115-26.

109.   Meuleman, W., et al., *Comparison of normalisation methods for surface-enhanced laser desorption and ionisation (SELDI) time-of-flight (TOF) mass spectrometry data.* BMC Bioinformatics, 2008. **9**: p. 88.

110.   Szajli, E., T. Feher, and K.F. Medzihradszky, *Investigating the quantitative nature of MALDI-TOF MS.* Mol Cell Proteomics, 2008. **7**(12): p. 2410-8.

111.   Marczyk, M., J. Polanska, and A. Polanski. *Comparison of Algorithms for Profile-Based Alignment of Low Resolution MALDI-ToF Spectra*. in *Man-Machine Interactions 3*. 2014. Springer International Publishing, Cham.

112.   Tracy, M.B., et al., *Precision enhancement of MALDI-TOF MS using high resolution peak detection and label-free alignment.* Proteomics, 2008. **8**(8): p. 1530-8.

113.   Wijetunge, C.D., et al., *A new peak detection algorithm for MALDI mass spectrometry data based on a modified Asymmetric Pseudo-Voigt model.* BMC Genomics, 2015. **16 Suppl 12**: p. S12.

114.   Baggerly, K.A., et al., *A comprehensive approach to the analysis of matrix-assisted laser desorption/ionization-time of flight proteomics spectra from serum samples.* Proteomics, 2003. **3**(9): p. 1667-72.

115.   Bauer, C., R. Cramer, and J. Schuchhardt, *Evaluation of Peak-Picking Algorithms for Protein Mass Spectrometry*, in *Data Mining in Proteomics: From Standards to Applications*, M. Hamacher, M. Eisenacher, and C. Stephan, Editors. 2011, Humana Press: Totowa, NJ. p. 341-352.

116.   Holland, R.D., et al., *Rapid identification of intact whole bacteria based on spectral patterns using matrix-assisted laser desorption/ionization with time-of-flight mass spectrometry.* Rapid Commun Mass Spectrom, 1996. **10**(10): p. 1227-32.

117.   Arnold, R.J. and J.P. Reilly, *Fingerprint matching of E. coli strains with matrix-assisted laser desorption/ionization time-of-flight mass spectrometry of whole cells using a modified correlation approach.* Rapid Commun Mass Spectrom, 1998. **12**(10): p. 630-6.

118.   Anhalt, J.P. and C. Fenselau, *Identification of Bacteria Using Mass-Spectrometry.* Anal Chem, 1975. **47**(2): p. 219-225.

119.   van Belkum, A., et al., *Progress in proteomics for clinical microbiology: MALDI-TOF MS for microbial species identification and more.* Expert Rev Proteomics, 2015. **12**(6): p. 595-605.

120.   Hart, P.J., et al., *A method for the detection of antibiotic resistance markers in clinical strains of Escherichia coli using MALDI mass spectrometry.* J Microbiol Methods, 2015. **111**: p. 1-8.

121.   Schubert, S. and M. Kostrzewa, *Chapter 14 - MALDI-TOF Mass Spectrometry in the Clinical Microbiology Laboratory; Beyond Identification*, in *Methods in Microbiology*, S. Andrew and T. Yi-Wei, Editors. 2015, Academic Press. p. 501-524.

122.   Sanguinetti, M. and B. Posteraro, *Mass spectrometry applications in microbiology beyond microbe identification: progress and potential.* Expert Rev Proteomics, 2016. **13**(10): p. 965-977.

123.   DeMarco, M.L. and B.A. Ford, *Beyond identification: emerging and future uses for MALDI-TOF mass spectrometry in the clinical microbiology laboratory.* Clin Lab Med, 2013. **33**(3): p. 611-28.

124.   Croxatto, A., G. Prod'hom, and G. Greub, *Applications of MALDI-TOF mass spectrometry in clinical diagnostic microbiology.* FEMS Microbiol Rev, 2012. **36**(2): p. 380-407.

125.   Sandrin, T.R., J.E. Goldstein, and S. Schumaker, *MALDI TOF MS profiling of bacteria at the strain level: a review.* Mass Spectrom Rev, 2013. **32**(3): p. 188-217.

126.   Sparbier, K., et al., *MALDI biotyper-based rapid resistance detection by stable-isotope labeling.* J Clin Microbiol, 2013. **51**(11): p. 3741-8.

127.   Sparbier, K., S. Schubert, and M. Kostrzewa, *MBT-ASTRA: A suitable tool for fast antibiotic susceptibility testing?* Methods, 2016. **104**: p. 48-54.

128.   Burckhardt, I. and S. Zimmermann, *Susceptibility Testing of Bacteria Using Maldi-Tof Mass Spectrometry.* Front Microbiol, 2018. **9**: p. 1744.

129.   Marinach, C., et al., *MALDI-TOF MS-based drug susceptibility testing of pathogens: the example of Candida albicans and fluconazole.* Proteomics, 2009. **9**(20): p. 4627-31.

130.   CLSI, *Performance Standards for Antimicrobial Susceptibility Testing; Twenty-Third Informational Supplement* CLSI document M100-S23. Wayne, PA: Clinical and Laboratory Standards Institute, 2013.

131. Jung, J.S., et al., *Evaluation of a Semiquantitative Matrix-Assisted Laser Desorption Ionization-Time of Flight Mass Spectrometry Method for Rapid Antimicrobial Susceptibility Testing of Positive Blood Cultures.* J Clin Microbiol, 2016. **54**(11): p. 2820-2824.

132. Lange, C., et al., *Quantitative matrix-assisted laser desorption ionization-time of flight mass spectrometry for rapid resistance detection.* J Clin Microbiol, 2014. **52**(12): p. 4155-62.

133. Wieser, A. and S. Schubert, *MALDI-TOF MS entering the microbiological diagnostic laboratory – from fast identification to resistance testing.* Trends Anal Chem, 2016. **84, Part B**: p. 80-87.

134. Ceyssens, P.J., et al., *Matrix-Assisted Laser Desorption Ionization-Time of Flight Mass Spectrometry for Combined Species Identification and Drug Sensitivity Testing in Mycobacteria.* J Clin Microbiol, 2017. **55**(2): p. 624-634.

135. Schott, A.S., et al., *MALDI-TOF Mass Spectrometry Enables a Comprehensive and Fast Analysis of Dynamics and Qualities of Stress Responses of Lactobacillus paracasei subsp. paracasei F19.* PLoS One, 2016. **11**(10): p. e0165504.

136. Bozik, M., et al., *Stress response of Escherichia coli to essential oil components - insights on low-molecular-weight proteins from MALDI-TOF.* Sci Rep, 2018. **8**(1): p. 13042.

137. Dong, H., et al., *Rapid detection of apoptosis in mammalian cells by using intact cell MALDI mass spectrometry.* Analyst, 2011. **136**(24): p. 5181-9.

138. Kober, S.L., et al., *Intact cell mass spectrometry as a rapid and specific tool for the differentiation of toxic effects in cell-based ecotoxicological test systems.* Anal Bioanal Chem, 2015. **407**(25): p. 7721-31.

139. Chiu, N.H., et al., *Rapid differentiation of in vitro cellular responses to toxic chemicals by using matrix-assisted laser desorption/ionization time-of-flight mass spectrometry.* Environ Toxicol Chem, 2015. **34**(1): p. 161-6.

140. Vanhara, P., et al., *Intact Cell Mass Spectrometry as a Quality Control Tool for Revealing Minute Phenotypic Changes of Cultured Human Embryonic Stem Cells.* Stem Cells Transl Med, 2018. **7**(1): p. 109-114.

141. Morris, J.S., et al., *Feature extraction and quantification for mass spectrometry in biomedical applications using the mean spectrum.* Bioinformatics, 2005. **21**(9): p. 1764-1775.

142. Tarca, A.L., et al., *Machine learning and its applications to biology.* PLoS Comput Biol, 2007. **3**(6): p. e116.

143. Saeys, Y., I. Inza, and P. Larranaga, *A review of feature selection techniques in bioinformatics.* Bioinformatics, 2007. **23**(19): p. 2507-17.

144. Guyon, I. and A. Elisseeff, *An Introduction to Feature Extraction*, in *Feature Extraction: Foundations and Applications*, I. Guyon, et al., Editors. 2006, Springer-Verlag Berlin Heidelberg. p. 1-25.

145. De Bruyne, K., et al., *Bacterial species identification from MALDI-TOF mass spectra through data analysis and machine learning.* Syst Appl Microbiol, 2011. **34**(1): p. 20-9.

146. Larranaga, P., et al., *Machine learning in bioinformatics.* Brief Bioinform, 2006. **7**(1): p. 86-112.

147. Liu, Q., et al., *Comparison of feature selection and classification for MALDI-MS data.* BMC Genomics, 2009. **10 Suppl 1**(Suppl 1 S3).

148. Petricoin, E.F., et al., *Use of proteomic patterns in serum to identify ovarian cancer.* Lancet, 2002. **359**(9306): p. 572-7.

149. Rodrigo, M.A., et al., *MALDI-TOF MS as evolving cancer diagnostic tool: a review.* J Pharm Biomed Anal, 2014. **95**: p. 245-55.

150. Stańczyk, U., *Feature Evaluation by Filter, Wrapper, and Embedded Approaches*, in *Feature Selection for Data and Pattern Recognition. Studies in Computational Intelligence, vol 584*, U. Stańczyk and L. Jain, Editors. 2015, Springer Berlin Heidelberg. p. 29-44.

151. Kuschner, K.W., et al., *A Bayesian network approach to feature selection in mass spectrometry data.* BMC Bioinformatics, 2010. **11**(1): p. 177.

152. Guyon, I., et al., *Gene selection for cancer classification using support vector machines.* Machine Learning, 2002. **46**(1-3): p. 389-422.

153. Datta, S. and V. Pihur, *Feature selection and machine learning with mass spectrometry data.* Methods Mol Biol, 2010. **593**: p. 205-29.

154. Breiman, L., *Random forests.* Machine Learning, 2001. **45**(1): p. 5-32.

155. Mathai, N., Y. Chen, and J. Kirchmair, *Validation strategies for target prediction methods.* Brief Bioinform, 2019.

156. Castaldi, P.J., I.J. Dahabreh, and J.P. Ioannidis, *An empirical assessment of validation practices for molecular classifiers.* Brief Bioinform, 2011. **12**(3): p. 189-202.

157. EUCAST, *The European Committee on Antimicrobial Susceptibility Testing. Breakpoint Tables for Interpretation of MICs and Zone Diameters. Version 6.0, 2016. http://www.eucast.org*

158. Wiegand, I., K. Hilpert, and R.E. Hancock, *Agar and broth dilution methods to determine the minimal inhibitory concentration (MIC) of antimicrobial substances.* Nat Protoc, 2008. **3**(2): p. 163-75.

159. EUCAST, *Tables of clinical breakpoints for antifungal agents, Version 9.0. , 2018.

160. Arnold, R.J. and J.P. Reilly, *Observation of Escherichia coli ribosomal proteins and their posttranslational modifications by mass spectrometry.* Anal Biochem, 1999. **269**(1): p. 105-12.

161. Gasteiger, E., et al., *Protein Identification and Analysis Tools on the ExPASy Server*, in *The Proteomics Protocols Handbook*, J.M. Walker, Editor. 2005, Humana Press: Totowa, NJ. p. 571-607.

162. Consortium, T.U., *UniProt: a worldwide hub of protein knowledge.* Nucleic Acids Research, 2018. **47**(D1): p. D506-D515.

163. ISBS, *Institute for Systems Biology, Proteomics Toolkit - MS/MS Fragment Ion Calculator, available through http://db.systemsbiology.net:8080/proteomicsToolkit/FragIonServlet.html. Last accessed March 2020.*

164. Hoaglin, D.C., B. Iglewicz, and J.W. Tukey, *Performance of Some Resistant Rules for Outlier Labeling.* J Am Stat Assoc, 1986. **81**(396): p. 991-999.

165. Tukey, J.W., *Exploratory Data Analysis.* Addison-Wesley, 1977.

166.   Maxson, T., C.L. Taylor-Howell, and T.D. Minogue, *Semi-quantitative MALDI-TOF for antimicrobial susceptibility testing in Staphylococcus aureus.* PLoS One, 2017. **12**(8): p. e0183899.

167.   Wallden, M., et al., *The Synchronization of Replication and Division Cycles in Individual E. coli Cells.* Cell, 2016. **166**(3): p. 729-739.

168.   Lomnitzer, R. and E.Z. Ron, *Synchronization of cell division in Escherichia coli by elevated temperatures: a reinterpretation.* J Bacteriol, 1972. **109**(3): p. 1316-8.

169.   Cutler, R.G. and J.E. Evans, *Synchronization of bacteria by a stationary-phase method.* J Bacteriol, 1966. **91**(2): p. 469-76.

170.   Lin, S.M., et al., *Characterising phase variations in MALDI-TOF data and correcting them by peak alignment.* Cancer Inform, 2005. **1**(1): p. 32-40.

171.   Ilina, E.N., et al., *Direct bacterial profiling by matrix-assisted laser desorption-ionization time-of-flight mass spectrometry for identification of pathogenic Neisseria.* J Mol Diagn, 2009. **11**(1): p. 75-86.

172.   Ryzhov, V. and C. Fenselau, *Characterization of the protein subset desorbed by MALDI from whole bacterial cells.* Anal Chem, 2001. **73**(4): p. 746-50.

173.   Statnikov, A., L. Wang, and C.F. Aliferis, *A comprehensive comparison of random forests and support vector machines for microarray-based cancer classification.* BMC Bioinformatics, 2008. **9**(1): p. 319.

174.   Shen, C., et al., *Comparison of computational algorithms for the classification of liver cancer using SELDI mass spectrometry: a case study.* Cancer Inform, 2007. **3**: p. 329-39.

175.   Dupret, G. and M. Koda, *Bootstrap re-sampling for unbalanced data in supervised learning.* Eur J Oper Res, 2001. **134**(1): p. 141-156.

176.   Janitza, S. and R. Hornung, *On the overestimation of random forest's out-of-bag error.* PLoS One, 2018. **13**(8): p. e0201904.

177.   Parker, B.J., S. Gunter, and J. Bedo, *Stratification bias in low signal microarray studies.* BMC Bioinformatics, 2007. **8**(1): p. 326.

178.   Aha, D.W. and R.L. Bankert, *A Comparative Evaluation of Sequential Feature Selection Algorithms*, in *Learning from Data: Artificial Intelligence and Statistics V*, D. Fisher and H.-J. Lenz, Editors. 1996, Springer New York: New York, NY. p. 199-206.

179.   Li, J., et al., *Feature Selection.* ACM Comput Surv, 2017. **50**(6): p. 1-45.

180.   Lewis, D.D. *Naive (Bayes) at forty: The independence assumption in information retrieval*. in *Nédellec C., Rouveirol C. (eds) Machine Learning: ECML-98. ECML 1998. Lecture Notes in Computer Science (Lecture Notes in Artificial Intelligence), vol 1398*. Springer, Berlin, Heidelberg.

181.   Mohd Sobran, N.M., A. Ahmad, and Z. Ibrahim, *Classification of imbalanced dataset using conventional naïve bayes classifier.* Int. Conf. on Artificial Intelligence in Computer Science and ICT (AICS, 2013: p. 25-26.

182.   Yaguchi, M., *Primary structure of protein S18 from the small Escherichia coli ribosomal subunit.* FEBS Lett, 1975. **59**(2): p. 217-20.

183.   Hobbs, E.C., J.L. Astarita, and G. Storz, *Small RNAs and small proteins involved in resistance to cell envelope stress and acid shock in Escherichia coli: analysis of a bar-coded mutant collection.* J Bacteriol, 2010. **192**(1): p. 59-67.

184.   Izutsu, K., et al., *Escherichia coli ribosome-associated protein SRA, whose copy number increases during stationary phase.* J Bacteriol, 2001. **183**(9): p. 2765-73.

185.   Friedman, D.I., *Integration Host Factor - a Protein for All Reasons.* Cell, 1988. **55**(4): p. 545-554.

186.   Agafonov, D.E., V.A. Kolb, and A.S. Spirin, *Ribosome-associated protein that inhibits translation at the aminoacyl-tRNA binding stage.* EMBO Rep, 2001. **2**(5): p. 399-402.

187.   Wadler, C.S. and C.K. Vanderpool, *A dual function for a bacterial small RNA: SgrS performs base pairing-dependent regulation and encodes a functional polypeptide.* Proc Natl Acad Sci U S A, 2007. **104**(51): p. 20454-9.

188.   Kern, R., et al., *Escherichia coli HdeB is an acid stress chaperone.* J Bacteriol, 2007. **189**(2): p. 603-10.

189.   Hughes, J.P., et al., *Principles of early drug discovery.* Br J Pharmacol, 2011. **162**(6): p. 1239-49.

190.   Stanton, T.B. and S.B. Humphrey, *Isolation of tetracycline-resistant Megasphaera elsdenii strains with novel mosaic gene combinations of tet(O) and tet(W) from swine.* Appl Environ Microbiol, 2003. **69**(7): p. 3874-82.

191.   Sanchez, M.S. and J.L. Watts, *Enhancement of the activity of novobiocin against Escherichia coli by lactoferrin.* J Dairy Sci, 1999. **82**(3): p. 494-9.

192.   Zhou, Y., et al., *Structure-guided discovery of novel aminoglycoside mimetics as antibacterial translation inhibitors.* Antimicrob Agents Chemother, 2005. **49**(12): p. 4942-9.

193.   Xu, P., et al., *Novel pleuromutilin derivatives with excellent antibacterial activity against Staphylococcus aureus.* Chem Biol Drug Des, 2009. **73**(6): p. 655-60.

194.   Poulsen, S.M., et al., *The pleuromutilin drugs tiamulin and valnemulin bind to the RNA at the peptidyl transferase centre on the ribosome.* Mol Microbiol, 2001. **41**(5): p. 1091-9.

195.   McOsker, C.C. and P.M. Fitzpatrick, *Nitrofurantoin: mechanism of action and implications for resistance development in common uropathogens.* J Antimicrob Chemother, 1994. **33 Suppl A**: p. 23-30.

196.   Menichetti, F., *Current and emerging serious Gram-positive infections.* Clin Microbiol Infect, 2005. **11 Suppl 3**: p. 22-8.

197.   Prágai, Z. and C.R. Harwood, *Regulatory interactions between the Pho and σB-dependent general stress regulons of Bacillus subtilis.* Microbiology, 2002. **148**(5): p. 1593-1602.

198.   Rouviere-Yaniv, J. and F. Gros, *Characterization of a novel, low-molecular-weight DNA-binding protein from Escherichia coli.* Proc Natl Acad Sci U S A, 1975. **72**(9): p. 3428-32.

199.   Natori, Y., et al., *A fail-safe system for the ribosome under zinc-limiting conditions in Bacillus subtilis.* Mol Microbiol, 2007. **63**(1): p. 294-307.

200.   Hensley, M.P., et al., *Characterization of Zn(II)-responsive ribosomal proteins YkgM and L31 in E. coli.* J Inorg Biochem, 2012. **111**: p. 164-72.

201. Stojkova, P., P. Spidlova, and J. Stulik, *Nucleoid-Associated Protein HU: A Lilliputian in Gene Regulation of Bacterial Virulence.* Frontiers in Cellular and Infection Microbiology, 2019. **9**(159).

202. Bolt, E.L., et al., *Identification of Escherichia coli ygaQ and rpmG as novel mitomycin C resistance factors implicated in DNA repair.* Biosci Rep, 2015. **36**(1): p. e00290.

203. Reynolds, P.E., *Structure, biochemistry and mechanism of action of glycopeptide antibiotics.* Eur J Clin Microbiol Infect Dis, 1989. **8**(11): p. 943-50.

204. Bisacchi, G.S. and J.I. Manchester, *A New-Class Antibacterial-Almost. Lessons in Drug Discovery and Development: A Critical Analysis of More than 50 Years of Effort toward ATPase Inhibitors of DNA Gyrase and Topoisomerase IV.* ACS Infect Dis, 2015. **1**(1): p. 4-41.

205. Szychowski, J., et al., *Inhibition of aminoglycoside-deactivating enzymes APH(3')-IIIa and AAC(6')-Ii by amphiphilic paromomycin O2''-ether analogues.* ChemMedChem, 2011. **6**(11): p. 1961-6.

206. Mashruwala, A.A., et al., *The DUF59 Containing Protein SufT Is Involved in the Maturation of Iron-Sulfur (FeS) Proteins during Conditions of High FeS Cofactor Demand in Staphylococcus aureus.* PLoS Genet, 2016. **12**(8): p. e1006233.

207. Bonissone, S., et al., *N-terminal protein processing: a comparative proteogenomic analysis.* Mol Cell Proteomics, 2013. **12**(1): p. 14-28.

208. Wehrli, W., *Rifampin: mechanisms of action and resistance.* Rev Infect Dis, 1983. **5 Suppl 3**: p. S407-11.

209. Heide, L., *New aminocoumarin antibiotics as gyrase inhibitors.* Int J Med Microbiol, 2014. **304**(1): p. 31-6.

210. Maxwell, A. and D.M. Lawson, *The ATP-binding site of type II topoisomerases as a target for antibacterial drugs.* Curr Top Med Chem, 2003. **3**(3): p. 283-303.

211. Hooper, D.C., *Mode of action of fluoroquinolones.* Drugs, 1999. **58 Suppl 2**: p. 6-10.

212. Jachak, G.R., et al., *Silicon Incorporated Morpholine Antifungals: Design, Synthesis, and Biological Evaluation.* ACS Med Chem Lett, 2015. **6**(11): p. 1111-6.

213. Chryssanthou, E. and M. Cuenca-Estrella, *Comparison of the Antifungal Susceptibility Testing Subcommittee of the European Committee on Antibiotic Susceptibility Testing proposed standard and the E-test with the NCCLS broth microdilution method for voriconazole and caspofungin susceptibility testing of yeast species.* J Clin Microbiol, 2002. **40**(10): p. 3841-4.

214. Barchiesi, F., et al., *In vitro activity of five antifungal agents against clinical isolates of Saccharomyces cerevisiae.* Med Mycol, 1998. **36**(6): p. 437-40.

215. Borman, A.M., et al., *MIC distributions for amphotericin B, fluconazole, itraconazole, voriconazole, flucytosine and anidulafungin and 35 uncommon pathogenic yeast species from the UK determined using the CLSI broth microdilution method.* J Antimicrob Chemother, 2020 (ahead of print).

216. Kathwate, G.H. and S.M. Karuppayil, *Tramadol, an Opioid Receptor Agonist: An Inhibitor of Growth, Morphogenesis, and Biofilm Formation in the Human Pathogen, Candida albicans.* Assay Drug Dev Technol, 2016. **14**(10): p. 567-572.

217. Yousfi, H., et al., *Repurposing of Ribavirin as an Adjunct Therapy against Invasive Candida Strains in an In Vitro Study.* Antimicrob Agents Chemother, 2019. **63**(10): p. e00263-19.

218. Bolard, J., V. Joly, and P. Yeni, *Mechanism of Action of Amphotericin B at the Cellular Level. Its Modulation by Delivery Systems.* J Liposome Res, 2008. **3**(3): p. 409-427.

219. Polak, A., *Preclinical data and mode of action of amorolfine.* Dermatology, 1992. **184 Suppl 1**: p. 3-7.

220. Pasko, M.T., S.C. Piscitelli, and A.D. Van Slooten, *Fluconazole: a new triazole antifungal agent.* DICP, 1990. **24**(9): p. 860-7.

221. CLSI, *Performance Standards for Antifungal Susceptibility Testing of Yeasts, 1st ed. CLSI Supplement M60. Wayne, PA: Clinical and Laboratory Standards Institute; 2017.* 2017.

222. Pfaller, M.A., et al., *Wild-type MIC distributions and epidemiological cutoff values for amphotericin B, flucytosine, and itraconazole and Candida spp. as determined by CLSI broth microdilution.* J Clin Microbiol, 2012. **50**(6): p. 2040-6.

223. Lockhart, S.R., et al., *Validation of 24-hour flucytosine MIC determination by comparison with 48-hour determination by the Clinical and Laboratory Standards Institute M27-A3 broth microdilution reference method.* J Clin Microbiol, 2011. **49**(12): p. 4322-5.

224. Hawser, S. and K. Islam, *Comparisons of the effects of fungicidal and fungistatic antifungal agents on the morphogenetic transformation of Candida albicans.* J Antimicrob Chemother, 1999. **43**(3): p. 411-3.

225. Arthington-Skaggs, B.A., et al., *Comparison of visual and spectrophotometric methods of broth microdilution MIC end point determination and evaluation of a sterol quantitation method for in vitro susceptibility testing of fluconazole and itraconazole against trailing and nontrailing Candida isolates.* Antimicrob Agents Chemother, 2002. **46**(8): p. 2477-81.

226. Dignard, D., et al., *Identification and characterization of MFA1, the gene encoding Candida albicans a-factor pheromone.* Eukaryot Cell, 2007. **6**(3): p. 487-94.

227. Mercer, E.I., *Morpholine antifungals and their mode of action.* Biochem Soc Trans, 1991. **19**(3): p. 788-93.

228. Holz, R.W., *Polyene Antibiotics: Nystatin, Amphotericin B, and Filipin*, in *Mechanism of Action of Antieukaryotic and Antiviral Compounds*, F.E. Hahn, Editor. 1979, Springer-Verlag Berlin Heidelberg. p. 313-340.

229. Ouedraogo, R., et al., *Global analysis of circulating immune cells by matrix-assisted laser desorption ionization time-of-flight mass spectrometry.* PLoS One, 2010. **5**(10): p. e13691.

230. Munteanu, B., et al., *Sensitive, robust and automated protein analysis of cell differentiation and of primary human blood cells by intact cell MALDI mass spectrometry biotyping.* Anal Bioanal Chem, 2012. **404**(8): p. 2277-86.

231. Kugeratski, F.G., et al., *Hypoxic cancer-associated fibroblasts increase NCBP2-AS2/HIAR to promote endothelial sprouting through enhanced VEGF signaling.* Sci Signal, 2019. **12**(567): p. eaan8247.

232. Ligon, A.H., et al., *Identification of a novel gene product, RIG, that is down-regulated in human glioblastoma.* Oncogene, 1997. **14**(9): p. 1075-81.

233. Jacob, S.T., K. Ghoshal, and J.F. Sheridan, *Induction of metallothionein by stress and its molecular mechanisms.* Gene Expr, 1999. **7**(4-6): p. 301-10.

234. Margoshes, M. and B.L. Vallee, *A Cadmium Protein from Equine Kidney Cortex.* J Am Chem Soc, 1957. **79**(17): p. 4813-4814.

235. Karin, M. and H.R. Herschman, *Dexamethasone stimulation of metallothionein synthesis in HeLa cell cultures.* Science, 1979. **204**(4389): p. 176-7.

236. Thirumoorthy, N., et al., *A review of metallothionein isoforms and their role in pathophysiology.* World J Surg Oncol, 2011. **9**: p. 54.

237. Tsangaris, G.T. and F. Tzortzatou-Stathopoulou, *Metallothionein expression prevents apoptosis: a study with antisense phosphorothioate oligodeoxynucleotides in a human T cell line.* Anticancer Res, 1998. **18**(4A): p. 2423-33.

238. Peng, B., et al., *Microarray-assisted pathway analysis identifies MT1X & NFkappaB as mediators of TCRP1-associated resistance to cisplatin in oral squamous cell carcinoma.* PLoS One, 2012. **7**(12): p. e51413.

239. Sovcikova, A., et al., *Effect of cyclosporin A in Lewis rats in vivo and HeLa cells in vitro.* J Appl Toxicol, 2002. **22**(3): p. 153-60.

240. An, K.C., *Selective Estrogen Receptor Modulators.* Asian Spine J, 2016. **10**(4): p. 787-91.

241. Krashin, E., et al., *Thyroid Hormones and Cancer: A Comprehensive Review of Preclinical and Clinical Studies.* Front Endocrinol (Lausanne), 2019. **10**: p. 59.

242. Maneckjee, R., *Anticancer effects of therapeutic opioids.* Pain Forum, 1999. **8**(4): p. 213-215.

243. Goldstein, M.R., L. Mascitelli, and F. Pezzetta, *Do statins prevent or promote cancer?* Curr Oncol, 2008. **15**(2): p. 76-7.

244. Mrusek, M., et al., *Identification of cellular and molecular factors determining the response of cancer cells to six ergot alkaloids.* Invest New Drugs, 2015. **33**(1): p. 32-44.

245. Obrero, M., D.V. Yu, and D.J. Shapiro, *Estrogen receptor-dependent and estrogen receptor-independent pathways for tamoxifen and 4-hydroxytamoxifen-induced programmed cell death.* J Biol Chem, 2002. **277**(47): p. 45695-703.

246. Chen, W., H.H. Chung, and J.T. Cheng, *Opiate-induced constipation related to activation of small intestine opioid mu2-receptors.* World J Gastroenterol, 2012. **18**(12): p. 1391-6.

247. McCorvy, J.D. and B.L. Roth, *Structure and function of serotonin G protein-coupled receptors.* Pharmacol Ther, 2015. **150**: p. 129-42.

248. Samandi, S., et al., *Deep transcriptome annotation enables the discovery and functional characterization of cryptic small proteins.* Elife, 2017. **6**: p. e27860.

249. Yamaguchi, H. and H.G. Wang, *CHOP is involved in endoplasmic reticulum stress-induced apoptosis by enhancing DR5 expression in human carcinoma cells.* J Biol Chem, 2004. **279**(44): p. 45495-502.

250. Nakamura, N., *Ubiquitin System.* Int J Mol Sci, 2018. **19**(4): p. 1080.

251. Lee, J.C. and M.E. Peter, *Regulation of apoptosis by ubiquitination.* Immunol Rev, 2003. **193**: p. 39-47.

252. de Baey, A., et al., *Complex expression pattern of the TNF region gene LST1 through differential regulation, initiation, and alternative splicing.* Genomics, 1997. **45**(3): p. 591-600.

253. Rollinger-Holzinger, I., et al., *LST1: a gene with extensive alternative splicing and immunomodulatory function.* J Immunol, 2000. **164**(6): p. 3169-76.

254. Raboy, B., et al., *Effect of stress on protein degradation: role of the ubiquitin system.* Acta Biol Hung, 1991. **42**(1-3): p. 3-20.